PHYSICS-BASED CHARACTERIZATION OF LAMBDA SENSOR OUTPUT TO CONTROL EMISSIONS FROM NATURAL GAS FUELED ENGINES

by

MOHAMED AHMED TOEMA

B.S., Benha High Institute of Technology, 1995
M.S., Benha High Institute of Technology, 2004

AN ABSTRACT OF A DISSERTATION

submitted in partial fulfillment of the requirements for the degree

DOCTOR OF PHILOSOPHY

Department of Mechanical and Nuclear Engineering
College of Engineering

KANSAS STATE UNIVERSITY
Manhattan, Kansas

2010

Abstract

The increasingly strict air emission regulations may require implementing Non-Selective Catalytic Reduction (NSCR) systems as a promising emission control technology for stationary rich burn spark ignition engines. Many recent experimental investigations that used NSCR systems for stationary natural gas fueled engines showed that NSCR systems were unable to consistently control the exhaust emissions level below the compliance limits. Part of this thesis is devoted to show the results from the field testing of three engines working in natural gas gathering stations located in the "Four Corners" area. These three engines are retrofitted with NSCR systems. Emissions and engine operating data were monitored for more than one year. Data collected from October 2007 through December 2008 shows significant variation in emissions levels over hours, days, and longer periods of time, as well as seasonal variations. As a result of these variations, simultaneous control of NO_x and CO below the compliance limit was achieved less than fifty percent of the monitored time.

Modeling of NSCR components to better understand, and then exploit, the underlying physical processes that occur in the lambda sensor and the catalyst media is now considered an essential step toward improving NSCR system performance. The second portion of this thesis focuses on modeling the lambda sensor that provides feedback to the air-to-fuel ratio controller. Correct interpretation of the sensor output signal is necessary to achieve consistently low emissions level. The goal of this modeling study is to improve the understanding of the physical processes that occur within the sensor, investigate the cross-sensitivity of various exhaust gas species on the sensor performance, and finally this model serves as a tool to improve NSCR control strategies. This model simulates the output from a planar switch type lambda sensor. The model consists of three modules. The first module models the multi-component mass transport through the sensor protective layer. Diffusion fluxes are calculated using the Maxwell-Stefan equation. The second module includes all the surface catalytic reactions that take place on the sensor platinum electrodes. All kinetic reactions are modeled based on the Langmuir-Hinshelwood kinetic mechanism. The third module is responsible for simulating the reactions that occur on the electrolyte material and determine the sensor output voltage. The details of these three modules as well as a parametric study that investigates the sensitivity of the output voltage signal to various exhaust gas parameters is provided in the thesis.

PHYSICS-BASED CHARACTERIZATION OF LAMBDA SENSOR OUTPUT TO CONTROL EMISSIONS FROM NATURAL GAS FUELED ENGINES

by

MOHAMED AHMED TOEMA

B.S., Benha High Institute of Technology, 1995
M.S., Benha High Institute of Technology, 2004

A DISSERTATION

submitted in partial fulfillment of the requirements for the degree

DOCTOR OF PHILOSOPHY

Department of Mechanical and Nuclear Engineering
College of Engineering

KANSAS STATE UNIVERSITY
Manhattan, Kansas

2010

Approved by:

Major Professor
Kirby S. Chapman

Copyright

Abstract

The increasingly strict air emission regulations may require implementing Non-Selective Catalytic Reduction (NSCR) systems as a promising emission control technology for stationary rich burn spark ignition engines. Many recent experimental investigations that used NSCR systems for stationary natural gas fueled engines showed that NSCR systems were unable to consistently control the exhaust emissions level below the compliance limits. Part of this thesis is devoted to show the results from the field testing of three engines working in natural gas gathering stations located in the "Four Corners" area. These three engines are retrofitted with NSCR systems. Emissions and engine operating data were monitored for more than one year. Data collected from October 2007 through December 2008 shows significant variation in emissions levels over hours, days, and longer periods of time, as well as seasonal variations. As a result of these variations, simultaneous control of NO_x and CO below the compliance limit was achieved less than fifty percent of the monitored time.

Modeling of NSCR components to better understand, and then exploit, the underlying physical processes that occur in the lambda sensor and the catalyst media is now considered an essential step toward improving NSCR system performance. The second portion of this thesis focuses on modeling the lambda sensor that provides feedback to the air-to-fuel ratio controller. Correct interpretation of the sensor output signal is necessary to achieve consistently low emissions level. The goal of this modeling study is to improve the understanding of the physical processes that occur within the sensor, investigate the cross-sensitivity of various exhaust gas species on the sensor performance, and finally this model serves as a tool to improve NSCR control strategies. This model simulates the output from a planar switch type lambda sensor. The model consists of three modules. The first module models the multi-component mass transport through the sensor protective layer. Diffusion fluxes are calculated using the Maxwell-Stefan equation. The second module includes all the surface catalytic reactions that take place on the sensor platinum electrodes. All kinetic reactions are modeled based on the Langmuir-Hinshelwood kinetic mechanism. The third module is responsible for simulating the reactions that occur on the electrolyte material and determine the sensor output voltage. The details of these three modules as well as a parametric study that investigates the sensitivity of the output voltage signal to various exhaust gas parameters is provided in the thesis.

Table of Contents

List of Figures

List of Tables

Nomenclature

Acronyms

4SCRB	Four-Stroke Cycle, Rich Burn
AFRC	Air-to-Fuel Ratio Controller
ASME	American Society of Mechanical Engineers
BACT	Best Available Control Technology
CAA	Clean Air Act
CFR	Code of Federal Regulation
DOE	United States Department of Energy
EGO	Exhaust Gas Oxygen
EIA	United States Energy Information Administration
EPA	United States Environmental Protection Agency
FTIR	Fourier-Transform Infrared Spectroscopy
GHG	Green House Gas
HAP	Hazardous Air Pollutant
HEGO	Heated Exhaust Gas Oxygen
IEA	International Energy Agency
INGAA	Interstate Natural Gas Association of America
MACT	Maximum Achievable Control Technology
M-S	Maxwell-Stefan equation
NAAQS	National Ambient Air Quality Standards
NESHAP	National Emissions Standards of Hazardous Air Pollutants
NGML	National Gas Machinery Laboratory
NMHC	Non-Methane Hydrocarbons
NSCR	Non-Selective Catalytic Reduction
NSPS	New Source Performance Standards
PM	Particulate Matter
PRCI	Pipeline Research Council International, Inc.
PSD	Prevention of Significant Deterioration

RACT	Reasonably Available Control Technology
REPP	Renewable Energy Policy Project
RICE	Reciprocating Internal Combustion Engines
SAE	Society of Automotive Engineers
SCR	Selective Catalytic Reduction
SIP	State Implementation Plan
THC	Total Hydrocarbons
TWC	Three-Way Catalyst
UEGO	Wide-Band or Universal Exhaust Gas Oxygen Sensor
VOC	Volatile Organic Compound
YSZ	Yatteia-Stabilized Zirconia

Greek variables

$\Sigma_{v,i}$	Diffusion volume of species i [m^3/mol]
v_o	Oxide positive vacancy [-]
∇	Gradient operator [-]
ν	Stoichiometric coefficient [-]
λ	Normalized air-to-fuel ratio (AF_{act}/AF_{st}) [-]
$\mathcal{K}$	Ratio of reaction coefficients [-]
ε/q	Porosity/ Tortuosity [-]
θ	Electrode occupancy [-]

Species

CH_4	Methane
CO	Carbon monoxide
CO_2	Carbon dioxide
H_2	Hydrogen
H_2O	Water vapor
HCHO	Formaldehyde
HCN	Hydrogen cyanide
N_2	Nitrogen

N_2O	Nitrous oxide
NH_3	Ammonia
NO	Nitric oxide
NO_2	Nitrogen dioxide
NO_x	Oxides of nitrogen ($NO+NO_2$)
O_2	Oxygen
Pd	Palladium
Pt	Platinum
Rh	Rhodium
SO_x	Sulfur oxides
Y_2O_3	Yttrium dioxide
ZrO_2	Zirconium dioxide

Variables and Parameters

AF	Air-to-fuel ratio [-]
B	Matrix composed of x and D [s/m^2]
C	Molar concentration [mol/m^3]
D_{ij}	Binary diffusion coefficient of i into j [m^2/s]
e	Electron [-]
E	Activation energy [kJ/mol]
F	Faraday's constant [C/mol]
J	Diffusive flux [$mol/m^2.s$]
k	Pre-exponential factor [s^{-1}]
L	Adsorption capacity [mol/m^2]
M	Molecular weight [kg/kmol]
m	Number of electrons (Nernst eq.) [-]
n	Total number of exhaust gas species [-]
P	Exhaust gas pressure [Pa]
R_u	Universal gas constant [J/kmol-K]
s	Sticking probability [-]
T	Exhaust gas temperature [K]

V	Sensor output voltage [mV]
x	Mole fraction [-]
z	Dimensional coordinate [m]
$\mathbb{C}_v$	Vacancy concentration in electrolyte [-]

Subscripts

a	Adsorption
act	Actual
d	Desorption
elec	Electrode
exh	Exhaust
i	Species *i*
o	Electrolyte oxide
ref	Reference electrode
s	Active site
st	Stoichiometric
v	Vacant Site

Acknowledgements

I would like to acknowledge the people, without whom, this research would not have been possible. First, I would like to express my gratitude to my advisor Dr. Kirby S. Chapman, Professor and Director of the National Gas Machinery Laboratory (NGML), for his benevolent guidance, and endless support and trust over the years of my PhD work. I learned from his impressive professional and personal skills that cannot be gained from books. I will always be proud that I graduated from NGML under his supervision.

A special thanks to the members of my doctoral committee panel:

- Dr. Donald Fenton: I enjoyed his Thermal System Design class so much. This is a unique class that includes design and optimization of thermal systems. I am hoping to teach this class when I return to my faculty position back home.
- Dr. Larry Glasgow: I am most grateful for him teaching me the Transport Phenomena classes. Dr. Glasgow is the model academic teacher who is talented in both engineering knowledge and strong communication skills with his students.
- Dr. Keith Hohn: His Advanced Chemical Reaction class changed my perception about chemical reactions and chemical kinetics, as many of mechanical engineering major. Now, I have a lot of fun modeling catalytic reactions. This work would not have been done without his thoughtful discussion and insightful comments.

I wish to thank Sandy Chapman for her compassionate assistance and continuous counseling. I think one of the secrets of the NGML success is the lovely and friendly environment she inspires. Also I would like to thank all of the NGML staff and my co-workers for their help and cooperation.

I would like to express my sincere thanks to Pipeline Research Council International, Inc. (PRCI) for financial support of this project and for their confidence in the NGML.

Lastly, I do not know the words that can express my gratitude to my mother for her emotional motivation and patience through the last four years while I have been so far from home. Thanks to my wife for her love and understanding during this work.

Dedication

To the exceptional father and mentor

AHMED TOEMA

November 16, 1944 – August 8, 2007

The one who encouraged me to pursue the PhD degree, even though he knew that the remaining part of his life was short and he had the feeling that he might never see me again after I came to US in January 2007.

Preface

Information included in this dissertation has been previously published in the form of technical reports submitted to the U.S. Department of Energy and BP of America Company:

- Toema, M., Nuss-Warren, S., and Chapman, K.S., "Cost-Effective Reciprocating Engine Emissions Control and Monitoring for E&P Field and Gathering Engines," U.S. Department of Energy, DOE Award DE-FC26-02NT15464, Technical Progress Quarterly Reports 25-32, Work Completed January 2009 – October 2010.
- Nuss-Warren, S., Toema, M., and Chapman, K.S., "Four Corners NSCR Characterization Study," Final Report Volume 1and 2, BP of America, May, 2009.

In addition to the previous technical reports, there are several peer reviewed papers which have been published from this work:

- Toema, M., and Chapman, K.S., 2010, "Physics-Based Characterization of NSCR Operation - Part 1," Gas Machinery Conference, October 4-6, Phoenix, AZ.
- Toema, M., and Chapman, K.S., 2010, "Interpreting the Lambda Sensor Output to Control Emissions from Natural Gas Fueled Engines," Proceedings of the 2010 Fall of ASME Internal Combustion Engine Division Technical Conference, ICEF2010-35164, Sept.12-15, San Antonio, TX.
- Toema, M., Nuss-Warren, S., Chapman, K.S., 2009, "Long-Term Emissions Performance of Stationary Natural Gas Engines Equipped with NSCR System," Gas Machinery Conference, October 5-7, Atlanta, GA.
- Toema, M., Nuss-Warren, S., Chapman, K.S., McCarthy, J., and McGrath, T., 2009, "Mapping Study to Characterize NSCR Performance on a Natural Gas-Fueled Engine," Proceedings of the 2009 Spring of ASME Internal Combustion Engine Division Technical Conference, ICES2009-76120, May 3-6, Milwaukee, WI.

Chapter 1 - Introduction

Since the invention of the internal combustion engine in 1876 by N. A. Otto, there has been a continuous increase in the demand of internal combustion engine production. Even in the twenty first century, the reciprocating internal combustion engine is still one of the major mechanical engineering wonders. The use of the internal combustion engine is not only limited to the road vehicle application but also it extends to stationary engine applications. Stationary engines are considered one of the sources of mechanical power generation. Stationary engines are used extensively as a prime mover of mechanical equipment, such as compressors and pumps, or they can be coupled directly with an electrical generator to produce electrical power.

The pollutants emitted from any combustion process have a deleterious effect on the environment. In 2008, the annual review of US Energy Information Administration (EIA) revealed that 3.33 million metric tons of nitrogen oxides were produced from fossil fuel combustion (EIA, 2010). The growth in the internal combustion engine usage contributes to the environment air pollution. The increased public concern about the adverse effect of the engine pollutants has led to stringent air emissions regulations. The last decade has witnessed a significant development and amendment of the emissions legislations to control emissions from the internal combustion engines.

This chapter briefly introduces the air emissions regulations. This thesis focuses on the impact of these regulations on the stationary engines industry. In addition, a discussion about the role of stationary engines in the US natural gas industry will be presented. Also this chapter gives a glimpse about the ways that can be followed to control engines emissions. Finally, this chapter gives a scope of the current study and outlines the objectives of this work.

Regulatory Motivation

Historically, the first piece of legislation that regulates air emissions is the Clean Air Act (CAA) promulgated in 1970. This was the first substantive and comprehensive environmental statute enacted by US Congress. The Act underwent a major revision in 1977 as a result of congressional impatience with the pace of air quality improvement. For a variety of reasons, the 1977 amendments also proved ineffective against several air pollution problems that became especially prominent and controversial early in the 1980s. Public concerns over acid rain,

regional smog, and air toxics increased as efforts to amend the law continued from 1982 to 1990. The CAA took its current form on November 15, 1990 (Renewable Energy Policy Project (REPP), 2000). The central pillars of the 1990 amendments are:

- Title I: seeks to prevent smog and attain national air quality standards;
- Title II: imposes tighter tailpipe and fuel standards for vehicles;
- Title III: focuses on protecting human health from air toxics;
- Title IV: seeks to control acid rain;
- Title V: creates a new comprehensive permitting system; and
- Title VI: protects and monitors the stratospheric ozone layer.

The CAA authorizes the Environmental Protection Agency (EPA) to develop these air regulations and timely review the existing rules. The primary standards that trigger emission control for stationary engines used in the natural gas industry are:

- National Ambient Air Quality Standards (NAAQS)
- New Source Performance Standards (NSPS)
- National Emission Standards for Hazardous Air Pollutants (NESHAPs)

The National Ambient Air Quality Standards (NAAQS) have been the cornerstone of the CAA. The NAAQS limit the allowable concentration for six "criteria pollutants," which are ozone, particulate matter, nitrogen dioxide, carbon monoxide, sulfur dioxide and lead. Ozone is considered the main pollutant in NAAQS. It forms as a result of nitrogen oxides (NO_x) reaction with other gases in the presence of sun light. Any geographical area with ozone levels in excess of the NAAQS ozone limit is termed "non-attainment" area. The EPA requires states to develop a State Implementation Plan (SIP), where the state identifies regulations it will adopt to improve air quality and "attain" NAAQS. Figure 1.1 shows an example of a non-attainment ozone map based on an 8-hour average of 2006-2008 data. This figure shows the counties that violate 60-70 part per billion (ppb) ozone limits.

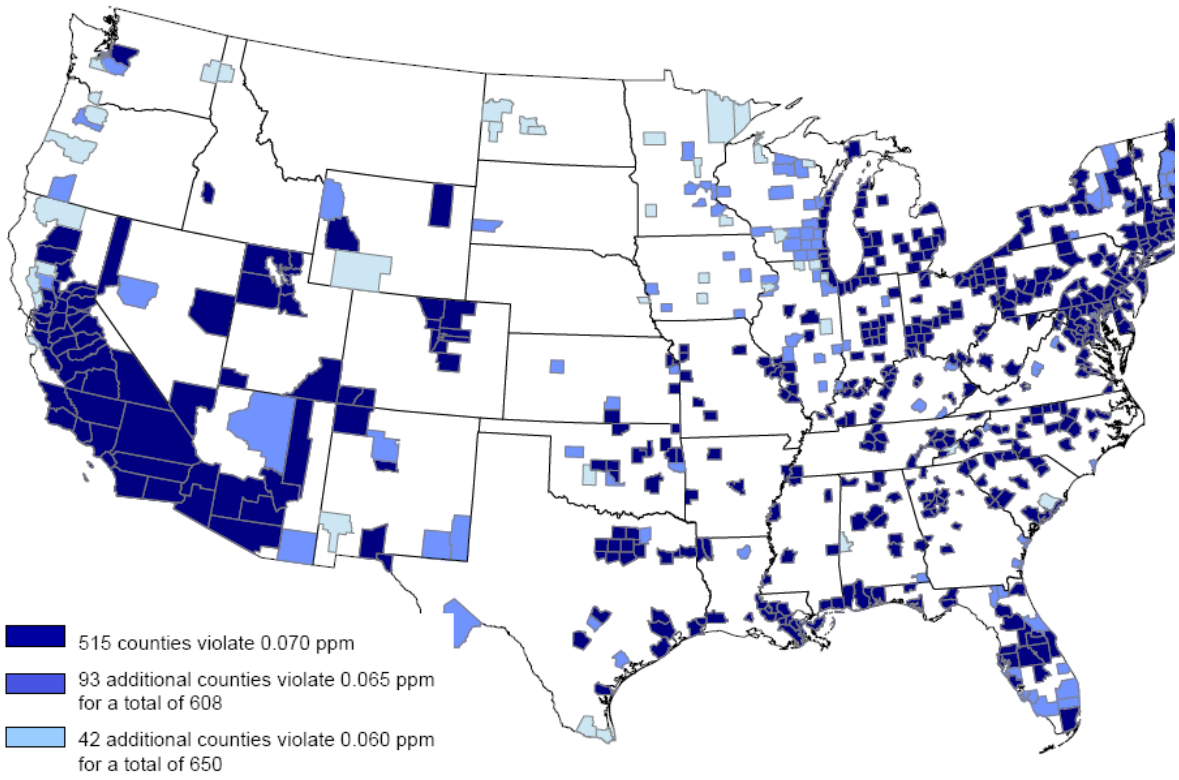

Figure 1.1 Ozone non-attainment areas based on 2006-2008 data (EPA, 2010)

The National Emission Standards for Hazardous Air Pollutants (NESHAPs) regulate the air toxic emissions. The CAA identifies 188 hazardous air pollutants (HAPs) that are to be controlled from sources. The NESHAP of stationary reciprocating internal combustion engines identifies four specific HAPs in a major source: formaldehyde, acrolein, methanol, and acetaldehyde.

In 2004, EPA established Title 40 of the Code of Federal regulation (CFR) Part 63 which regulates the HAPs from reciprocating internal combustion engine. The 2004 Maximum Achievable Control Technology (MACT) standard is a federal control regulation that is consistently applied nationwide. This rule requires formaldehyde control for engines larger than 500 hp that are located at a major source. A major source of HAPs is defined as having the facility-wide potential to emit 10 tons per year or more for a single HAP or 25 tons per year for aggregation of all HAPs. This rule has been revised twice since 2004. The first revision was in 2008 and the second one was in 2009.

The main amendment of NESHAP in 2008 is that smaller engines which are below 500 hp were also included under this rule. Additionally, it affects all engine types such as new, modified or reconstructed engines (40 CFR- Part 63, Subpart ZZZZ).

The third standard that triggers emission controls is the New Source Performance Standards (NSPS). The EPA promulgated the final rule of NSPS in January 2008 along with the NESHAP amendments. Like NESHAP, this final rule affects all RICE sizes and types. Based upon this rule, there is no engine size threshold. According to this rule, the engine compliance limit of NO_x, CO, and Volatile Organic Compounds (VOCs) are specified based upon engine size and category. This rule requires the use of Non-Selective Catalytic Reduction (NSCR) systems for rich burn spark ignition engines and combustion-based control technology for lean burn engines (40 CFR- Part 60, Subpart JJJJ).

Recently, EPA announced NAAQS in 2010 for nitrogen dioxide. Nitrogen dioxide is one of the species of nitrogen oxides NO_x which significantly contribute to the formation of particulate matter and smog. In another scope, EPA is developing a rule to limit the applicability of greenhouse gas (GHG) emission regulations under the CAA Prevention of Significant Deterioration (PSD) and Title V operating permit programs. Carbon dioxide (CO_2) and methane (CH_4) are the primary greenhouse gases related to the natural gas industry. Methane emissions are especially important due to its global warming potential. Methane has 21 times the effect of CO_2 on a relative mass basis. Several new initiatives have been lunched to develop a rule for reporting and tracking GHG emissions. In September, 2009, EPA issued a final rule requiring the reporting from large industrial sources with emissions greater than 25,000 metric tons per year of CO_2 equivalent. These sources are required to report their GHG emissions beginning in 2011. Additionally, EPA is proposing another set of regulations that will address oil and natural gas industry fugitive methane emissions (INGAA, 2010).

US Natural Gas Transmission Industry

Natural gas is an important major source of energy. The annual review of US Energy Information Administration (EIA) showed that natural gas consumption during 2009 is 22.8 trillion cubic feet (Tcf), which represents 24.7 percent of the total energy consumption (EIA, 2010). Recent projections by the International Energy Agency (IEA) indicate that the worldwide demand of natural gas will increase by 44 percent between 2008 and 2035 with an average increase 1.4 percent per year (IEA, 2010). Because of this demand for natural gas fuel, natural gas transmission and distribution has a pervasive grid of pipeline network and infrastructure. In US and Canada, there are roughly 38,000 miles of gathering pipeline, 85 billion cubic feet (Bcf) per day of natural gas processing capacity, 350,000 miles of transmission pipeline, 4.5 trillion cubic feet (Tcf) of natural gas storage capacity (INGAA, 2009). Transporting natural gas from wellhead to market involves a series of processes and an array of physical facilities. Among these are:

- **Gathering Lines:** These small-diameter pipelines move natural gas from the wellhead to the natural gas processing plant or to an interconnection with a larger mainline pipeline.
- **Processing Plant**: This operation extracts natural gas liquids and impurities from the natural gas stream.
- **Mainline Transmission Systems**: These wide-diameter, long-distance pipelines transport natural gas from the producing area to market areas.
- **Market Hubs/Centers:** Locations where pipelines intersect and flows are transferred.
- **Underground Storage Facilities:** Natural gas is stored in depleted oil and gas reservoirs, aquifers, and salt caverns for future use.
- **Peak Shaving**: System design methodology permitting a natural gas pipeline to meet short-term surges in customer demands with minimal infrastructure. Peaks can be handled by using gas from storage or by short-term line-packing.

Between the producing area and the market area, a number of compressor stations are located along the transmission system. These compressor stations are “pumping” facilities that advance the flow of natural gas. They are usually situated between 50 and 100 miles apart along

the length of a natural gas pipeline system, and are designed to operate on a nonstop basis. The average station is capable of moving about 700 million cubic feet (MMcf) of natural gas per day, while the largest can move as much as 4.6 billion cubic feet (Bcf) per day.

In 2007, the US interstate natural gas pipeline network relied on more than 1,200 natural gas compressor stations to maintain the continuous flow of natural gas between supply area and consumers as shown in Figure 1.2.

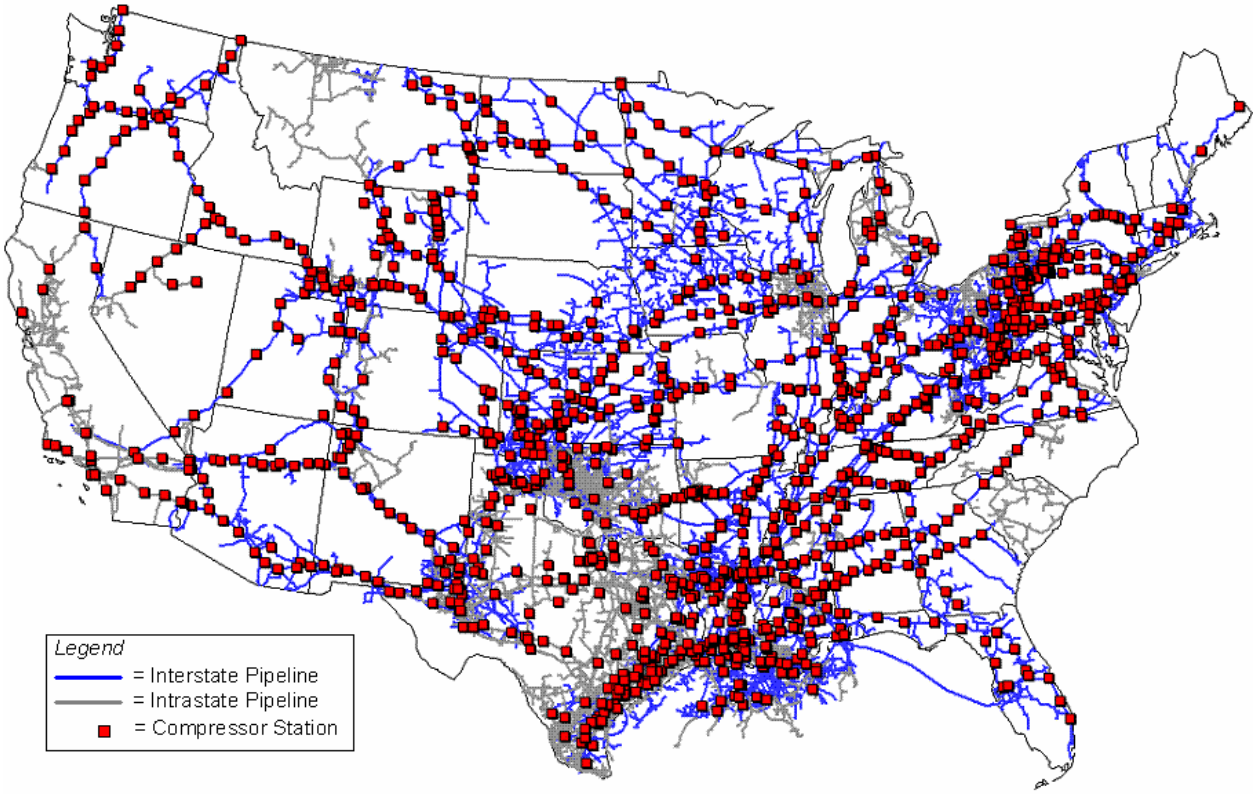

Figure 1.2 Interstate natural gas transmission grid compressor stations (EIA, 2007)

Stationary internal combustion engines play a significant role in the natural gas transmission industry. Most of the compressor stations and gathering stations rely extensively on internal combustion engines to drive their compressors. Integral reciprocating compressor engines larger than 1,000 hp comprise half of the 16 million hp of installed US gas compression capacity. The total number of engines that serve this industry around 5,600 engines (PRCI, 2005). Unfortunately, the majority of natural gas-fired reciprocating engine-compressor units are employing a technology that originated in the middle of the last century, promoting the use of the

term “legacy” when referring to this technology (Grauer, 2010). The natural gas transmission industry now faces great challenges to retrofit these legacy engines to comply with new emission regulations.

In response to the new strict EPA regulations, the Pipeline Research Council International, Inc. (PRCI) developed a detailed technology roadmap to overcome these challenges. The PRCI is a consortium of the world’s leading pipeline companies, vendors, service providers, original equipment manufacturers, and other organizations that support the natural gas transmission industry. The main objective of the PRCI is to provide this industry with the development and deployment of research solutions to the operation, maintenance, and regulatory challenges that face the industry.

The PRCI roadmap is a comprehensive multi-year research plan to find solutions that make natural gas legacy engines comply with EPA regulations (e.g. achieve 0.5 g/hp-hr NO_x) , while meeting a cost-objective of one thirds the replacement cost. Compliance scenarios that require either widespread engine replacement or engine retrofit to achieve unprecedented emissions levels have severe financial consequences. The engine replacement cost scenario ranges from $2.2 billion to $6 billion (PRCI, 2005), while retrofits could be appreciably less if ultra-low NO_x technology are developed.

The PRCI roadmap database groups the engines used in the natural gas transmission industry into five categories:

1. 2SC lean burn loop scavenged Clark and Cooper engines (~70%)
2. 4SC lean-burn (9%)
3. 4SC rich-burn (9%)
4. 2SC lean-burn uniflow scavenged (7%)
5. 4SC lean-burn port injected (5%)

Through this roadmap, PRCI defines the technology dimensions that can be used to achieve the cost-effectively compliance goal. The current technology gaps were also mentioned and the appropriate options to overcome these technical gaps. The main areas of dimensions that need technical focus to achieve the PRCI objectives are:

- Ignition
- Air Delivery
- Mixing (Combustion Performance)

- Air Management
- After-Treatment Technology
- Closed Loop Controls

In-cylinder combustion control technology is expected to be used for lean burn engines, while the NSCR is the promising technology for rich burn engines.

The work reported in this thesis is part of the NSCR research program, which is developed according to the PRCI roadmap. The Department of Energy (DOE), PRCI, BP, Emit, and others funded the work presented in this thesis to improve the performance of NSCR systems and make this technology a viable solution to comply with the recent stringent EPA regulations.

The Need for NSCR Modeling

Over the last several decades, the automotive and other industries have conducted a substantial amount of research into the use of NSCR systems to reduce NO_x and CO emissions. For the most part, these research activities focused entirely on gasoline-fueled engines. Much of that research has been published in the public domain through the Society of Automotive Engineers (SAE) and the American Society of Mechanical Engineers (ASME) conferences and journals. The studies of NSCR on gasoline-fueled engines are not necessarily transportable to natural gas-fueled engines without a detailed understanding of how the system responds to natural gas combustion products. The difficulty in finding a reliable model that describes the performance of NSCR components in natural gas service serves as the primary motivation for this project.

More recently, the natural gas pipeline industry and the Department of Energy have supported a significant amount of research to characterize NSCR catalyst systems for four-stroke cycle rich burn (4SRB) natural gas engines. While a substantial quantity of data has been collected, a clear understanding of how NSCR catalysts function remains somewhat elusive. The data collected from these studies revealed that the currently available NSCR system technology was not capable of consistently reducing exhaust emissions for long-term operation. Emission concentrations were not consistent from day-to day, or even from hour-to hour. One of the key outcomes from these studies was that the inconsistency of the lambda (i.e., normalized air-to-fuel ratio) sensor output affects the NSCR system performance.

There is a direct, but as yet not well understood, connection between the physical processes that occur within the lambda sensor and the performance of the NSCR catalyst. The lambda sensor voltage, which is a function of numerous parameters such as the exhaust gas specie concentrations, is created by the difference between the equilibrium oxygen concentration at the EGO sensor surface and the oxygen concentration in the atmosphere. This voltage is then used to control the air-to-fuel ratio that enters the engine.

Also clear from the plethora of experimental data is that the processes that occur within the lambda sensor are not well-understood and/or predictable. Instead of continuing the hunt-and-peck approach that has been employed to date, this research develops a lambda sensor model to actually understand the underlying physical processes that occur in the sensor. Once these physical processes are understood, a parametric investigation will be completed to then understand how specie concentrations and the existence of specific exhaust species impact the sensor performance. This information can then be used to develop a simplified model that can be incorporated into NSCR air-to-fuel ratio controllers.

In summary, the motivation for the study reported in this thesis is the need for a more precise control strategy of NSCR/AFRC systems to comply with New Source Performance Standards promulgated by the EPA in January 2008, as well as the insufficient relevant investigations in the open literature that address the specific application of NSCR systems to control emissions from natural gas-fueled engines. Furthermore, most, if not all, modeling work conducted for NSCR catalysts has focused on the reduction and oxidation of exhaust products from gasoline-fueled engines, not natural gas-fueled engines. The exhaust gas species are sufficiently different to upset the delicate balance required for acceptable, if not optimal, NSCR system operation. Because of all of these issues regarding NSCR system performance, there is a need to develop high fidelity models for NSCR system components. This is because experimental work alone (i.e., laboratory work or field test work) is too time consuming, and is a very expensive approach to overcome all of the NSCR challenges. Accurate models can be used to run parametric studies faster and optimize the overall system performance better than running experimental tests.

Objectives

The overarching goal of this research is to improve the performance of NSCR systems to maintain consistent engine compliance with the recent stringent emission regulations. This overarching goal is achieved by developing a mathematical model of NSCR systems to better understand the operating characteristics and interactions between the system components.

Due to the significant role of the lambda sensor on the overall NSCR system, this study focuses on the development of a high-fidelity, physics-based lambda sensor model. This mathematical model is based upon first engineering principles and chemical kinetics laws. Once the model development is completed, a comprehensive parametric investigation is conducted to determine the effect of various parameters on the lambda sensor performance.

The parametric study is used to identify and understand the parameters that affect the lambda sensor voltage output. The model will be used as a reliable tool to achieve the following primary objectives:

- Provide a deeper insight into the transport and electrochemical processes that occur within the lambda sensor;
- Define the influence of exhaust gas composition from natural gas-fueled engines; and
- Serve as a powerful approach to develop a better control strategy for NSCR systems.

Thesis Overview

The thesis is divided into six chapters. Chapter 2 presents the literature review of industry and academic work that has been published to complete the study objectives. This chapter also provides a background about NSCR systems and its components. Additionally, it presents the different mechanisms of pollutant emissions formation.

Chapter 3 presents the results obtained from the implementation of the NSCR system on three natural gas-fueled engines used in natural gas gathering stations. This chapter describes the methodology that has been applied to retrofit these engines with the NSCR system. The data obtained from the long term study as well as engine mapping is presented in this chapter.

Chapter 4 describes the detailed mathematical governing equations that are used to model the lambda sensor. The sensor mathematical model is composed of different modules, which represent each part of the sensor. This chapter lists the equations that describe each module. The reaction scheme of the electrode elementary step reactions is also presented in this chapter.

Chapter 5 shows the result obtained from the sensor model. The model validation and verification is presented in this chapter. This chapter also shows the results obtained from the two approaches that are used to model the lambda sensor. The first approach is the model without considering the reaction of methane into the sensor platinum electrode. The second approach is the extension of the first approach by integrating methane surface reactions on the platinum electrode. The result from the sensitivity analysis and parametric study are also included in this chapter.

Chapter 6 outlines the conclusions from this work and the recommendation for further research work.

Chapter 2 - Literature Review

This chapter presents a thorough literature review about NSCR systems and lambda sensor modeling studies. The goal of the NSCR system is to control the pollutant emissions exhausted from internal combustion engines. Therefore, this chapter starts with an introduction to the various mechanisms of pollutant formation that occur during the combustion process. The basics of NSCR systems are also introduced. This chapter presents the background about lambda sensors and reviews of the recent research and scholarly work conducted on lambda sensors. Finally, the governing equations that were used to model the lambda sensor are presented.

Emission Formation Mechanisms

The five principle classes of pollutant species emitted from any combustion process are nitrogen oxides (NO_x), carbon monoxide (CO), organic compounds (VOC, unburned and partially burned hydrocarbons), sulfur oxides (SO_x) and particulates (Bowman, 1975). For natural gas fired engines, the emissions of sulfur oxides and particulate matters (PM) are negligibly small. The typical exhaust emissions from internal combustion engines are shown in Figure 2.1. Each constituent has a different trend than the others and there is usually trade-off between the pollutant species. As a result of this difference in behavior of each exhaust pollutant, the control of all of these species is considered a challenge for any emission control technology.

Figure 2.1 shows the dependence of pollutant concentrations on the normalized air-to-fuel ratio (λ). Lambda is the ratio of the actual air-to-fuel to the stoichiometric air-to-fuel:

$$\lambda = \frac{AF_{act}}{AF_{st}} \tag{2-1}$$

When lambda equals one, the quantity of air is equal to the theoretical amount required for complete combustion of the fuel. For lean operation, lambda will be larger than unity and for rich operation lambda will be less than unity. Carbon monoxide exhibits a large surge in concentration at rich operation. This increase in CO is caused by the insufficient amount of oxygen to convert all the carbon in the fuel to carbon dioxide (Ferguson et al., 2000). Nitrogen oxide is mainly governed by the combustion temperature. However, the adiabatic flame

temperature reaches its peak at a slightly rich lambda (Law et al., 2005), while the highest NO_x concentration level occurs at a slightly lean lambda due to the existence of sufficient oxygen atoms necessary for atmospheric nitrogen oxidation. Hydrocarbons appear in the exhaust gases as a result of incomplete combustion of the hydrocarbon fuels. Hydrocarbon emissions decrease with increasing lambda until a point is reached where further increase in lambda can cause engine misfiring. Consequently, more hydrocarbons are produced.

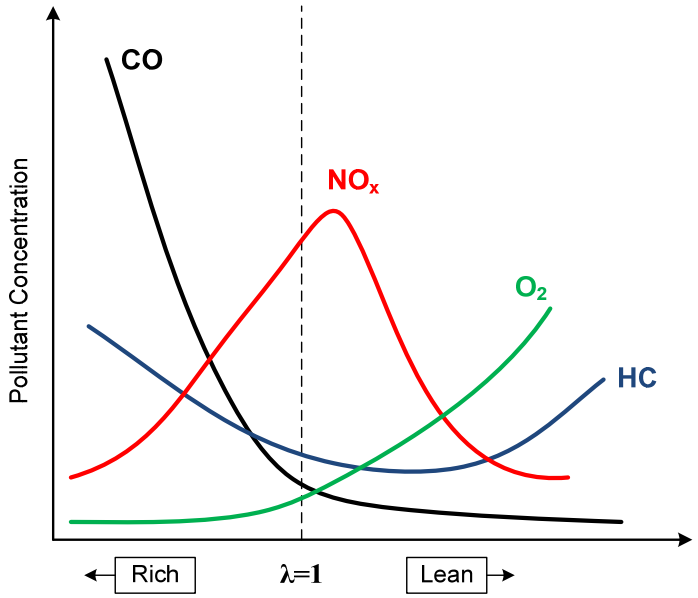

Figure 2.1 Exhaust emissions from typical uncontrolled engine

NO_x Formation

In the atmosphere, nitrogen oxides react in the presence of sun light with unburned hydrocarbons to form photochemical smog, which deleteriously affects the environment. Nitrogen oxides (NO_x) refer to the combination of nitric oxide (NO) and nitrogen dioxide (NO_2). The formation of NO_2 results only from the oxidation of NO, so the total NO_x (NO + NO_2) is not affected by the amount of NO_2 formed. Therefore, the calculation of NO is normally sufficient for determining NO_x.

The formation mechanism of NO_x has been a topic of intensive research for many decades (Kuo, 2005). The literature review revealed that there are several paths for NO_x formation. There are four well-recognized chemical mechanisms for NO formation. These

include the Zeldovich, prompt, nitrous oxide, and fuel-bound nitrogen pathways. The following sections describe of these four NO producing chemical mechanisms.

Thermal Mechanism (Zeldovich Mechanism)

This mechanism is the first major work conducted on the kinetics of NO_x formation. Zeldovich postulated this mechanism around the middle of the last century (1946). The Zeldovich mechanism consists of two chain reactions (Turns, 2000):

$$O + N_2 \rightleftarrows NO + N \qquad \textbf{(2-2)}$$

$$N + O_2 \rightleftarrows NO + O \qquad \textbf{(2-3)}$$

These reactions are further extended by adding the reaction:

$$N + OH \rightleftarrows NO + H \qquad \textbf{(2-4)}$$

The NO formed through the Zeldovich mechanism is referred to as thermal NO because the formation rates strongly depend on temperature. The Zeldovich mechanism is the most widely used and recognized mechanism for NO formation. The nitrogen incorporated in this mechanism is the atmospheric nitrogen, which is introduced to the combustion process with atmospheric air.

Reaction (2-2) is the rate-limiting step in the Zeldovich mechanism because of its low reaction rate constant (Kuo, 2005). Reaction (2-2) requires a very high activation energy to occur due to the strong triple bond in the N_2. Figure 2.2 shows the chain nature of the Zeldovich reaction mechanism. This reaction proceeds only at sufficiently high temperatures. As a rule of thumb, the thermal mechanism is usually important at temperatures above 1800 K.

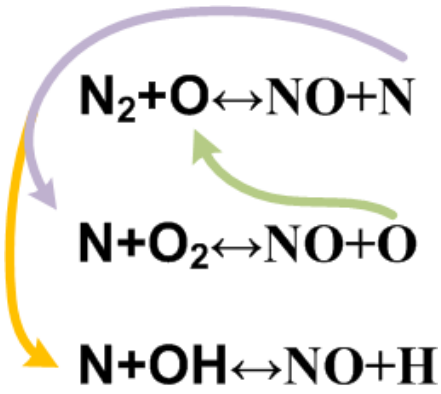

Figure 2.2 Chain nature of the Zeldovich NO_x mechanism

Reaction (2-3) is much faster than reaction (2-2), so the N atom can be assumed to be in steady state. In addition, the NO formation process is assumed to be much slower than the combustion process; this allows the assumption that the elements affecting the formation of NO are in their equilibrium concentrations (Heywood, 1988). With these assumptions, the rate of NO formation becomes:

$$\frac{d[\mathrm{NO}]}{dt} = \frac{2R_1\left\{1-\left([\mathrm{NO}]/[\mathrm{NO}]_e\right)^2\right\}}{1+\left([\mathrm{NO}]/[\mathrm{NO}]_e\right)R_1/(R_2+R_3)} \tag{2-5}$$

The R_i parameters are based on the forward kinetic reaction rate constants for the three reactions in the extended Zeldovich mechanism and the equilibrium concentrations of the applicable species:

$$R_1 = k_1^+[\mathrm{O}]_e[\mathrm{N}_2]_e \tag{2-6}$$

$$R_2 = k_2^+[\mathrm{N}]_e[\mathrm{O}_2]_e \tag{2-7}$$

$$R_3 = k_3^+[\mathrm{N}]_e[\mathrm{OH}]_e \tag{2-8}$$

The kinetic rate constants *k* are based on the temperature of the reacting mixture and are readily available for each reaction in the extended Zeldovich mechanism (Heywood, 1988). Equation (2-5) is a simple expression that can be used to calculate the NO formation rate when the temperature and equilibrium concentrations of the applicable species are known.

Prompt Mechanism (Fenimore Mechanism)

The prompt, or Fenimore, mechanism was first proposed by Fenimore in 1971 to account for NO formation that occurred very quickly in the primary reaction zone of the combustor (Fenimore, 1971). Researchers later found that NO is formed from hydrocarbon fragments present during the combustion process reacting with nitrogen (Nicol et al., 1995). The primary initiating reaction is:

$$N_2 + CH \rightleftharpoons HCN + N \qquad \textbf{(2-9)}$$

The N atom becomes NO through the last two reactions in the Zeldovich mechanism. The hydrogen cyanide (HCN) path to NO is complex, but its main path is through NCO, NH, N, and then finally to NO through the same Zeldovich N atom reactions. Prompt NO refers to NO formed in the flame zone, while thermal NO refers to NO formed in the post flame zone.

Nitrous Oxide Mechanism

The nitrous oxide (N_2O) mechanism was recognized by Malte and Pratt in 1974 as an important NO pathway (Corr et al., 1991). It is regarded as being most relevant in low-temperature conditions, such as those experienced in lean-premixed combustion (Turns, 2000). The three main steps of this mechanism are:

$$O + N_2 + M \rightleftharpoons N_2O + M \qquad \textbf{(2-10)}$$

$$H + N_2O \rightleftharpoons NO + NH \qquad \textbf{(2-11)}$$

$$O + N_2O \rightleftharpoons NO + NO \qquad \textbf{(2-12)}$$

Reaction (2-10) occurs when oxygen atom O reacts with N_2 in the presence of a third element M to form N_2O. The N_2O may subsequently react with H and O atoms according to reactions (2-11) and (2-12).

Fuel-Bound Nitrogen Mechanism

Combustion of fuel containing nitrogen shows an increase in NO production (Toof, 1985). This increase in NO is a result of the conversion of the nitrogen in the fuel to NO. The mechanism begins with the pyrolysis of the nitrogen-containing fuel to HCN. The HCN then follows the same pathway to NO as the prompt mechanism. Because of this, the fuel and prompt NO are considered linked processes (Toof, 1985). This mechanism is obviously unimportant in fuels containing no nitrogen, such as natural gas, but contributes significantly when burning nitrogen containing fuels such as coal.

CO Formation

Carbon monoxide is formed during an intermediate step in any hydrocarbon combustion reaction scheme as depicted in Figure 2.3. After this intermediate step, if the combustion temperature remains adequately high for a sufficient period of time, CO begins to oxidize by the hydroxyl free radical OH to form CO_2, according to the following reaction:

$$CO + OH \rightleftharpoons CO_2 + H \qquad \textbf{(2-13)}$$

Carbon monoxide formation is very dependent on the temperature profile, mixing rate, and residence time. The CO formation rate is inversely proportional to the residence of the pollutant in the CO burnout zone before quenching of the oxidation process occurs (Connors et al., 1996).

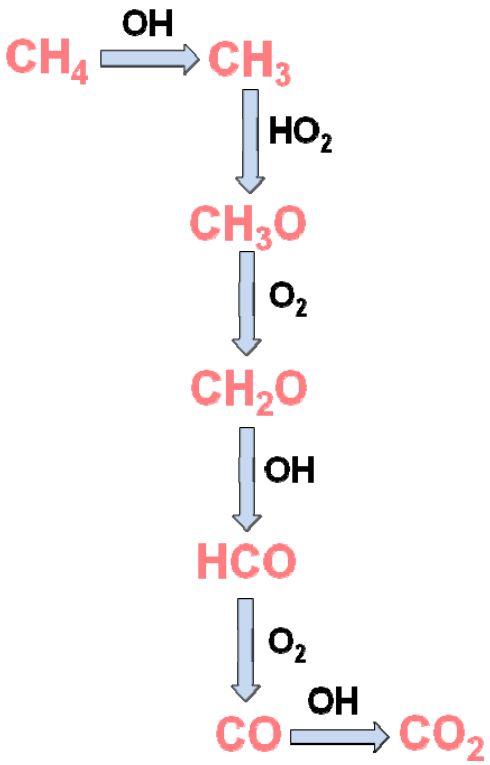

Figure 2.3 Main reaction scheme for methane (CH_4) oxidation

Large amounts of CO are formed during fuel-rich combustion because of the lack of sufficient oxygen to complete the reaction to CO_2. If the combustion mixture is stoichiometric or moderately fuel–lean, significant amounts of CO will also be present due to the dissociation of CO_2. Carbon monoxide emissions are found to be much higher than calculated from equilibrium calculations and to be highest at low–power conditions, where burning rates and peak temperatures are relatively low (Lefebvre, 1999).

Carbon monoxide emission formation and oxidation is primarily controlled by the trapped equivalence ratio and the oxidation of hydrocarbon fuels. Methane oxidation, the fuel of interest in this work, has been studied extensively. A kinetic model was developed from extensive experimentation which includes 207 reactions with 40 species. The major reaction scheme is shown in Figure 2.3 (Borman et al., 1998). This complex combustion mechanism still does not completely describe CH_4 combustion. The use of every mechanism to quantify the oxidation event could require the solution of approximately 1,000 coupled differential equations (Westbrook et al., 1984). There is ongoing work conducted by a research group in National Gas

Machinery Laboratory (NGML, Kansas State University) to develop a global reaction mechanism of CO formation in internal combustion engines (McFarland et al., 2010).

NSCR System

The utilization of the NSCR system schematically shown in Figure 2.4 is the method of choice for rich burn engines. There is a strong regulatory prejudice for NSCR systems to the point where the operators prefer four-stroke cycle rich burn engines over four-stroke cycle lean burn engines. Such a system relies on three components to control NO_x, CO, and unburned hydrocarbon (HC) emissions: a three-way catalyst (TWC), an air-to-fuel ratio controller (AFRC), and exhaust gas oxygen (EGO) or lambda (λ) sensors to determine the oxygen concentration in the exhaust. All three components must function correctly and be tuned properly to successfully reduce emissions to the target level and maintain reliable performance.

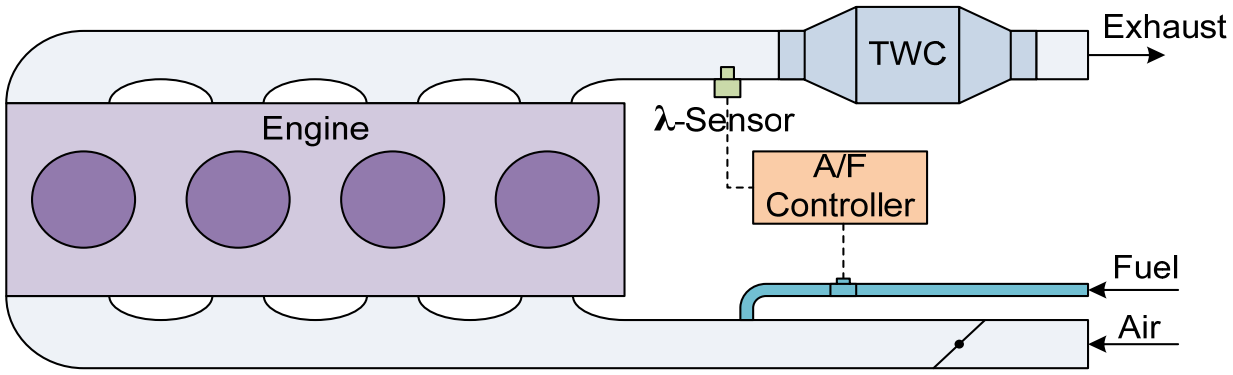

Figure 2.4 Schematic of NSCR system

The catalyst facilitates the reduction of NO_x to N_2 and the oxidation of CO and hydrocarbons into CO_2 and water vapor as in the following general reactions:

- Oxidation Reactions:

$$2CO + O_2 \longrightarrow 2CO_2 \quad \textbf{(2-14)}$$

$$2H_2 + O_2 \longrightarrow 2H_2O \quad \textbf{(2-15)}$$

$$C_xH_y + \left(x + \frac{y}{4}\right) O_2 \longrightarrow xCO_2 + \frac{y}{2}H_2O \quad \textbf{(2-16)}$$

- Reduction Reactions:

$$2CO + 2NO \longrightarrow 2CO_2 + N_2 \quad \textbf{(2-17)}$$

$$C_xH_y + \left(2x + \frac{y}{2}\right) NO \longrightarrow xCO_2 + \frac{y}{2}H_2O + \left(x + \frac{y}{4}\right) N_2 \quad \textbf{(2-18)}$$

$$2H_2 + 2NO \longrightarrow 2H_2O + N_2 \quad \textbf{(2-19)}$$

Nitrogen oxides can only undergo chemical reduction when there is very little oxygen in the engine exhaust, typically no more than 0.5% by volume (Lambert, 1995). As a result, researchers report that the catalyst can reduce both CO and NO_x by 80% or more only over a small range of lambda or air-to-fuel ratio.

The catalyst is the kernel of the NSCR system. The catalyst is a matrix of thousands of parallel channels that gives the monolith TWC the desired combination of large surface area and low pressure drop. The large area is needed for high reaction rates, and the pressure drop should be minimized to avoid adverse effects on the engine performance. The monolithic channels have washcoat material that contains the noble metals: platinum (Pt), palladium (Pd) and rhodium (Rh). Figure 2.5 shows a schematic of the monolithic catalytic converter. The main usage of these precious materials is to offer reaction pathways with lower activation energy. Consequently, the reactions can proceed at normal operating conditions and higher conversion efficiencies can be achieved.

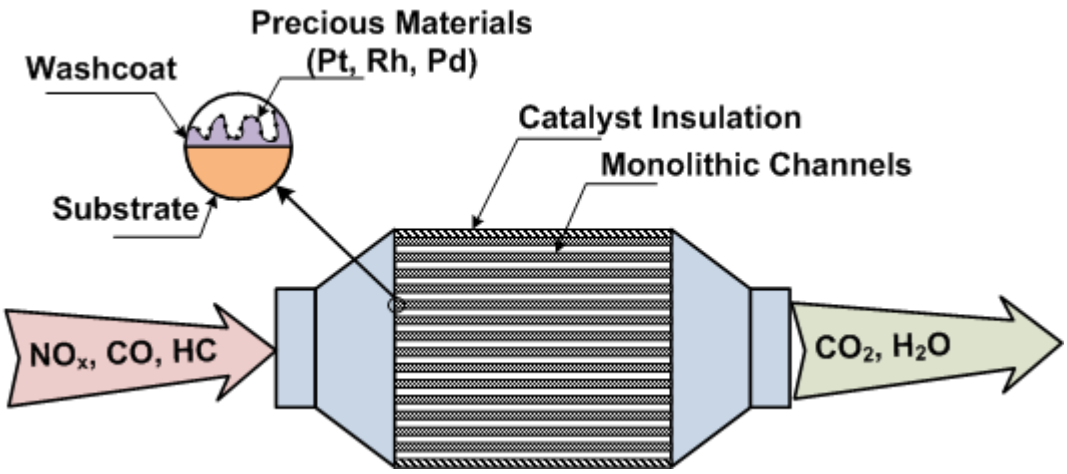

Figure 2.5 Schematic of monolithic catalytic converter (Pontikakis, 2003)

The second element of the NSCR system is the lambda sensor which, will be covered in detail in the following section. The final component of the NSCR system is the AFRC. It consists of electronics that modulate a fuel control valve. This valve must be properly sized to provide sufficient fuel so that the engine can run fully loaded at the proper air-to-fuel ratio. It also must reduce fuel flow sufficiently so that only the necessary fuel is provided during low-load operation. When the air-to-fuel ratio controller determines that the EGO signal indicates operation is too rich or too lean, it will modulate the fuel control valve to achieve the exhaust oxygen voltage set point.

The literature indicates that the catalysts operate most efficiently with engine operation slightly rich of stoichiometric and a lambda operating window of about 0.99 +/- 0.005, which corresponds to an engine exhaust O_2 of between 0.3% and 0.5%. Figure 2.6 presents the conversion efficiency for each of the three pollutant species as a function of lambda. During rich operation, the conversion efficiency of NO_x is high because there are sufficient reducing species available such as CO, H_2 and HC that can reduce NO_x to N_2. On the other hand, lean operation results in a higher conversion efficiency of CO. The high CO conversion is obtained due to the availability of oxygen at lean operation, which oxidizes CO to CO_2. Meanwhile, NO_x and HC experience a reduction in their conversion efficiencies. Natural gas HCs are mainly low carbon-number HCs , such as methane. These kinds of HCs exhibit a decrease in their conversion due to the existence of water vapor and NO_x which inhibit the adsorption of these HCs on the catalytic

surface (Hanaki et al., 1996). For gasoline engines, the HCs are heavier and react in the same way as CO, achieving high conversion efficiency during rich operation.

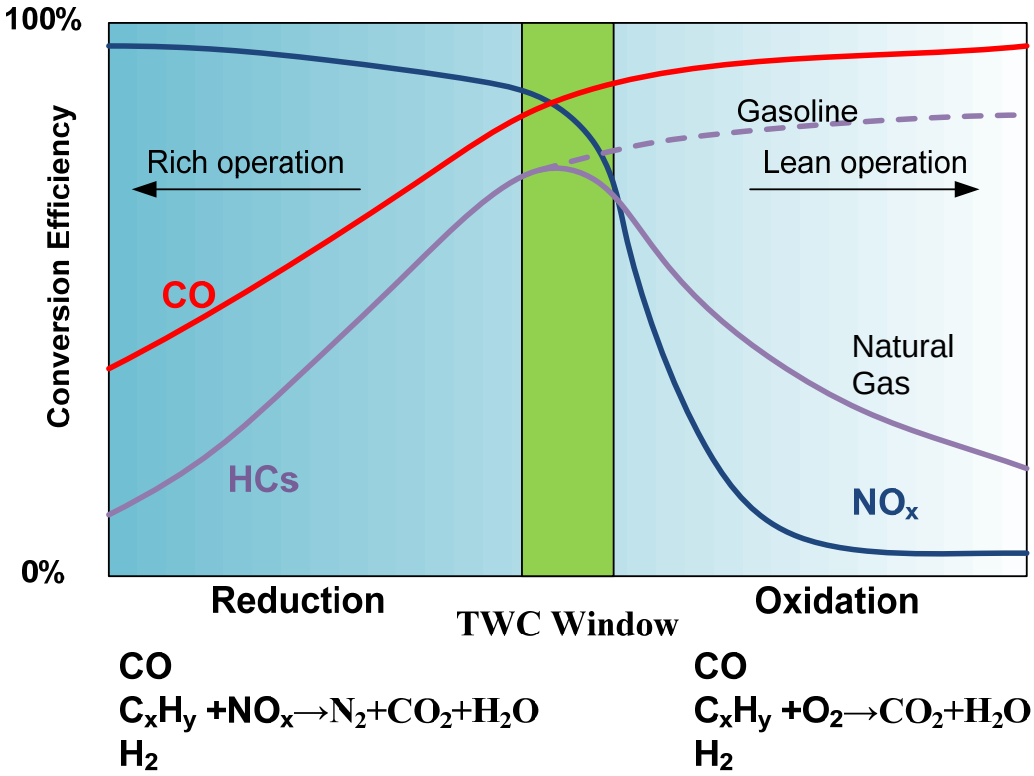

Figure 2.6 Influence of air-to-fuel ratio on pollutant conversion efficiency

The challenge of successfully deploying NSCR systems is basically the trade-off between NO_x and CO. The lambda sensor and the control system have a challenging task, which is providing the correct mixture to the TWC by controlling the air-to-fuel ratio within this very narrow catalytic operating window. The functional range for a catalyst can widen when the oxygen content varies periodically (i.e., dithers) around the ideal average value. Defoort et al. (2004) found that a 1% variation in equivalence ratio at 0.2 Hz (dithering) extended the 80% reduction window by approximately 20% by increasing NO_x reduction at leaner average equivalence ratios.

Previous studies of NSCR-equipped engines operating at California's Best Achievable Control Technology (BACT) limits of 0.15 g/bhp-hr NO_x and 0.6 g/bhp-hr CO showed the emissions may exceed compliance limits, with substantial excursions during load variations (Arney et al., 2007). Load and fuel quality variability in production applications could exacerbate these performance issues. These studies support concerns of NSCR systems effectiveness and reliability. However, the studies conducted by Arney et al. in California are based on engines and NSCR systems that are required to achieve more stringent limits than those typical for regulations such as NO_x RACT for existing engines or the new emissions constraints of 2.8 g/bhp-hr NO_x and 4.8 g/bhp-hr CO specified in the NSPS for engines between 25 and 100 hp.

Another study showed that ammonia could be produced by a 495 hp rich-burn engine with NSCR operating at rich conditions (Defoort et al., 2004) – i.e., richer operation decreases NO_x from NSCR-equipped engines but increases ammonia. Unlike in a laboratory setting, NSCR settings and operational reliability in the field may provide additional challenges, including "drift," that lead to undesirable levels of ammonia production. The question of what levels of ammonia are typically produced by field engines was not addressed in this laboratory study. As a result of the previous studies, implementation of NSCR systems on the legacy stationary natural gas pipeline engines is still challenging and needs more improvements.

Lambda Sensor

This section of the chapter introduces the basics and background of lambda sensors. Additionally, it reviews the literature and research conducted on the modeling of lambda sensors.

Basics of Lambda Sensor

The fundamental engineering principle that governs the lambda sensor voltage output is based on the Nernst principle. The Nernst principle, developed in the late 1800s, describes the thermochemical behavior of a galvanic element. Figure 2.7 illustrates the basic components of the Nernst cell. As shown in Figure 2.7, the first layer exposed to the exhaust gases is the protective porous layer. This layer is a porous ceramic layer used to protect the catalytic platinum electrode from gas contamination and exhaust gas erosion. The second element of the Nernst cell is comprised of the platinum electrodes separated by the electrolytic material. These

electrodes serve as a catalyst that responds to the chemical composition of the gases that permeate through the protective ceramic layer. Many surface chemical reactions take place at this electrode, as well as the adsorption and desorption processes.

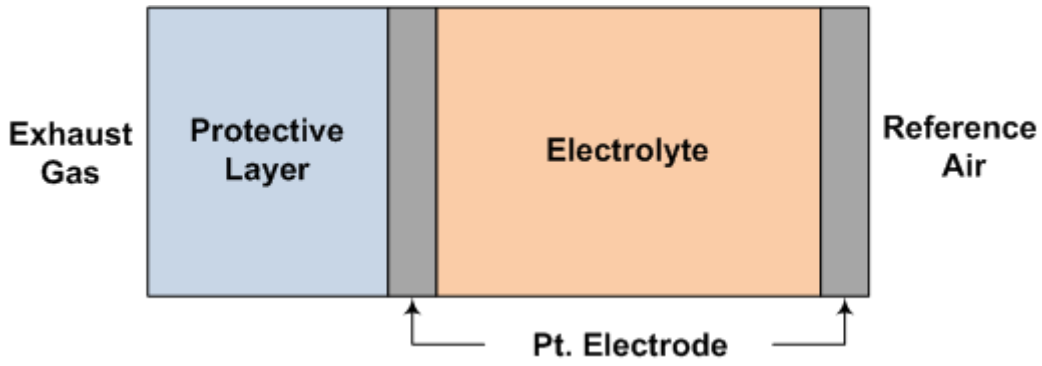

Figure 2.7 Basic components of the Nernst cell

These surface reactions largely affect the thermodynamic equilibrium oxygen concentration at the left electrode in Figure 2.7. Thermodynamic equilibrium oxygen concentration is the main driving force for the output voltage from the sensor. The left electrode acts as the anode where oxidation processes occur according to the reaction:

$$2O_2^- \rightarrow O_2 + 4e^- \qquad \textbf{(2-20)}$$

The released electrons migrate to the right electrode, i.e., the cathode, through the external circuitry. The cathode is subjected to the higher oxygen concentration of atmospheric air, which is approximately 21%. A reduction reaction takes place at the cathode of the form:

$$O_2 + 4e^- \rightarrow 2O_2^- \qquad \textbf{(2-21)}$$

The released oxygen ions transfer through the electrolyte material to the anode. This conducting path for oxygen ions balances the electrons flowing through the external cell circuitry. Zirconium dioxide ceramic (ZrO_2) stabilized with yttrium dioxide (Y_2O_3) is becoming a commonly-used material (YSZ; Yttria-Stabilized Zirconia) due to its excellent ion conductivity as well as its mechanical strength and thermal shock resistance.

The typical response of a lambda sensor is illustrated in Figure 2.8. The oxygen partial pressure in air acts as a constant reference at approximately 21%. Consequently, the sensor output voltage depends primarily on the oxygen concentration in the exhaust gas alone, although the true response is due to the difference between the partial pressure of O_2 on the opposite sides of the sensor electrodes. As illustrated in Figure 2.8, a value of lambda that equates to a small oxygen concentration, i.e., a rich mixture such that $\lambda<1$, produces a higher output voltage due to the higher difference in oxygen concentrations between the two electrodes of the Nernst cell. Conversely, a value of lambda that equates to a relatively high oxygen concentration, i.e., a lean mixture such that $\lambda>1$, creates a lower output voltage due to the smaller difference in oxygen concentration across the two electrodes. Worth noting is that the sensor responds to the equilibrium oxygen concentration instead of the free exhaust gas oxygen concentration (Jones et al., 2002). The equilibrium oxygen concentration is the net result of reactions that occur on the sensor anode, and this concentration is different from the free or un-reacted oxygen, particularly during rich operation. The free oxygen concentration varies continuously with lambda while the equilibrium oxygen concentration changes in an almost step-change fashion at stoichiometric conditions. This difference between the free oxygen and the equilibrium oxygen explains the behavior of the sensor output voltage depicted in Figure 2.8.

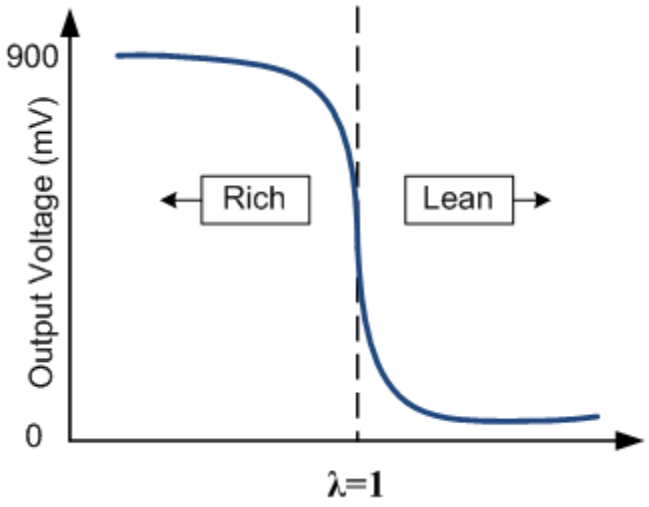

Figure 2.8 Typical output voltage from lambda sensor

Types of EGO Sensors

There are at least three EGO sensor classifications. The EGO sensor can be classified according to the material used, principle of operation, or configuration, and are referred to as (Ramamoorthy et al., 2003):

- Potentiometric;
- Amperometric; and
- Resistive Semiconductor

The resistive semiconductor is based mainly on the change in semiconductor material conductivity with oxygen concentration and reacting species of exhaust gases. This kind of EGO sensor has unacceptable limitations, such as resistance drift with time and weak long term robustness. The resistive semiconductor sensor is not durable and has lost the competitive edge to the other two sensor types (Riegel et al., 2002).

The potentiometric EGO sensor is based on the Nernst cell principle where the output voltage varies logarithmically with the oxygen concentration ratio across the sensor electrodes. Because of the rather abrupt logarithmic response, this sensor is sometimes referred to as the "switch-type" EGO sensor. Of note, again, is that the output voltage is based on the equilibrium oxygen concentration at the anode as opposed to the free oxygen concentration in the exhaust gases.

The amperometric sensor, commonly referred to as the wide band or broad band lambda sensor, is based on the limiting current principle where an additional cell is used for oxygen pumping. The pumping current, which is applied from an external circuit, is a function of the oxygen concentration. This technique facilitates the measurement of a wide lambda range between 0.7 to almost 4.

Evolution of the EGO Sensor

The development of the EGO sensor has passed through the following evolutionary stages:

- Increased the robustness and accuracy of the sensor in a harsh exhaust gas environment. This was the main concern in the first fifteen years;
- Introduced the ceramic heating element to eliminate cold start problems and minimize the sensor output dependence on the exhaust gas temperature (1980s);

- Improved the oxygen ion conductivity of the electrolyte and used partially stabilized zirconia to increase the mechanical strength/thermal shock resistance;
- Used a planar-type sensor instead of the original thimble-type. The planar sensor is a multi-layer sensor using thick film manufacturing technology (Bosch's Catalogs, 2009). The individual active layers are stacked together as shown in Figure 2.9, which enhances the integration of the heater strip within the sensor element. This design provides faster response time, robust construction, and a more effective heater design; and
- Improved the protective layer by using modern manufacturing methods to increase poisoning resistance and to avoid glaze formation in order to stabilize the dynamic control behavior over the sensor life.

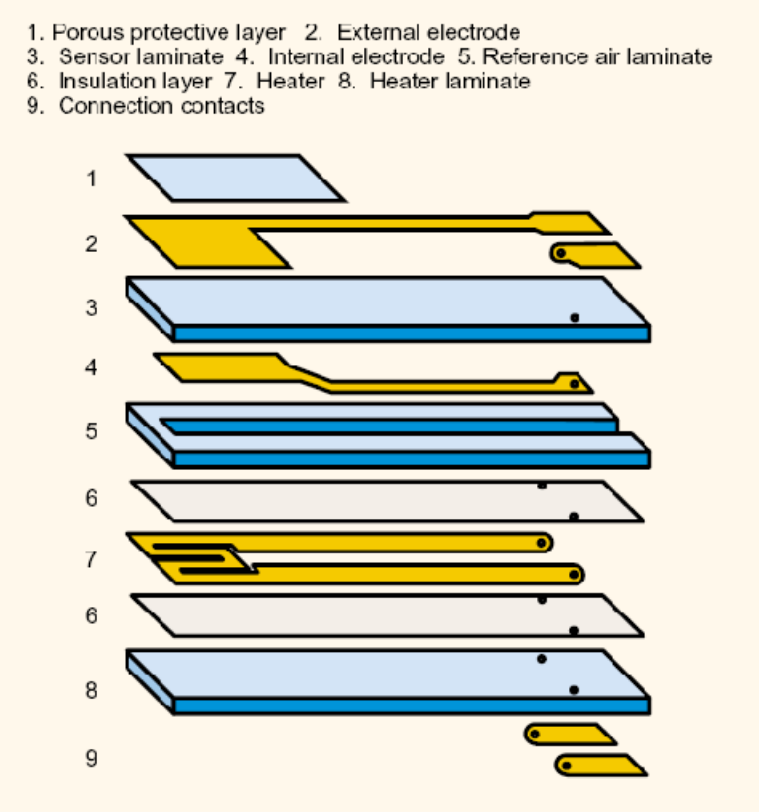

Figure 2.9 Planer-type sensor element layers (Bosch's catalogs)

Previous Work

Although the lambda sensor is based on the principle introduced by Walther Nernst in 1889, the overall integrated sensor modeling effort remains limited. Clearly, there is a need for a more general and accurate characterization of the sensor that can represent the specie transport,

catalytic reactions, and electrochemical processes that occur in the sensor. Since the late 1970s, there have been several preliminary investigations focused on finding suitable lambda sensor mathematical models. These studies start with defining the physical constants that govern sensor performance, and then determine values for these constants through experimental means (Fleming, 1977). The most important effort in modeling the lambda sensor was performed by Brailsford and his research group. This series of publications (Brailsford et al., 1993, 1995, 1996, 1997, and1998) introduced the first physics principle-based model of the lambda sensor, incorporated the influence of exhaust gas species and multiple reactions on the sensor voltage output, and included the impact of mass transfer transient behavior on the oxygen sensor performance.

During the same timeframe, there were serious attempts by Baker et al. (1994 and 1996) to obtain a general sensor model. They extended their studies to model the wide range lambda sensor. Much of the prior work focused on a specific part (element) of the lambda sensor, e.g., studies that focused exclusively on the electrolyte and ion exchange (Robertson et al., 1990; Potamianou et al., 1994; and Zhuiykov et al., 2006) and other studies that focused only on the electrode surface reactions and kinetics of these reactions (Mizusaki et al., 1987; Mizusaki et al.,1992; Granger et al., 1998; Harmsen et al., 2001; and Tsagarakis et al., 2005).

Auckenthaler et al. (2002) provided a detailed control-oriented model of a lambda sensor. This model is based on the thimble configured, switch-type sensor. The model output was verified with experimental measurements from a gasoline engine. The model showed good agreement with the measured data. They found that the reducing reactions of carbon monoxide and hydrogen had a significant impact on the sensor voltage output. They concluded that the actual air-to-fuel ratio controls the sensor output rather than the actual free oxygen concentration. This conclusion is consistent with the statement that the equilibrium oxygen concentration is responsible for the sensor output, as opposed to the free oxygen concentration.

From the survey of the previous work, it was found that the inconsistency of the lambda sensor output comes from many sources. The first one is due to the difference in mass transfer diffusion rate of various exhaust gas species other than oxygen through the sensor protective layer. The second source is due to the impact of the catalytic reactions of the reducing species on the sensor electrodes. The existence of some reducing species such as H_2, CO, and HC affect the thermodynamic equilibrium concentration of oxygen in the sensor.

The previous literature review illustrates the gap in lambda sensor modeling efforts, especially for natural gas-fueled engines. Most of the prior work focused on the gasoline engine and ignored the effect of unburned hydrocarbons from natural gas combustion on the lambda sensor output. While there are a number of experimental investigations that study the use of lambda sensors in natural gas fueled engines, such as Mizutani et al. (1998), no adequate parallel modeling efforts exist. The studies of sensor-controlled NSCR emission reduction systems on gasoline-fueled engines are not necessarily transportable to natural gas-fueled engines without a detailed understanding of how the lambda sensor responds to natural gas combustion products. The difficulty in finding a reliable model that describes the performance of the lambda sensor in natural gas service, and the complex thermochemical processes that create the sensor output voltage, serve as the primary motivation for this work.

Several studies demonstrate that the heart of the lambda sensor problem is that the gas sensed at the sensor electrode does not have the same chemical composition as the gases in the exhaust stream (Brailsford et al., 1996). This difference can cause sensor "deception," and comes from the different mass diffusion rates of the various gas constituents through the protective layer. Additionally, and potentially more importantly, the sensor voltage responds to the equilibrium oxygen concentration on the sensor electrode instead of the free oxygen in the exhaust gases (Cottrill , 1999). Consequently, the lambda sensor is very sensitive not only to the oxygen content, but also to the other gas species in the exhaust stream (Vosz et al., 2006).

For these reasons, the development of a parametric model of the lambda sensor will allow researchers to understand the thermochemical physics that relate the sensor voltage response to the exhaust gas mixture. Furthermore, some have found that methane gases may escape the combustion chamber and could potentially affect the sensor output voltage. Modeling the thermochemical processes that occur at the sensor will enhance our understanding of the relationship between the sensor output voltage and the exhaust gas composition. This improved understanding can then serve as the "lambda sensor Rosetta stone" to more accurately control the air-to-fuel ratio (*AF*) for improved NSCR/AFRC performance.

Model Governing Equations

This part of the literature review presents the governing equations that are used to model the lambda sensor. The governing equations are divided into three categories which represent the three main processes that occur within the sensor. These main processes are:

- Diffusive mass transfer through the sensor protective layer;
- Heterogeneous catalytic reactions on the sensor platinum electrode; and
- Electrochemical process through the sensor electrolyte material.

Multi-Component Mass Transfer

There are two approaches for modeling multi-component mass transfer: the Maxwell-Stefan equation and Fick's law. According to many references dealing with multi-component mass transfer such as Taylor et al. (1993) and Wesselingh et al. (2006), the Maxwell-Stefan equation is the most reliable tool to model mass transfer in multi-component system. They showed that this equation is capable of handling multi-component mass transfer accurately when compared to models using Fick's law. Fick's law has many limitations and is not physically applicable to a wide array of mass transfer problems.

The Maxwell-Stefan equation is based on the kinetic theory of gases, and the detailed derivation can be found in Taylor et al. (1993). This equation is more general than Fick's law. As an example, it can include any kind of driving force such as chemical potential, pressure gradient, or external body forces. However, in Fick's law the main driving force is only the concentration gradient. Also, the Maxwell-Stefan equation clearly differentiates between the use of diffusive flux and convective flux. The Maxwell-Stefan equation was the first to distinguish between the concept of mass transfer due to convection and diffusion. This was clearly mentioned by Maxwell himself in his 1860 quote that "Mass transfer is due partly to the motion of translation and partly to that of agitation" (Philip, 2008). Cussler (1984) mentioned that the Maxell-Stefan equation is the only form that separates diffusion from convection in a simple way, however the mathematical difficulty of solving this equation is the main problem in using this equation compared to Fick's law.

The general form of the Maxwell-Stefan equation for a multi-component system composed of n species is expressed as:

$$(J_i) = -C_t\,[B]^{-1}(\nabla x_i) \tag{2-22}$$

where

(J_i) The vector of diffusive fluxes for n-1 species

C_t The total molar concentration

(∇x_i) The vector of concentration gradient

The matrix $[B]$ is a square matrix of rank n-1. The elements of this matrix are calculated using the following expression (Taylor et al., 1993):

For diagonal elements

$$B_{ii} = \frac{x_n}{D_{in}} + \sum_{k=1(i\neq k)}^{n} \frac{x_k}{D_{ik}} \tag{2-23}$$

For off-diagonal elements

$$B_{ij} = -x_i \left(\frac{1}{D_{ij}} - \frac{1}{D_{in}}\right) \tag{2-24}$$

The Maxwell-Stefan equation was rewritten in a matrix form explicitly for diffusive fluxes J. The length of this vector is n-1 because the J_n can be determined from the fact that the diffusive fluxes sum to zero:

$$\sum_{i=1}^{n} J_i = 0 \tag{2-25}$$

Through the sensor protective layer, the driving forces are only concentration gradients that can be expressed as the difference between the mole fraction x_i of each constituent of different exhaust gases. The matrix $[B]$ is composed of molar fractions x_i and the binary diffusion coefficient D_{ij} which are obtained when specie i diffuses into j in a binary system. It is worthy to mention here that one of the main advantages of using the Maxwell-Stefan equation is the use of binary diffusion coefficient even when the system is composed of multi-component species. The

diffusion coefficients used in Fick's law for multi-component systems are completely different than what were used in binary systems, creating another difficulty in using Fick's law for a multi-component system. The main disadvantages of using Fickian diffusion coefficients in multi-component systems can be summarized in the following points:

- The diffusion coefficient D_{ij} used in multi-component systems is not the same as that used in binary systems;
- It strongly depends on the concentrations of the mixture species;
- It depends on the species order, which is not a true physical attribute;
- It is not symmetrical $D_{ij} \neq D_{ji}$; and
- It can be negative or positive and again has no physical meaning.

The formula used to calculate the diffusion coefficients was found in Reid et al. (1987). This equation estimates the diffusion coefficient D_{ij} of binary gas systems as proposed by Fuller et al. (1966). The parameters used in this equation were determined by regression analysis of experimental data. The porosity/tortuosity factor is incorporated in this equation to account for the hindrance of the diffusion process that occurs in the ceramic porous material. The equation of binary diffusion coefficients can be expressed as:

$$D_{ij} = \frac{\varepsilon}{q} \frac{0.0143\, T^{1.74}}{P\sqrt{M_{i,j}}\left[\Sigma_{v,i}^{1/3} + \Sigma_{v,j}^{1/3}\right]^2} \quad \textbf{(2-26)}$$

where

$\frac{\varepsilon}{q}$ Porosity/tortuosity factor

T Exhaust gas temperature

P Exhaust gas pressure

$M_{i,j}$ Average Molecular weight $\frac{2}{\frac{1}{M_i}+\frac{1}{M_j}}$

$\Sigma_{v,i}$ Diffusion volume of species *i*

The diffusion of exhaust gases through the protective layer is governed by continuum mechanics instead of Knudsen diffusion. Knudsen diffusion is mainly applied when the molecular mean free path is large compared to the average pore diameter. This means that the diffusion is controlled by molecule-wall collision instead of the collision between the molecules themselves, which occur in continuum mechanics. Knudsen diffusion is typically applied when the gas density is very low or if the pores are very small. Because these two conditions are not satisfied for the lambda sensor, the assumption of continuum mechanics or normal diffusion is considered valid. (Hines at al., 1985)

The species mass transfer through the sensor protective layer is governed by the mass conservation equation. The mass conservation of each exhaust gas species *i* is written as (Bird et al., 2002):

$$\frac{\partial C_i}{\partial t} + \nabla . J_i = 0 \qquad \textbf{(2-27)}$$

where

C_i The molar concentration of species *i*

J_i The diffusive flux of species *i*

Heterogeneous Catalytic Reaction

The catalyst can be defined as any substance that increases the rate of reaction toward equilibrium without being appreciably consumed in the process (Satterfield et al., 1991). The catalyst changes the reaction rate by promoting a different molecular path ("mechanism") for the reaction. For example, Fogler et al. (1999) mentioned that gaseous hydrogen and oxygen are virtually inert at room temperature, but react rapidly when exposed to platinum. Figure 2.10 shows the influence of a catalyst on the reaction path and how it reduces the activation energy barrier to form water vapor.

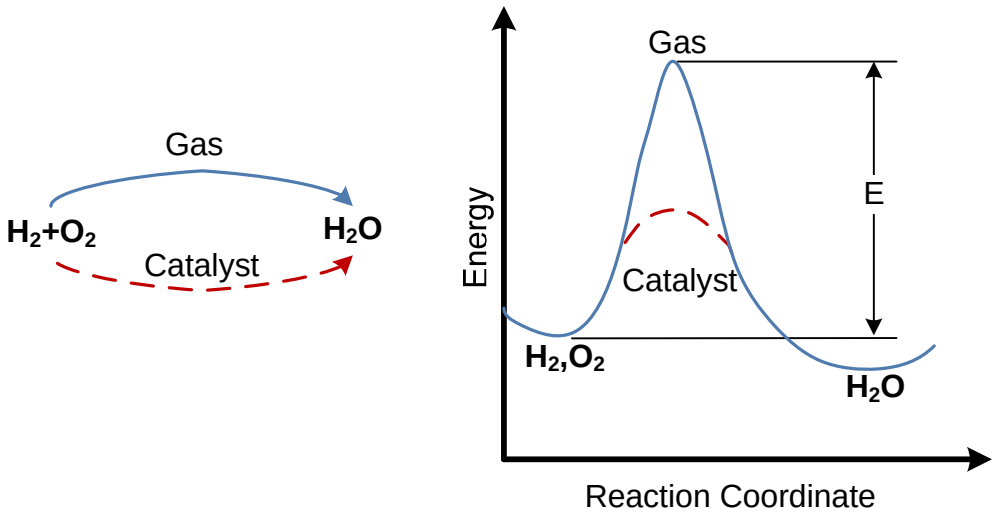

Figure 2.10 Reaction Paths (Fogler et al., 1999)

Heterogeneous catalysis refers to the kind of catalytic reactions where the reactants and products are in one phase (usually gas) and the catalyst is in another phase (usually solid). Heterogeneous catalytic reactions are very complex reactions. These kinds of reactions are composed of several steps. For the catalytic process to take place, the reactants must be transported to the catalytic surface. Thus, there are many steps that affect the overall reaction rate, such as diffusion, adsorption, chemical reaction, and desorption. Figure 2.11 illustrates the main processes of any heterogeneous catalytic reaction (Fogler et al., 1999). These processes are summarized in the following steps:

- Mass transfer of the reactants from the bulk flow to the catalytic surface
- Internal diffusion of the reactants into the pore
- Adsorption of the reactants onto the catalytic surface
- Chemical reaction on the catalytic surface
- Desorption of the product from the surface
- Diffusion of the product from the catalytic surface to the pore
- Mass transfer of the product from the pore to the bulk flow

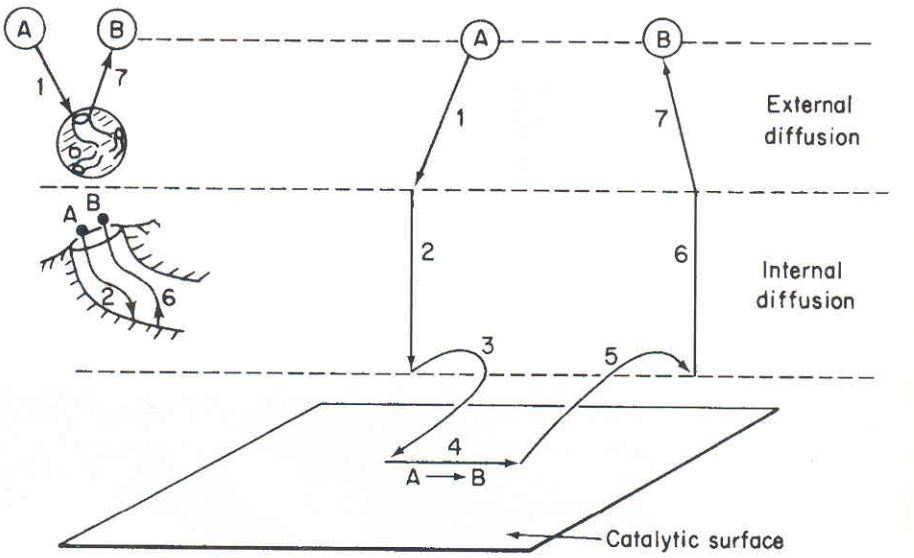

Figure 2.11 The Main Steps of Heterogeneous Catalytic Reaction (Fogler et al., 1999)

The kinetics of heterogeneous catalytic reactions can be modeled using two different mechanisms (Hagen, 2006), which are:

- Langmuir-Hinshelwood Mechanism (1921), and
- Eley-Rideal Mechanism (1943)

Figure 2.12 shows a schematic of Langmuir-Hinshelwood mechanism. The Langmuir-Hinshelwood (LH) mechanism is based on the reaction between two adsorbed species on the catalytic surface. For example, if A and B are the reactants in the gas phase, the reactants will be adsorbed into the catalyst active sites, after which these adsorbed molecules A* and B* react together to form adsorbed product C*. Finally, the adsorbed product will be desorbed back into the gas phase C. the reaction sequence is thus:

- Adsorption: $A \rightleftharpoons A^*$ and $B \rightleftharpoons B^*$
- Reaction: $A^* + B^* \rightleftharpoons C^*$
- Desorption: $C^* \rightleftharpoons C$

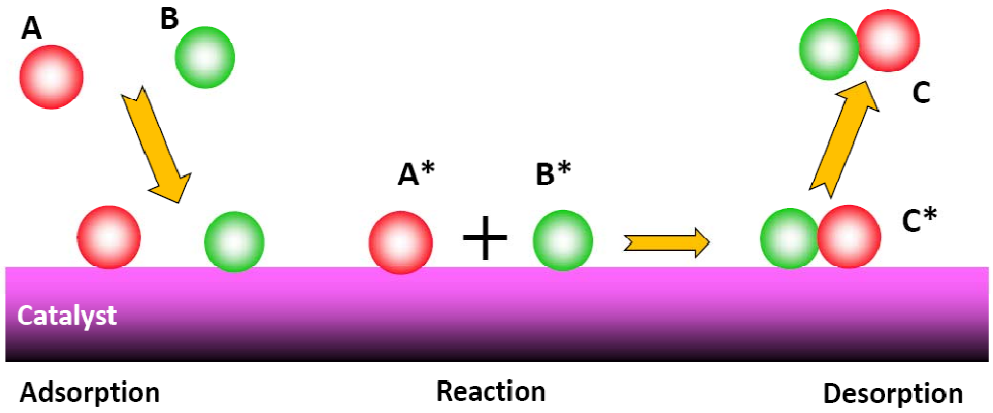

Figure 2.12 Schematic of Langmuir-Hinshelwood Mechanism

Figure 2.13 shows a schematic of Eley-Rideal mechanism. The Eley-Rideal mechanism is based on the reaction between a partner which is still in the gas phase and the other partner which is adsorbed into the catalytic surface. For example, if A and B are the reactants in the gas phase, A will be adsorbed into the catalytic surface to form A*. B, which is in the gas phase, hits the adsorbed molecule A* and a reaction takes place to form C*. Finally, the adsorbed product C* is desorbed back into gas phase C. The reaction sequence is:

- Adsorption: A ⇌ A*
- Reaction: A* + B ⇌ C*
- Desorption: C* ⇌ C

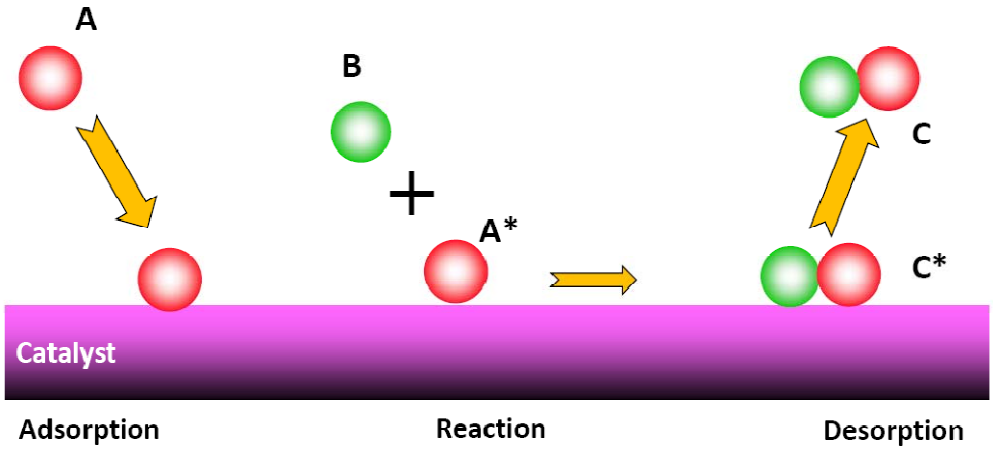

Figure 2.13 Schematic of Eley-Rideal Mechanism

The Langmuir-Hinshelwood scheme is the most commonly used kinetic expression to explain the kinetics of heterogeneous catalytic reactions (Kumar et al., 2008). Based on the EGO sensor literature review, most of the reactions that occur on the sensor platinum electrode are modeled using the Langmuir-Hinshelwood mechanism. Therefore, the research team used this mechanism to model all the kinetic reactions on the platinum electrode.

The occupancy or coverage θ_i refers to the fraction of the active sites on the catalytic surface occupied by species *i*. For instance, if the total number of sites is *N* and there are N_A sites covered by species A, then the occupancy θ_A of species A is equal to N_A/N. The time rate of change of occupancy of each species *i* on the noble platinum electrode is calculated according to:

$$\frac{\partial \theta_i}{\partial t} = r_a - r_d + \sum_j (\nu_{i,j} r_{i,j}) \quad \textbf{(2-28)}$$

where

r_a The adsorption rate

r_d The desorption rate

$\nu_{i,j}$ The stoichiometric coefficient between species *i* and *j*

$r_{i,j}$ The reaction rate between species *i* and *j*

The adsorption rate r_a depends on the concentration C_i of species *i* in the gaseous phase, the availability of free surface sites θ_V, and on the exhaust gas temperature *T*: (Auckenthaler, 2005)

$$r_{a,i} = s \sqrt{\frac{R_u T}{2\pi M_i}} \frac{\theta_V C_i}{L_{elec}} \quad \textbf{(2-29)}$$

where

s Sticking probability (correction factor)

R_u The universal gas constant

L_{elec} The electrode adsorption capacity

θ_V Surface vacancy =$1 - \sum_i \theta_i$

The desorption rate $r_{d,i}$ is a function of the occupancy θ_i and the sensor temperature T_{sensor} according to the Arrhenius-Ansatz equation: (Auckenthaler, 2005)

$$r_{d,i} = k_d \exp\left(\frac{-E_d}{R_u T_{sensor}}\right)\theta_i \quad \textbf{(2-30)}$$

where

k_d The desorption pre-exponential factor

E_d The desorption activation energy

The reaction rate $r_{i,j}$ depends on the occupancies θ of the reactants *i* and *j*, and on the sensor temperature: (Auckenthaler, 2005)

$$r_{i,j} = k \exp\left(\frac{-E}{R_u T_{sensor}}\right)\theta_i\theta_j \quad \textbf{(2-31)}$$

where

k The reaction pre-exponential factor

E The reaction activation energy

Methane Catalytic Reactions

There are many research groups working to model methane catalytic reactions. For example, Hickman et al. (1993) proposed a model for methane catalytic reaction on platinum surface. In this model, methane is assumed to be directly adsorbed into five vacant sites of the catalytic surface producing one carbon atom and four hydrogen atoms. Deutschmann et al. (1996) published a series of extensive work on modeling methane catalytic reactions.

Deutschmann extended Hickman model and assumed that methane adsorption occurs according to the following reactions (Deutschmann et al., 1996):

$$CH_4 + 2* \rightarrow CH_{3s} + H_s \quad \textbf{(2-32)}$$

$$CH_3 + 2* \rightarrow CH_{2s} + H_s \quad \textbf{(2-33)}$$

$$CH_2 + 2* \rightarrow CH_s + H_s \quad \textbf{(2-34)}$$

$$CH + 2* \rightarrow C_s + H_s \quad \textbf{(2-35)}$$

According to the Deutschmann scheme, methane is first adsorbed into the catalytic surface forming two species CH_3 and H. Following this step, a series of three sequential surface reactions occur for CH_3 dissociation. Therefore, the methane reactions will finally result in four adsorbed atoms of hydrogen and one adsorbed carbon atom into the platinum catalytic surface.

The research team examined both Hickman and Deutschmann schemes. The Hickman scheme is less complex and reduces the required computational resources. Using this reaction eliminates three additional equations that represent the mass balance of the three constituents CH_3, CH_2 and CH. Because the main goal of this study is to develop a solution scheme that can be used in model-based control, which is suitable for NSCR controller, the research team used the Hickman model.

Electrolyte Material

The literature review showed that there are many approaches that can be applied to simulate the electrolyte material. The simplest approach considers the oxygen concentration on the electrode and the transition of oxygen between the electrode and the electrolyte based on the concentration gradient only. A second approach takes into account the direct reactions of reducing species on the electrode. It suggests another oxygen transition driving force which is the chemical potential of the reduction-oxidation reactions that occur on the electrode. Yet a

third approach based on incorporating the adsorption of various species on the electrolyte itself. According to Auckenthaler's study (2005), the second approach provides excellent accuracy compared to the other two methods and, hence, this modeling study used only the second approach since it is the most accurate one.

The output potential difference between the sensor electrodes can be calculated using the Nernst equation. The general form of the Nernst equation is written as (Brailsford et al., 1996)

$$V = \frac{R_u T}{mF} ln \frac{\mathbb{C}_v}{\mathbb{C}_{v,ref}} \quad \textbf{(2-36)}$$

where

R_u The universal gas constant

T The sensor temperature

m number of electrons exchanged in the reaction

F Faraday's constant

$\mathbb{C}_v$ The vacancy concentration of the electrolyte material at the exhaust gas electrode

$\mathbb{C}_{v,ref}$ The vacancy concentration of the electrolyte material at the reference gas electrode

The concept behind the Nernst equation is to balance the chemical potential with the electrostatic potential in the electrolyte. This equation is the governing equation of a wide range of thermo-chemistry applications. The simple approach for applying the Nernst equation to the lambda sensor is mainly based on the adsorption of oxygen on the electrolyte material according to the reaction:

$$O_s + v_O^{2+} + 2e^- \rightleftharpoons O_o \text{ (oxide)} \quad \textbf{(2-37)}$$

where

O_s Adsorbed oxygen atom

v_O Oxide positive vacancy

e Electron

O_o Oxygen ion in the electrolyte

Brailsford et al. (1996) extended this simple reaction by including the effect of other adsorbed reducing species on the electrode such as CO and H_2. These reactions are:

$$CO_s + v_O^{2+} + 2e^- \rightleftharpoons CO_o + O_o \text{ (oxide)} \quad \textbf{(2-38)}$$

$$OH_s + v_O^{2+} + 2e^- \rightleftharpoons H_s + O_o \text{ (oxide)} \quad \textbf{(2-39)}$$

The above two reactions in addition to the simple oxygen reaction can be used to determine the output voltage as derived in Auckenthaler's study (2005). The final equation used to determine the sensor voltage taking into account the effect of reducing species is:

$$V = \frac{R_u T}{2F} ln \left[\frac{\theta_{O,ref}(\theta_v + \mathcal{K}_{COf}\theta_{CO} + \mathcal{K}_{Hf}\theta_H)}{\theta_{v,ref}(\theta_O + \mathcal{K}_{Hb}\theta_{OH})} \right] \quad \textbf{(2-40)}$$

where

$\mathcal{K}_{COf}$ The ratio between the forward reaction coefficients of CO and O

$\mathcal{K}_{Hf}$ The ratio between the forward reaction coefficients of H and O

$\mathcal{K}_{Hb}$ The ratio between the backward reaction coefficients of CO and O

In this study, the third approach which accounts for the adsorbed species into the electrolyte material was not used since it does not provide a more accurate result compared to the second approach, in addition to the complexity of its calculations.

Chapter 3 - NSCR Field Testing

This chapter describes work conducted by Kansas State University's National Gas Machinery Laboratory and Innovative Environmental Solutions, Inc. to characterize pollutant emissions performance of field gas-fired four-stroke cycle rich burn (4SRB) engines equipped with non-selective catalytic reduction (NSCR) technology. This field testing study was conducted as a part of a comprehensive project funded by U.S. Department of Energy (DOE) "Cost-Effective Reciprocating Engine Emissions Control and Monitoring for E&P Field and Gathering Engines" (DOE Award DE-FC26-02NT15464). Emissions and engine data were collected semi-continuously with portable emissions analyzers on three engines in the "Four Corners" area. These three engines were retrofitted with NSCR systems. The emissions were monitored during the period between October 2007 and December 2008. The objectives of this field testing study were to:

1. Identify the reliable (i.e., day-in and day-out) capabilities of currently-available NSCR/AFRC systems;
2. Characterize emissions including NO_x, ammonia, and the NO_x /ammonia (NH_3) trade-off; and
3. Identify and advance the understanding of AFRC limitations.

In addition, a mapping study was conducted on one engine. The NSCR was operated at various controlled air-to-fuel ratios (*AF*) while emission measurements were conducted and engine operating parameters monitored. NO_x, CO, and oxygen were measured using both EPA reference method technology and the portable analyzer used in the long-term study. In the mapping study, ammonia, formaldehyde, and speciated hydrocarbon emissions were recorded in real-time using an extractive Fourier-transform infrared spectroscopy (FTIR) analyzer.

Long-Term Emissions Performance of NSCR Systems

This project was prompted by increasingly strict environmental regulations that require engine owners and operators to apply emissions controls to their engines. Although small engines less than 500 hp had not been regulated in most cases in the past, new, modified, and reconstructed spark ignited engines are now subject to the New Source Performance Standard (NSPS) regardless of the engine size. These regulations have caused concern because many

emissions control technologies typically applied to larger engines have not been proven for small engines. Thus, it is unknown whether these technologies will impose additional performance challenges on smaller engines.

In addition to these federal regulations, state agencies such as those in Colorado, New Mexico, and Wyoming have started to focus on emissions from reciprocating engines below 50 bhp. Until now, these smaller engines have not been regulated. At present, the region with the greatest confluence of emissions concerns is the Rocky Mountain and Intermountain West area, where significant concerns about regional haze control have accelerated the implementation of NO_x and fine particulate regulations that are only pending in many other producing areas. However, the incremental adoption of regulations state-by-state, as well as the proximity of many remote production areas in the Southwest to National Parks and Class I Wilderness Areas (which are protected airsheds) may likely stimulate aggressive compressor engine controls in that and other production regions. Finally, the East Texas and Louisiana regions are subjected to conventional ambient ozone concerns, and have promulgated strict NO_x controls for reciprocating engines.

Technical Approach

Three engines in northwestern New Mexico and southwestern Colorado were retrofitted with NSCR control systems and equipment for semi-continuous monitoring. All engines are located between 5,000 and 6,100 ft above sea level. The continuously monitored engines are rated at 57 hp (Engine 1), 23 hp (Engine 2), and 1,467 hp (Engine 3), as listed in the end-user documentation. In addition to semi-continuous monitoring, Engine 1 was also mapped over the range of its operating conditions. All engines are used to compress natural gas at a wellhead or a main compression site. Engines 1 and 2 use Emit Technologies single round, foil, 8-inch catalysts with a 0.5-inch control valve and EDGE-NG AFRC. Engine 3 uses a QUICK-LID Model DC74-12 catalyst and a dual-bank-controlling Altronic EPC 110 AFRC. All catalysts were believed to be in good working condition when the data collection began at each site. However, the catalyst on Engine 1 was replaced once because reduced conversion efficiency indicated the catalyst had been damaged. The catalyst was replaced again when the engine was replaced with an identical, rebuilt model. This engine replacement occurred because the number of engine operating hours (between 46,000 and 54,000 hours) exceeded the limits recommended

by Emit (35,000 to 40,000 hours) in order to maintain successful emissions control. The catalyst was replaced at this time to ensure that any unusual combustion products that might have been produced by the older engine did not reduce the effectiveness of emissions reduction on the rebuilt engine. Semi-continuous monitoring began on Engines 1 and 2 in October of 2007 and on Engine 3 in May of 2008. The mapping of Engine 1 was completed in June of 2008 (Toema et al., 2009).

Semi-Continuous Monitoring Techniques

Semi-continuous monitoring was conducted to characterize the day-in, day-out emissions of the NSCR-outfitted engines at their operating conditions. To do this effectively, emissions, engine operating conditions, and ambient conditions were measured, as shown schematically in Figure 3.1. All data was stored on-site in a data acquisition controller and downloaded through cellular modems to the NGML every four hours.

Emissions were measured using a Testo 350 XL portable gas analyzer with four electrochemical cells that measure CO, NO, NO_2, and O_2. When using a portable analyzer in continuous mode, it is necessary to purge the cells with air between measurements to prevent cell poisoning and drift. Thus, "continuously" collected data are really collected only semi-continuously. The cycle between purge and measurement time has been shown to maintain measurement quality in a long-term study (Beshouri, 2006). Additionally, the instrument is run in 10-times dilution mode to protect the CO cell from over-threshold exposure, which will irreversibly damage the cell (Beshouri, 2006). The analyzer, cellular modem, and data acquisition system are housed in temperature-controlled instrument enclosures to ensure data quality and to protect them from the elements.

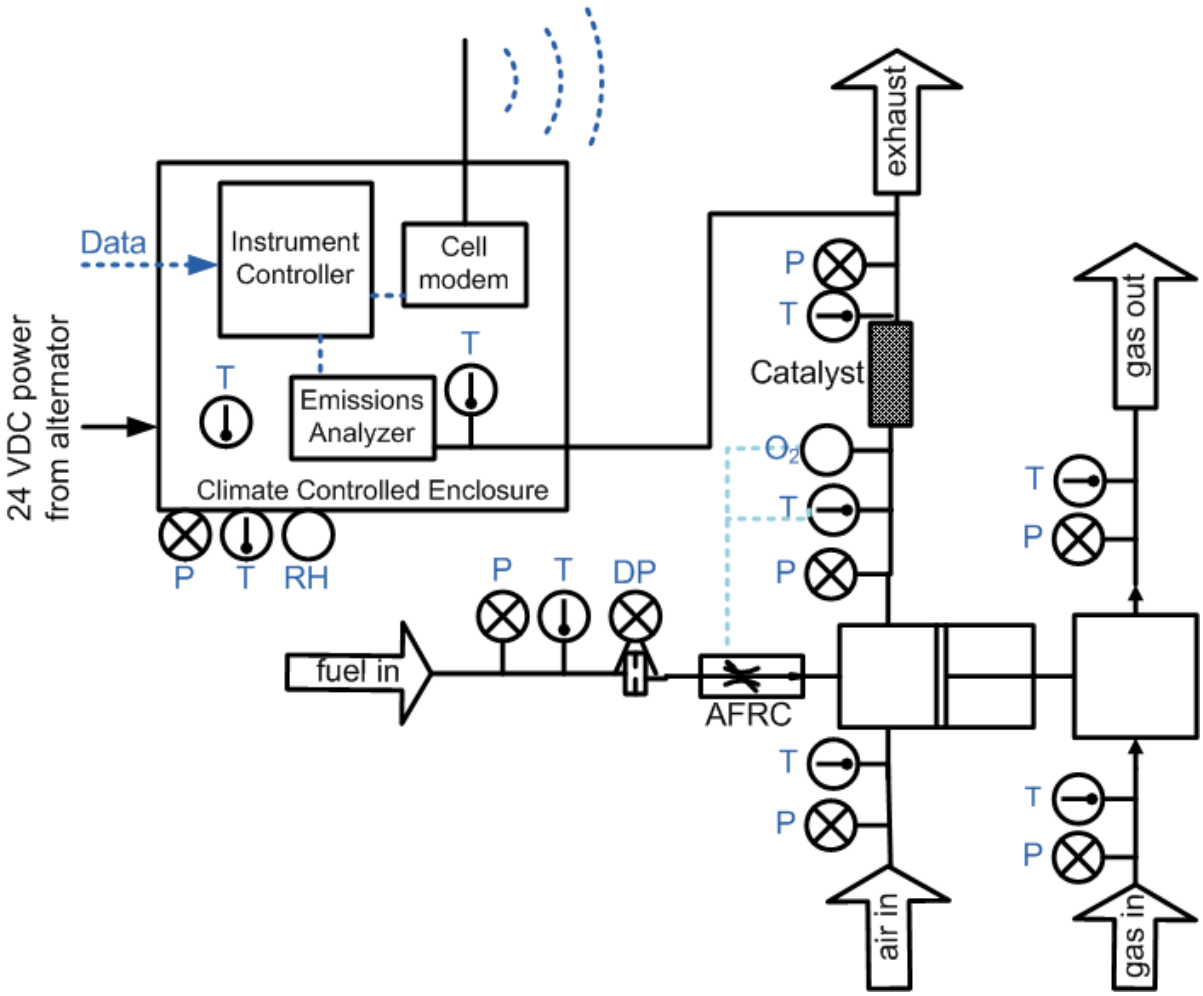

Figure 3.1 Parameters measured on continuous engines.

Long-Term Data Analysis of NSCR Systems

The goal of this study is to evaluate the capability of currently available NSCR/AFRC systems to reliably control NO_x and CO emissions from natural gas production engines. The exhaust emissions were monitored semi-continuously to determine the emissions levels that are consistently and reliably achieved. Table 3-1 summarizes the data collected from all three engines.

Table 3-1 Summary of data collected.

Engine Site	Data Collection Start Date	Operating Days	Days of Data Collection	Minutes of Data Collected
Engine 1	10/17/2007	383	227	94,244
Engine 2	11/31/2007	338	104	30,360
Engine 3	5/22/2007	226	144	63,353

As shown in Table 3-1, data was not collected on all days due in part to equipment problems such as analyzer malfunction from insufficient power or condensation buildup, engine down time, and difficulties with the cellular service provider. The data in this analysis set was collected over a number of seasonal conditions. For the purposes of this study, winter (the cold season) is considered to last from November through March, summer (the warm season) is considered to last from June through September, and the rest of the year is considered to be fall/spring (a season of intermediate temperatures). The portion of data collected during each seasonal condition is shown in Table 3-2. Because data collection was changed from 15 minutes out of the hour to 30 minutes out of the hour starting during the summer 2008, and there were fewer difficulties with equipment during the summer, more data was collected during warm conditions than any other conditions.

Table 3-2 Seasonal conditions for data collected

Engine Site	Summer	Fall/Spring	Winter
Engine 1	36%	31%	33%
Engine 2	31%	44%	25%
Engine 3	81%	19%	0%

Data Bin Analysis

Tables 3-3, 3-4, and 3-5 show binned emissions data for each of the three engines used during this study. Uncertainty levels for these tables were estimated by considering the precision with which each data point was placed into the correct emissions level category and estimating what percentage of measured data could have been placed into a neighboring category. This procedure was used for all binned data.

Table 3-3 summarizes emissions of Engine 1 from October 17, 2007 to November 3, 2008. The table shows the percentage of data points that fit into one of twelve emission level categories based on CO and NO emissions. The mass emissions (g/hp-hr) were based on measured concentrations and estimated engine ratings and operating parameters. For this engine and operating conditions: 0.5 g/hp-hr NO corresponds to approximately 90 ppm NO, 1 g/hp-hr corresponds to approximately 180 ppm, and 2 g/hp-hr corresponds to approximately 360 ppm. For CO, 2 g/hp-hr corresponds to approximately 591 ppm, and 4 g/hp-hr corresponds to approximately 1,182 ppm. Simultaneous control of NO to less than 0.5 g/hp-hr and CO to less than 2 g/hp-hr was achieved for less than 14% of the total monitoring time.

Table 3-4 shows the same information for Engine 2 from November 30, 2007 to November 3, 2008. (The analyzer was not communicating with the data acquisition system from July 13 to August 15, 2008.) For this engine and operating conditions: 0.5 g/hp-hr NO corresponds to approximately 92 ppm NO, and 1 g/hp-hr corresponds to approximately 183 ppm, and 2 g/hp-hr corresponds to approximately 366 ppm. For CO, 2 g/hp-hr corresponds to about 601 ppm, and 4 g/hp-hr corresponds to approximately 1,202 ppm. As at engine 1, the simultaneous control of NO to less than 0.5 g/hp-hr and CO to less than 2 g/hp-hr was achieved for less than 14% of the time emissions were monitored.

Table 3-5 shows the same information for Engine 3 from May 22, 2008 to January 1, 2009. For this engine and operating conditions: 0.5 g/hp-hr NO corresponds to about 138.3 ppm NO, and 1 g/hp-hr corresponds to about 276.6 ppm, and 2 g/hp-hr corresponds to about 553.2 ppm. For CO, 2 g/hp-hr corresponds to about 908 ppm, and 4 g/hp-hr corresponds to about 1,816 ppm. This table shows a difference between Engine 3 and the other two engines. The simultaneous control of NO to less than 0.5 g/hp-hr and CO to less than 2 g/hp-hr was achieved for less than 38% of the time compared to 14% for the other two engines. The Engine 3 system was capable of controlling CO emissions below 2 g/hp-hr with all NO levels for 97% of the time

while it can control NO emissions to less than 0.5 g/hp-hr with all CO emission levels for less than 40 % of the time. Engine 2 controlled NO to less than 0.5 g/hp-hr for all CO levels for approximately 63% of the time compared to 40% for Engine 3 and 31% for Engine 1. The observations were that the Engine 2 system appears to be more capable of controlling NO when compared to the other two engines.

The major observations between the emissions levels at Engine 2 and the emissions levels at Engine 1 are that Engine 2 had NO levels above 0.5 g/hp-hr for a smaller percentage of the time monitored. In addition, CO levels were in the 2 g/hp-hr to 4 g/hp-hr range for a significantly smaller fraction of the time, and CO levels were over 4 g/hp-hr for a higher percentage of time compared to Engine 1. This suggests a difference between the two engines running the same control system, which could be a result of engine model or size, EGO set point tuning, fuel composition, convenience of access to adjust problematic conditions, or a number of other factors.

Table 3-3 Engine 1 semi-continuous data summary.

	CO < 2 g/hp-hr	2 < CO < 4 g/hp-hr	CO > 4 g/hp-hr	All CO levels
NO_X < 0.5 g/hp-hr	14%	9%	8%	**31%**
0.5 < NO_X < 1 g/hp-hr	6%	1%	7%	**14%**
1 < NO_X < 2 g/hp-hr	8%	2%	19%	**29%**
NO_X > 2 g/hp-hr	12%	1%	13%	**26%**
All NO_X levels	**40%**	**1%**	**47%**	**100%**

Table 3-4 Engine 2 semi-continuous data summary.

	CO < 2 g/hp-hr	2 < CO < 4 g/hp-hr	CO > 4 g/hp-hr	All CO levels
NO_X < 0.5 g/hp-hr	14%	4 %	45%	**63%**
0.5 < NO_X < 1 g/hp-hr	11 %	0.3%	1 %	**12%**
1 < NO_X < 2 g/hp-hr	16%	0.3%	1 %	**18%**
NO_X > 2 g/hp-hr	7%	0.10%	0.10%	**7%**
All NO_X levels	**48%**	**5 %**	**47%**	**100%**

Table 3-5 Engine 3 semi-continuous data summary.

	CO < 2 g/hp-hr	2 < CO < 4 g/hp-hr	CO > 4 g/hp-hr	All CO levels
NO_X < 0.5 g/hp-hr	38%	1.0%	0.9%	**40%**
0.5 < NO_X < 1 g/hp-hr	15%	0.0%	0.0%	**15%**
1 < NO_X < 2 g/hp-hr	11%	0.0%	0.0%	**11%**
NO_X > 2 g/hp-hr	34%	0.11%	0.0 %	**34%**
All NO_X levels	**98%**	**1.1%**	**0.9%**	**100%**

A graphical representation of the simultaneous control capabilities observed for Engine 1 is shown in Figure 3.2. In this figure, each line represents the percentage of time that the CO level was below a certain value for NO levels below a given value. For this engine when the NO level was below 0.5 g/hp-hr, as shown by the bottom-most curve in Figure 2, CO was controlled to below 11 g/hp-hr almost 30% of the time. When the NO level was below 10 g/hp-hr, as shown by the top-most curve in Figure 2, CO was controlled to below 11 g/hp-hr approximately 85% of the time. As can be seen by the closeness of the curves for 6 g/hp-hr through 10 g/hp-hr of NO, little additional time with NO controlled to below a given limit would be gained for this particular NSCR/engine system as it was operated by relaxing the NO limit to greater than 6 g/hp-hr. Similarly, the curves begin to become asymptotically horizontal for CO levels approaching 11 g/hp-hr and the slope of the curves become even closer to zero at CO levels of 18 g/hp-hr. The incremental increase in additional time when CO is controlled to below a given limit gained by relaxing CO limits to above 11 g/hp-hr would be insignificant for this particular NSCR/engine system as it was operated. This particular NSCR/engine system operated within levels simultaneously below 6 g/hp-hr NO and 11 g/hp-hr CO approximately 80% of the time that emissions were monitored.

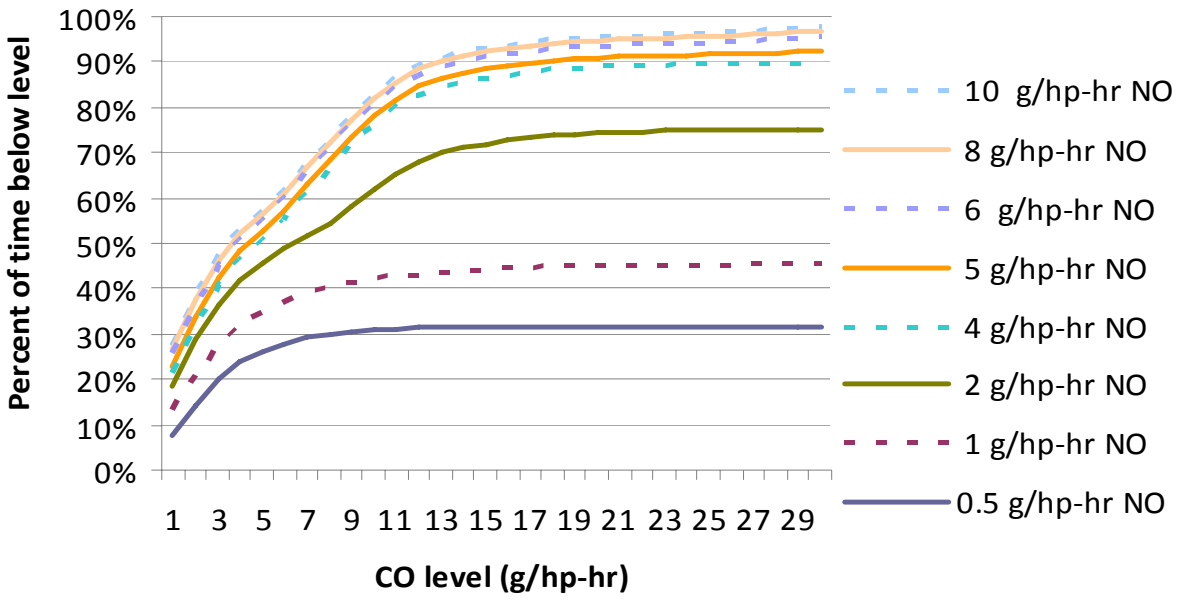

Figure 3.2 CO control at various NO levels for Engine 1

The graphical representation of the simultaneous control capabilities observed for Engine 2 is shown in Figure 3.3. While these curves have the same basic shape as the curves for Engine 1, the initial slope is not as large for Engine 2 and becomes almost horizontal at 15 g/hp-hr of CO level. Additionally, there is decreased spread in the percentage of the time that emissions below various NO levels were detected for Engine 2 compared to Engine 1. For example, as shown by the closeness of the curves for 5 g/hp-hr and 10 g/hp-hr of NO in Figure 3.3, in most instances where NO was controlled to below 10 g/hp-hr, it was also controlled to below 5 g/hp-hr, which indicates that little additional time with NO controlled to below a given limit would be gained for this particular NSCR/engine system as it was operated by relaxing the NO limit to greater than 5 g/hp-hr. Similarly, the slopes of the curves become nearly zero for CO levels greater than 15 g/hp-hr. The incremental increase in additional time when CO is controlled to below a given limit gained by relaxing CO limits to greater than 15 g/hp-hr would be insignificant for this particular NSCR/engine system as it was operated. This particular NSCR/engine system operated within levels simultaneously below 5 g/hp-hr NO and 15 g/hp-hr CO approximately 95% of the time its emissions were monitored and to below 5 g/hp-hr NO and 11 g/hp-hr CO approximately 80% of the time its emissions were monitored.

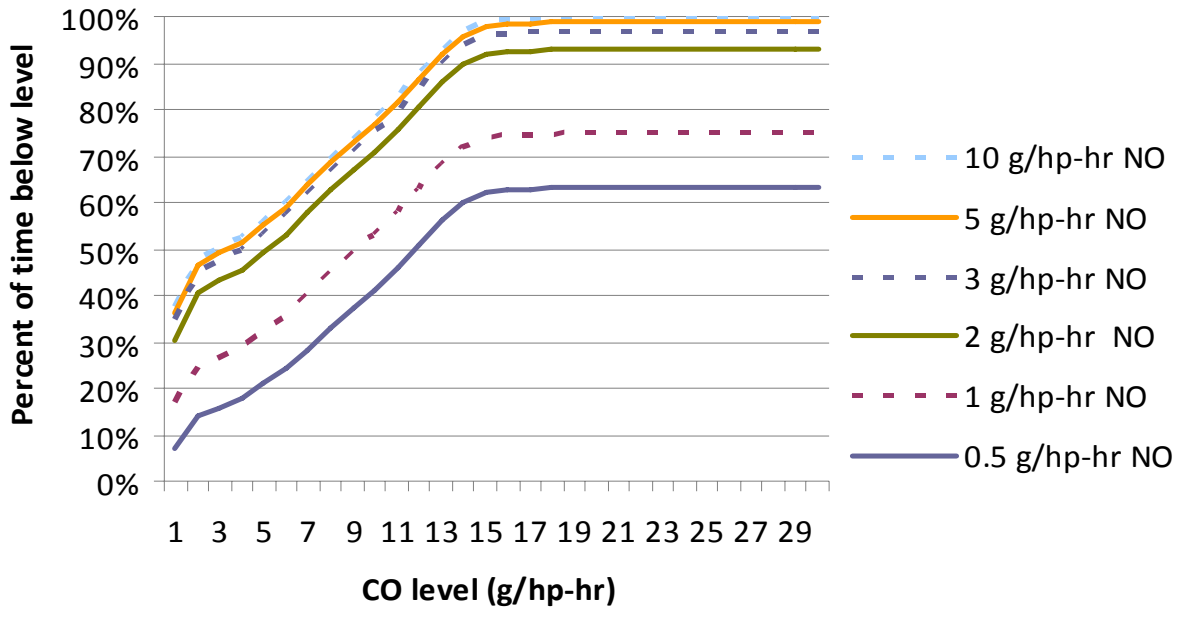

Figure 3.3 CO control at various NO levels for Engine 2

Figure 3.4 shows the graphical representation of the simultaneous control capabilities of Engine 3. The curves that represent the emissions levels appear to be more horizontal compared to the other two engines, as shown from this figure that the percent of time of data collected depends mainly on the NO levels when CO was greater than 5 g/hp-hr compared to 11 g/hp-hr for Engine 1 and 15 g/hp-hr for Engine 2. For Engine 3 when the NO level was controlled below 0.5 g/hp-hr, as shown by the bottom-most curve in Figure 3.4, CO was controlled below 5 g/hp-hr approximately 50% of the time, while this percentage does not exceed 25% of the time for either Engine 1 or Engine 2. For NO levels greater than 10 g/hp-hr, the engine was able to control CO emissions below 5 g/hp-hr approximately 98% of the time.

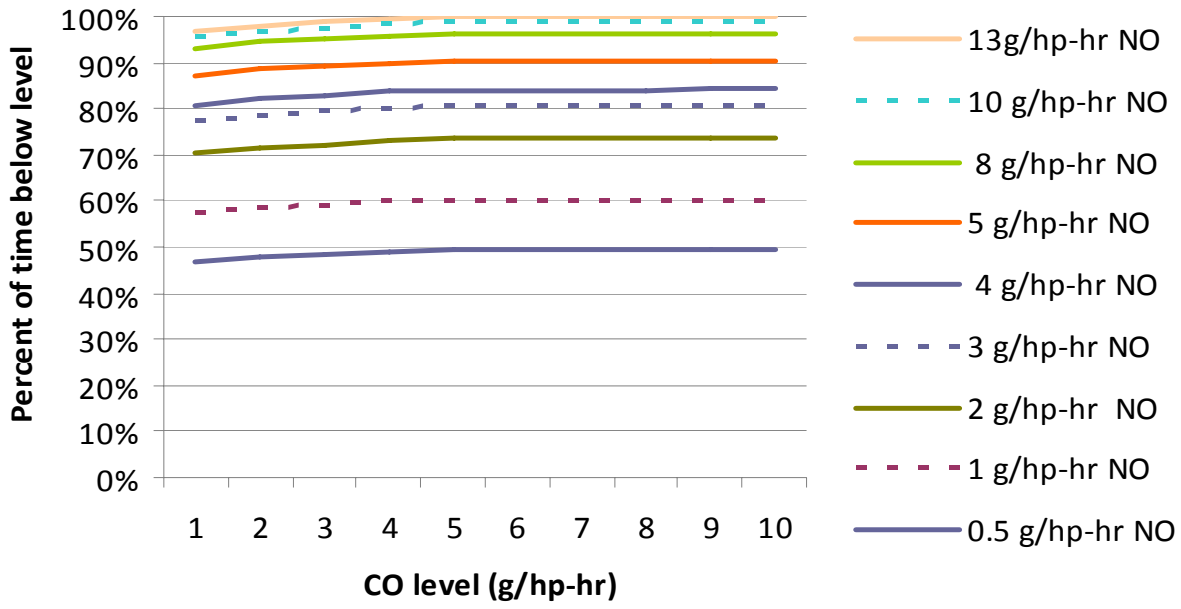

Figure 3.4 CO control at various NO levels for Engine 3

The data indicate that NSCR/AFRC systems are unable to simultaneously control NO_x emissions below a few hundred ppm and CO emissions below 1,000 ppm on a consistent basis. Furthermore, the data show an emissions trade-off. One pollutant may be consistently controlled to a low concentration while the other pollutant tends to vary significantly or remain high. The data also show significant variation of emissions over time spans of a few hours or less, as well as over long-term measurements. Changes in emissions levels often correspond to changes in

measured EGO signal or changes to the EGO set point voltage, which indicate rich or lean AFR excursions.

Seasonal Variation

Dividing the data by season as in Table 3-2 and by emissions level as in Table 3-3 through Table 3-5 reveals differences in seasonal emissions conditions. These differences in NO and CO emissions levels for Engine 1 are shown in Figures 3.5 and 3.6, respectively. As shown in Figure 3.5, more NO values were above 2 g/hp-hr during the winter season while more measured NO values were below 0.5 g/hp-hr than at any other level during the fall/spring and summer seasons. The seasonal CO behavior was different, as shown in Figure 3.6. During the winter season, more CO values were below 2 g/hp-hr than at any other level. However, higher CO emission levels occurred during fall/spring seasons.

Data collected from Engine 2 revealed patterns similar to those seen at Engine 1 when broken down by emissions level and season. As shown in Figure 3.7, during the winter season, more NO measurements were recorded at levels above 2 g/hp-hr than at any other NO level. During the summer season, more NO measurements were recorded at levels less than 0.5 g/hp-hr than at any other NO level. As for Engine 1, the CO data from Engine 2 shown in Figure 3.8 reveals that during the winter, more data was collected at CO levels less than 2 g/hp-hr than at any other level.

The seasonal data for both NO and CO emissions from Engine 3 are shown in Figures 3.9 and 3.10, respectively. The data collected from this engine were acquired only during summer and fall/spring seasons, therefore the influence of winter season on the emissions levels could not be determined. The patterns of both CO and NO emissions show a very similar trend to Engines 1 and 2 during summer and fall/spring seasons. As shown in Figures 3.9 and 3.10, the differences due to seasonal change from summer to fall/spring are not significant (Toema et al.,2009).

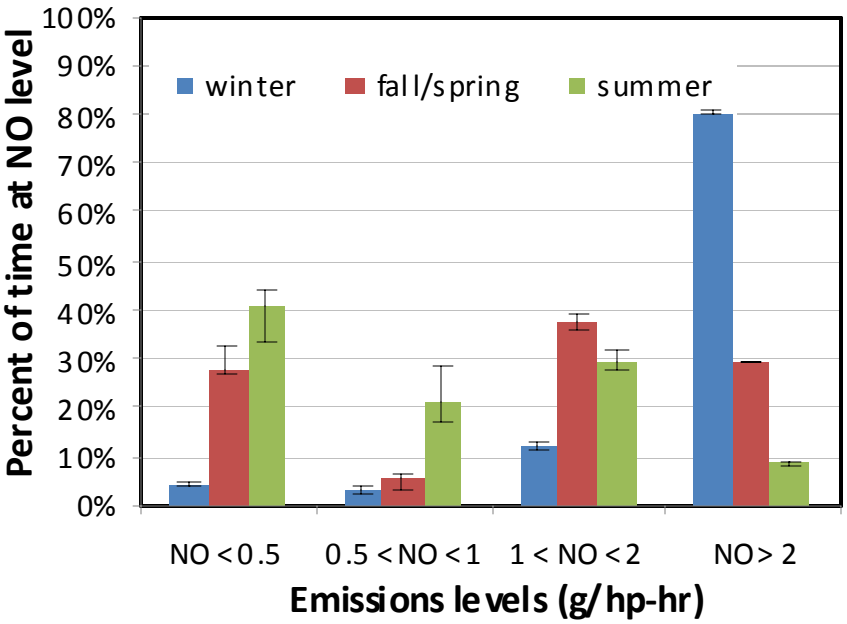

Figure 3.5 Seasonal effect on NO at Engine 1

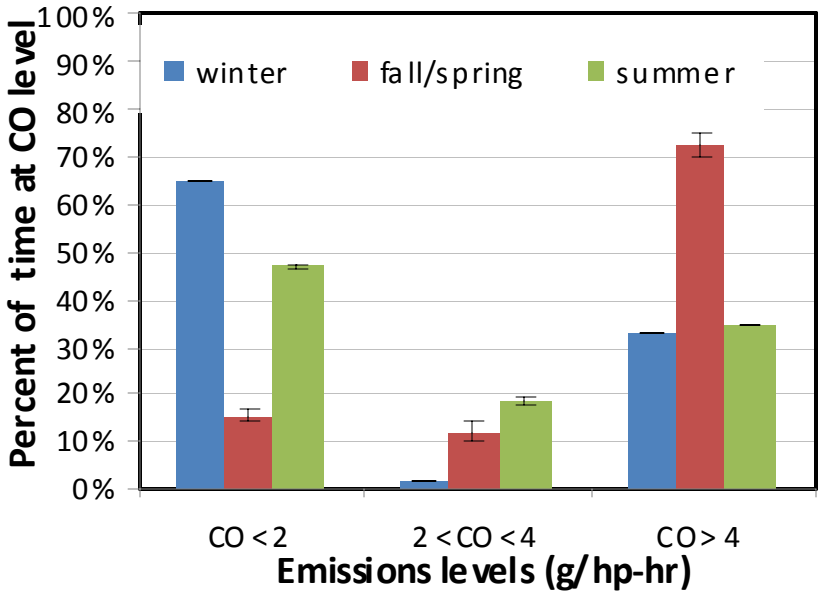

Figure 3.6 Seasonal effect on CO at Engine 1

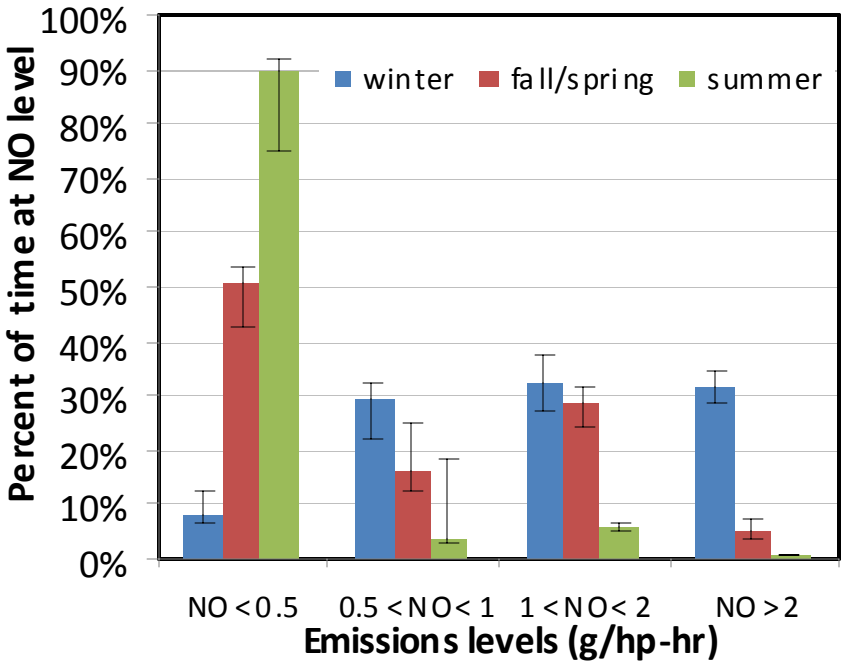

Figure 3.7 Seasonal effect on NO at Engine 2

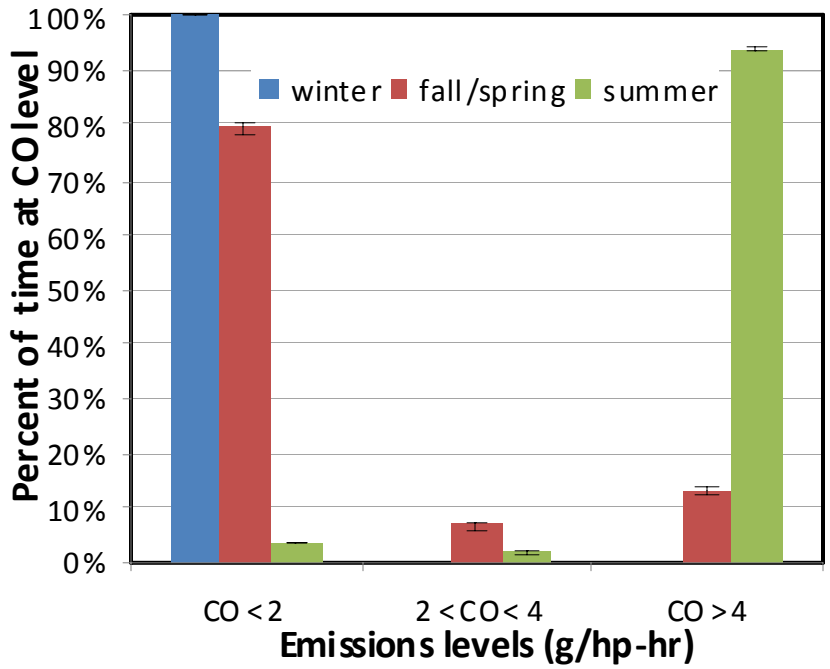

Figure 3.8 Seasonal effect on CO at Engine 2

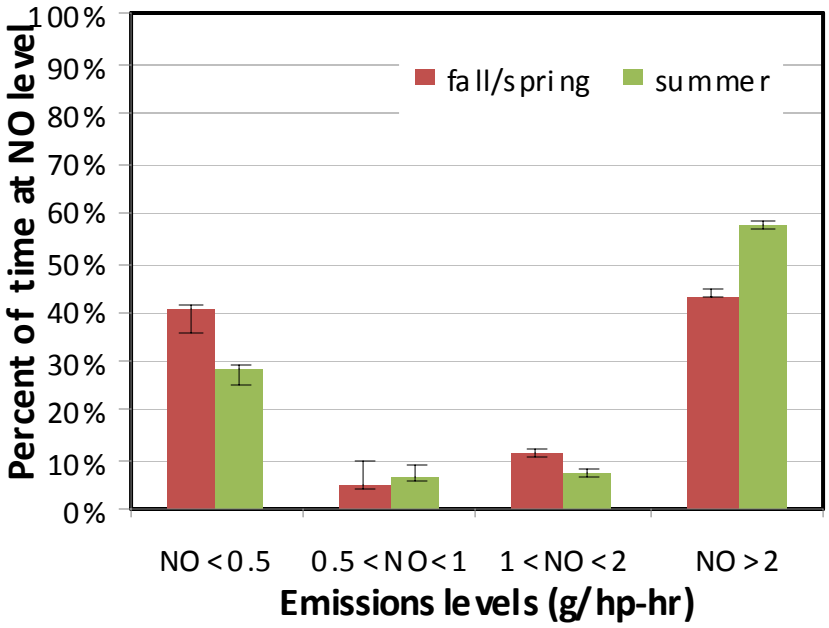

Figure 3.9 Seasonal effect on NO at Engine 3

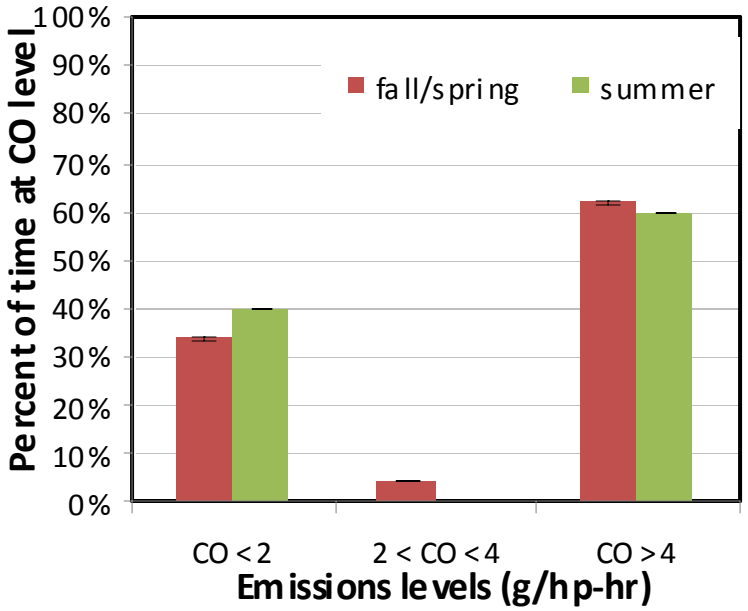

Figure 3.10 Seasonal effect on CO at Engine 3

The seasonal variations observed suggest that the correlations between emissions levels and ambient temperature should be examined. The influence of ambient temperature variation on the exhaust emissions for the three engines is presented in Figure 3.11 through Figure 3.13. These figures are constructed by binning the collected data with respect to ambient temperature and then calculating the average emissions for every 2^{o}F bin range. It can be shown from these figures that NO emissions have nearly the same trend in the three engines. NO emissions were observed to decrease with increasing ambient temperature, as shown in Figure 3.11 through Figure 3.13. This decrease can possibly be attributed to the fact that air density decreases with increasing ambient temperature, even though the controller should be able to compensate for the changing air density. Consequently, in warm weather the engine burns a richer mixture which leads to improve NO conversion efficiency. Following the same reasoning, CO emissions should show behavior opposite to that of NO emissions. Lower CO should be obtained in colder weather due to the lean operating condition caused by the higher air density at lower ambient temperatures. This trend of CO can be noticed only in Figure 3.12 for Engine 2. The other two engines did not show this trend clearly. Figure 3.11 and Figure 3.13 show that CO emissions just fluctuate and there is no evidence from this data that CO increases with higher ambient temperature based on the above explanation. This may be because NO conversion efficiency is more sensitive to the pre-catalyst oxygen concentration than the CO conversion efficiency, as observed in the mapping study. Thus, NO emissions are also more sensitive to ambient temperature than CO emissions. Another factor that might contribute to this fluctuation in CO and the NO trend is the influence of the EGO sensor itself with the ambient temperature. The change in the temperature of the sensor mounting assembly caused by the change in ambient temperatures could affect the sensor output. Because the trend in NO emissions was observed in all engines, and only Engine 1 was known to have leaner EGO set points during the winter months, these results suggest that the observed trend in NO emissions is not the result of only differences in EGO set points.

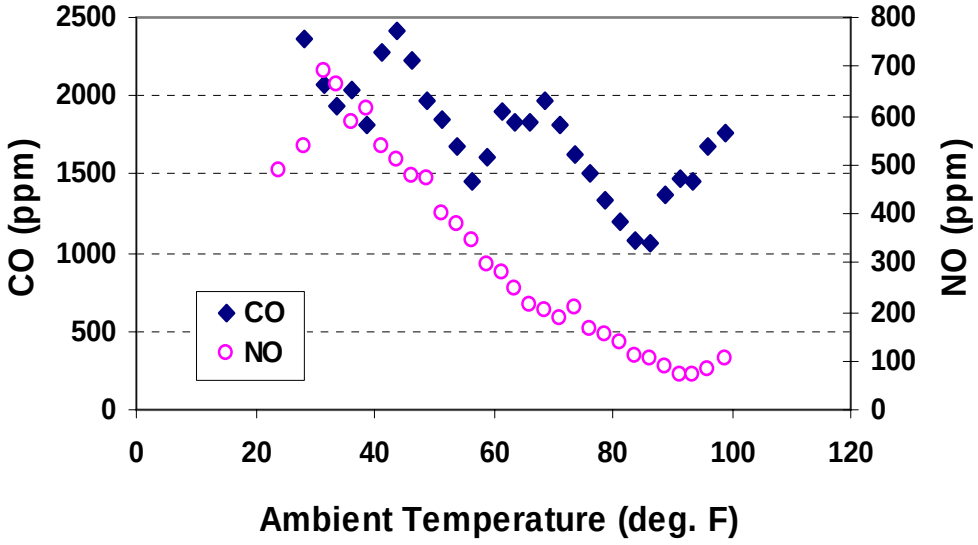

Figure 3.11 Effect of ambient temperature on emissions for Engine 1

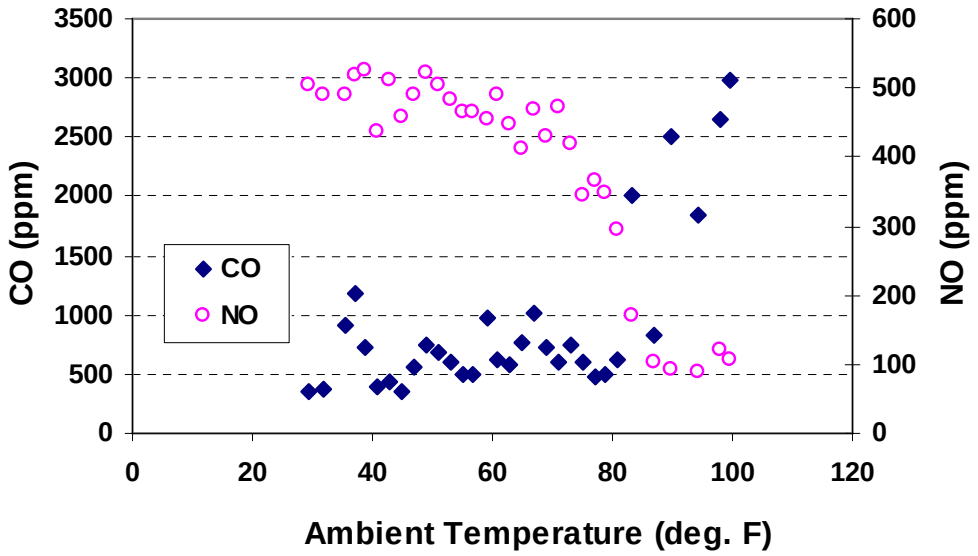

Figure 3.12 Effect of ambient temperature on emissions for Engine 2

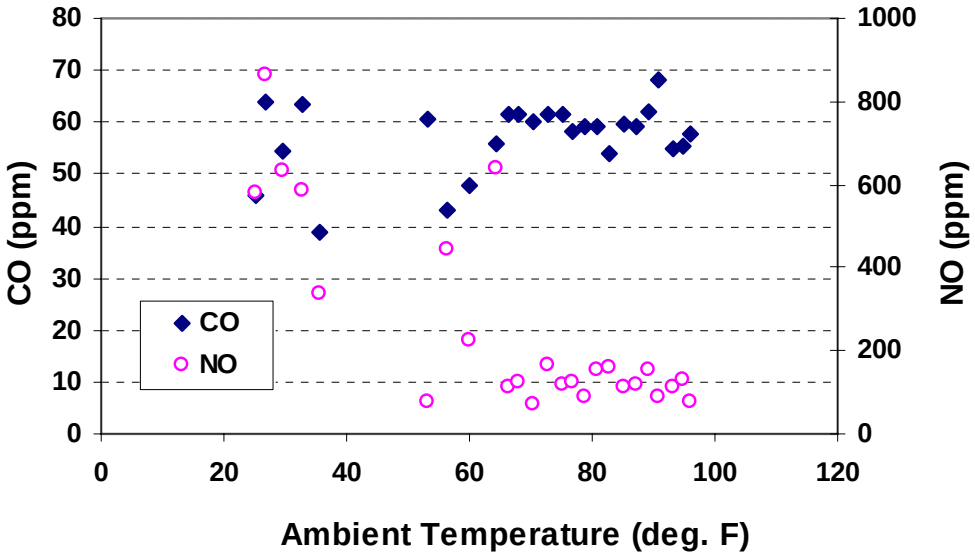

Figure 3.13 Effect of ambient temperature on emissions for Engine 3

Engine Mapping

A mapping study was conducted on one engine from June 10-12, 2008. This engine is rated at 57 hp in end user documentation and located in northern New Mexico at about 5,000 ft elevation, where it is used to compress natural gas at the wellhead. It was fitted with an Emit Technologies single round, foil, 8-inch catalyst with a 0.5-inch control valve and EDGE-NG AFRC. The engine, catalyst and EGO sensor had been rebuilt or replaced, respectively, approximately two months before the mapping study occurred.

Data Collection

During this study, the engine/NSCR system was operated at various controlled air-to-fuel ratios while a wide range of emission measurements were conducted and engine operating parameters monitored. The engine mapping task provided an opportunity to examine emissions at stable engine and emissions control system conditions compared to transient engine conditions. During the mapping procedure, data were collected with the engine in an as-found condition, as controlled by the AFRC. The AFRC set point was then varied over a range of richer and leaner conditions. The transitional changes in emissions were recorded, as were the

emission values once the engine was no longer transitioning from one point to another. Engine speed and approximate load were monitored but not intentionally adjusted.

The engine mapping procedure allowed the research team to collect extensive pre- and post-catalyst emissions data for each EGO set point of interest. For each test run, the research team first adjusted the EGO set point to a target value. The team then monitored the post-catalyst NO, CO, and O_2 emissions using both EPA reference method analyzers and the portable electrochemical analyzer normally used in long-term monitoring as shown in Figure 3.14. Next, the reference method O_2 analyzer was mechanically switched to the engine exhaust to measure the pre-catalyst oxygen concentration. Meanwhile, two extractive FTIR systems were used to measure pre- and post-catalyst formaldehyde, ammonia, and speciated hydrocarbons. Total hydrocarbons (THC) were also measured downstream of the catalyst using a flame ionization detector. The research team chose the EGO set points to evaluate the operating limits of the NSCR/AFRC system (i.e., the lean and rich limits) and to capture the transition of the exhaust emissions between the set points. Engine mapping was conducted over three days with a total number of 37 runs.

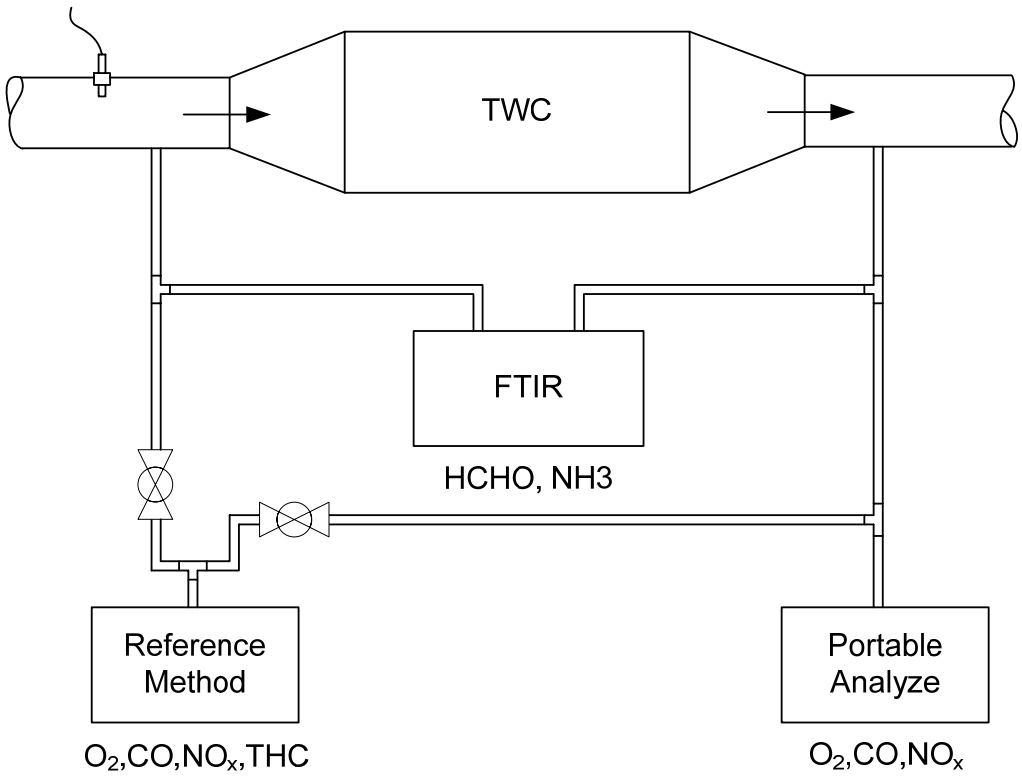

Figure 3.14 Schematic of various analyzers used in engine mapping.

Data Analysis

NO_x, CO, and Hydrocarbons

Figure 3.15 and Figure 3.16 present test results for oxygen and CO concentrations, respectively, when measured at the rich operating limit of the catalyst. For the purposes of this test, the rich limit was the richest EGO set point at which engine emissions remained relatively stable. As shown in Figure 3.15, the post-catalyst O_2 concentration was less than 0.1%. NO_x concentrations remained below 50 ppm at this operating condition. The data in Figure 3.16 show the NO_x /CO trade-off at the rich limit as CO concentrations ranged from 1,000 to 4,000 ppm while NO_x remained below 50 ppm. In general, emissions levels measured with the portable analyzer were comparable to those measured with the reference methods; although the reference methods show peak-smoothing relative to the portable analyzer, which is likely the result of a longer averaging time for the reference method data. In addition, the portable analyzer O_2 measurement appears to be slightly higher than the reference method measurement.

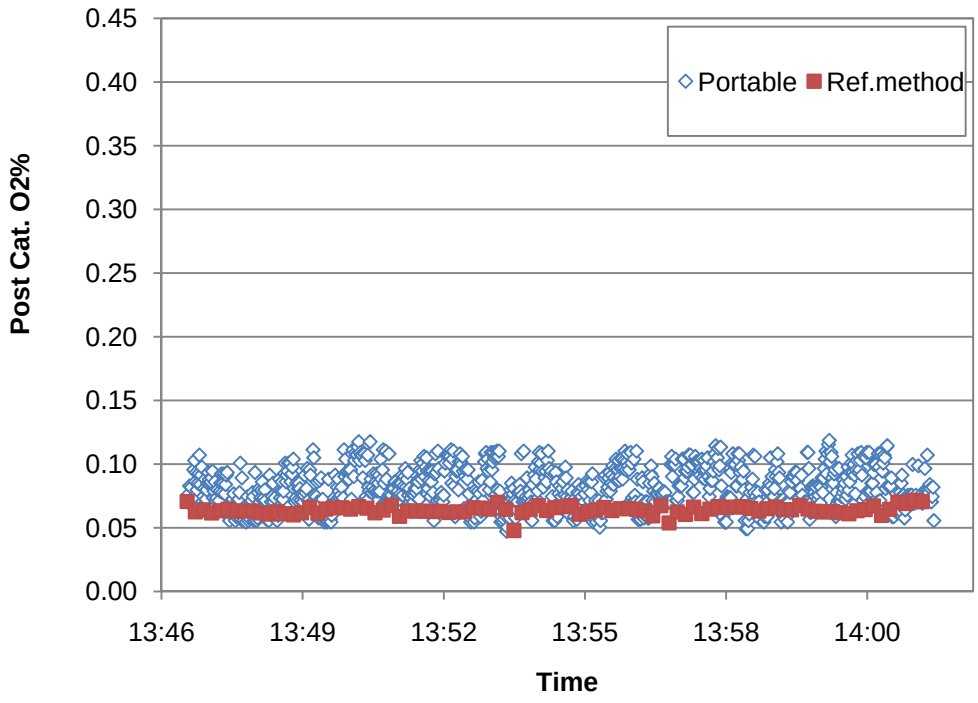

Figure 3.15 Post-catalyst O_2% at rich limit (June 12, 2008)

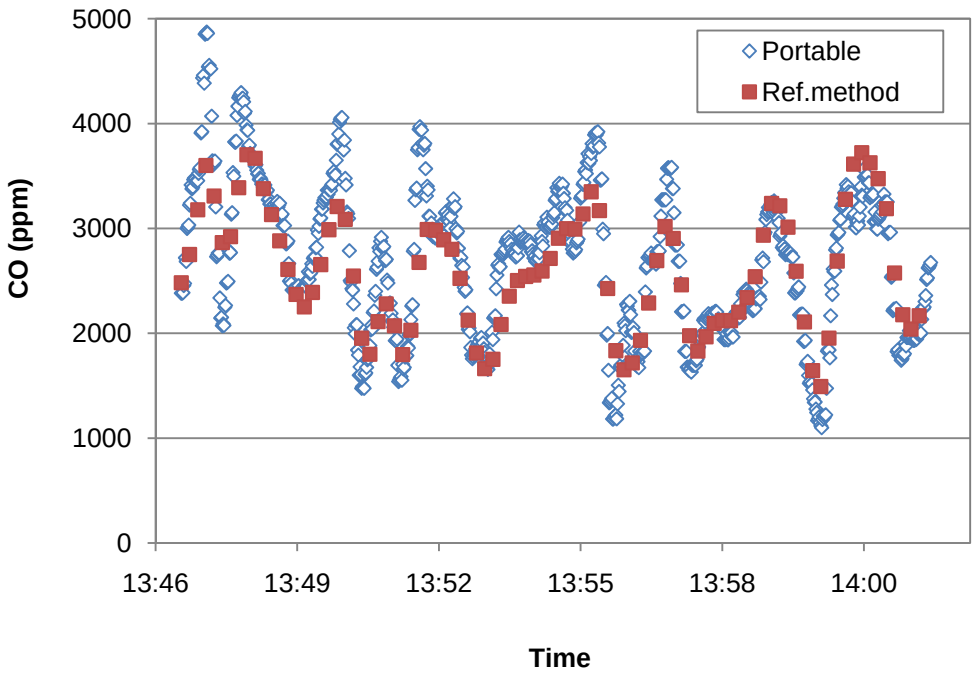

Figure 3.16 Post-catalyst CO at rich limit (June 12, 2008)

The fluctuations in the Figure 3.16 CO emissions data were likely caused, at least in part, by air-to-fuel ratio instability. Figure 3.17 presents the EGO sensor output during the rich limit test run. The sensor output fluctuations indicate changing net exhaust oxygen and a changing air-to-fuel ratio. The data suggest the AFRC was not able to tightly control the air-to-fuel ratio at this operating condition. The CO emissions fluctuation may have also been impacted by cyclic adsorption/desorption of exhaust gas species on the catalyst surface. The catalyst can periodically store and release oxygen, a process known as dithering, which affected the catalyst conversion efficiency and emission concentrations (Cottrill, 1999). Although the dithering process is normally expected when the air-to-fuel-ratio is intentionally periodically adjusted to allow the catalyst to store and release oxygen, this same process of oxygen storage and release occurs whenever the oxygen concentration in the exhaust stream varies over short periods of time. This variation could be caused by engine or AFRC controller instability.

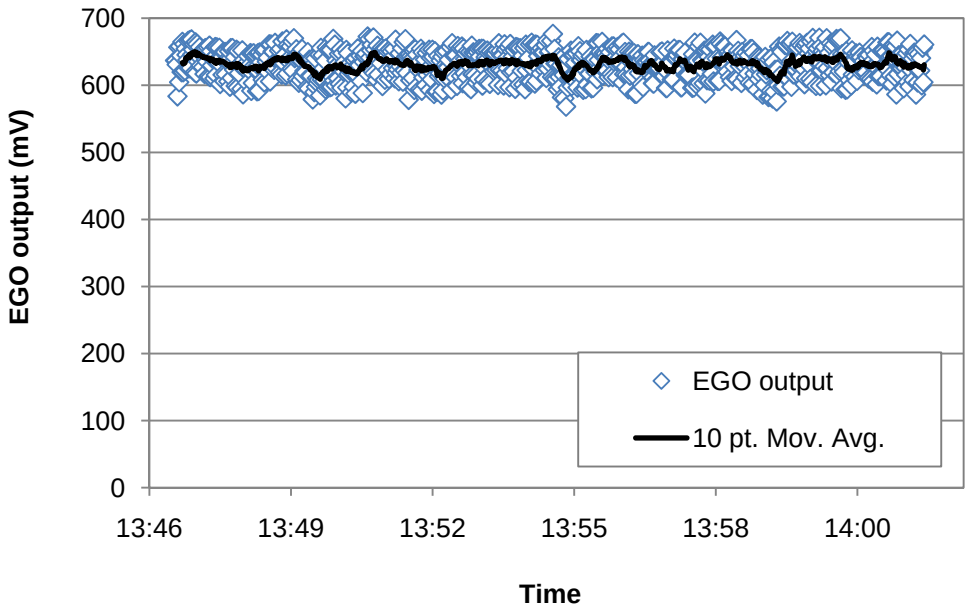

Figure 3.17 EGO output at rich limit (June 12, 2008)

Figure 3.18 and Figure 3.19 represent test results of oxygen and NO_x concentration with the engine operating at the catalyst lean limit. For the purposes of this study, the lean limit was the leanest EGO set point at which the emissions remained relatively stable. As shown in Figure 3.18, the post-catalyst O_2 concentration was greater than 0.25%. The CO concentrations remained well below 100 ppm at this operating condition. The data in Figure 3.19 show the NO_x /CO trade-off at the "lean limit" as NO_x concentrations ranged from about 1,000 to 2,000 ppm while CO remained less than 100 ppm.

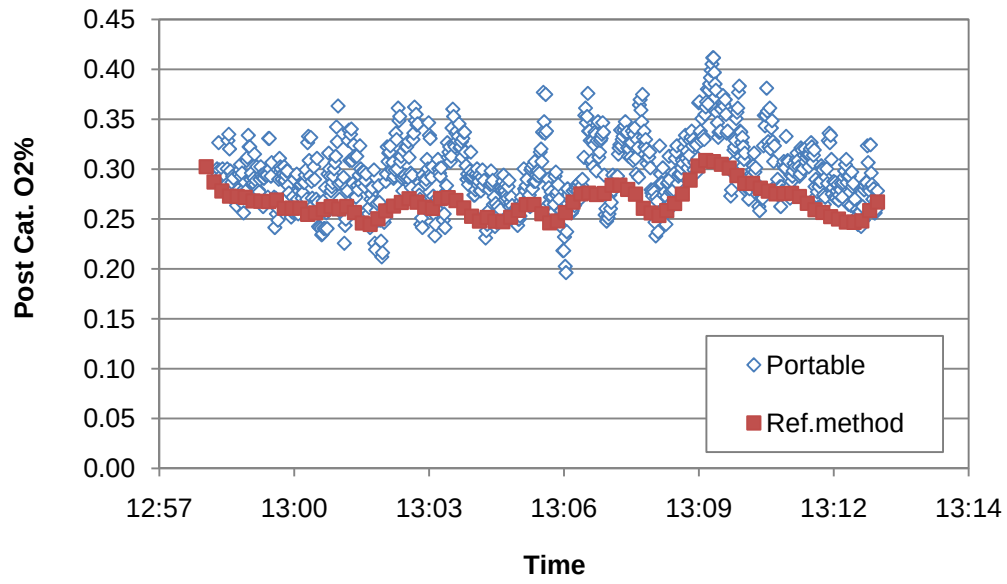

Figure 3.18 Post-catalyst O_2% at lean limit (June 10, 2008)

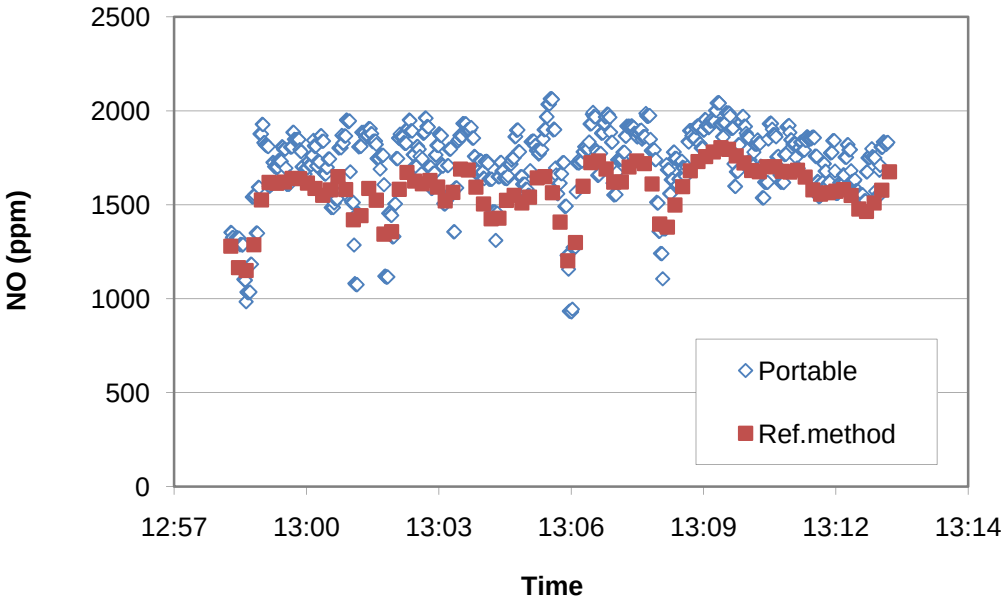

Figure 3.19 Post-catalyst NO at lean limit (June 10, 2008)

The mapping test results show that the catalyst emissions depend on the pre-catalyst oxygen concentration, which can be used as a surrogate for the engine air-to-fuel ratio. These pre-catalyst oxygen concentrations are measurements of O_2 molecules not "net oxygen" as measured by an EGO sensor. In the context of this study, both the concentration of O_2 molecules and the "net oxygen" are parameters of interest. Figure 3.20 shows the impact of a pre-catalyst

O_2 concentration ranging from approximately 0.4% to 0.53%. Although this range looks very small, it represents the typical operating range of a three-way catalyst, which is about 0.3% to 0.5%. The typical TWC operating range is slightly rich of stoichiometry, within an operating window of $\lambda = 0.99 \pm 0.005$ (Arney et al., 2007).

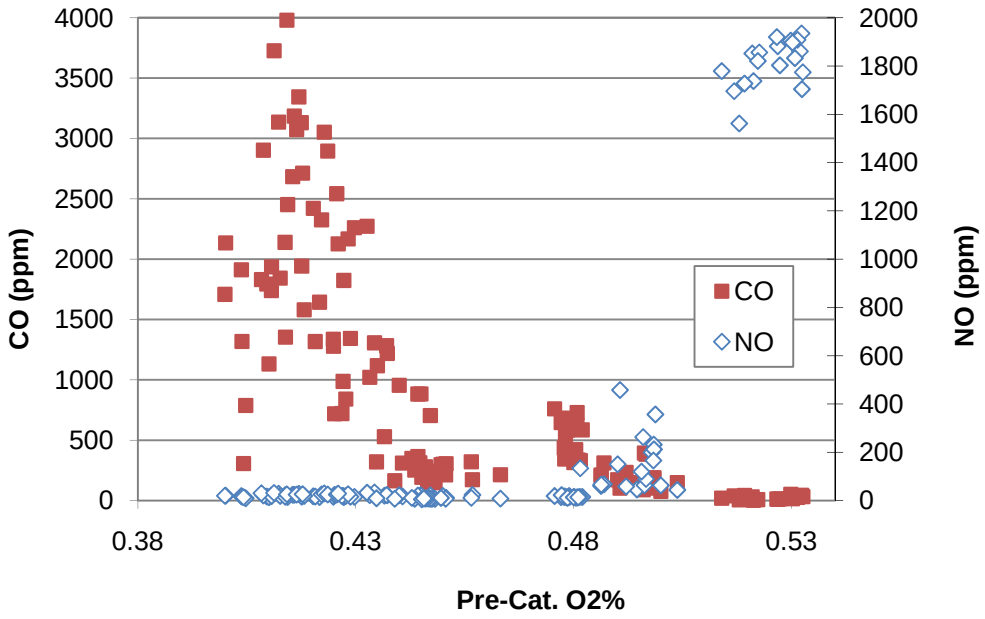

Figure 3.20 Influence of pre-catalyst O_2 % on CO and NO

The dependence of both CO and NO emissions on pre-catalyst O_2 concentration is depicted in Figure 3.20. As shown in this figure, a trade-off between CO and NO is observed. Increasing the concentration of pre-catalyst oxygen reduces CO emissions as O_2 molecules are available to oxidize CO to CO_2. However, this same increase in pre-catalyst oxygen concentration increases NO emissions because less CO and HCs are competing for the NO oxygen atom. This figure shows that an O_2 concentration of approximately 0.48% represents the boundary between rich and lean conditions. Figure 3.20 shows the catalyst's ability to maintain low NO emissions until the pre-catalyst oxygen concentration reaches 0.48%. However, at leaner conditions the data show a sharp increase in NO, implying decreased conversion efficiency. The optimum operating window for minimizing both CO and NO emissions appears to be between 0.45% and 0.48% pre-catalyst oxygen concentration for this particular NSCR/engine system.

Figure 3.21 shows the effect of pre-catalyst oxygen concentration on total hydrocarbon (THC) emissions. THC emissions decrease with higher oxygen, the same trend seen for CO, because the total hydrocarbon concentration also depends on oxidation reactions. Higher THC concentrations were obtained at lower oxygen concentrations due to insufficient oxygen to complete the oxidation of all hydrocarbons. However, the THC includes significant proportions of methane and ethane, which are not included in regulated VOCs. As the amount of oxygen available for combustion changes, the proportion of each hydrocarbon species may change as well. Therefore this pattern in THC cannot be used to draw conclusions about patterns for reduction of VOCs at this time. In this figure and the following figures, averages of the data sets for each run are used because the reference method could not be used to collect pre- and post-catalyst emissions simultaneously. As described earlier, the testing procedure was to first measure all post-catalyst emissions with the reference methods, including THCs, and then to measure the pre-catalyst oxygen concentration. Thus, the average pre-catalyst oxygen concentration is plotted against the average THC concentration collected immediately prior at the same operating condition. The error bars used in this figure represent the standard deviation of the data set. The large error bars are a consequence of the post-catalyst emissions fluctuations; for example, as shown previously in Figure 3.16 for CO.

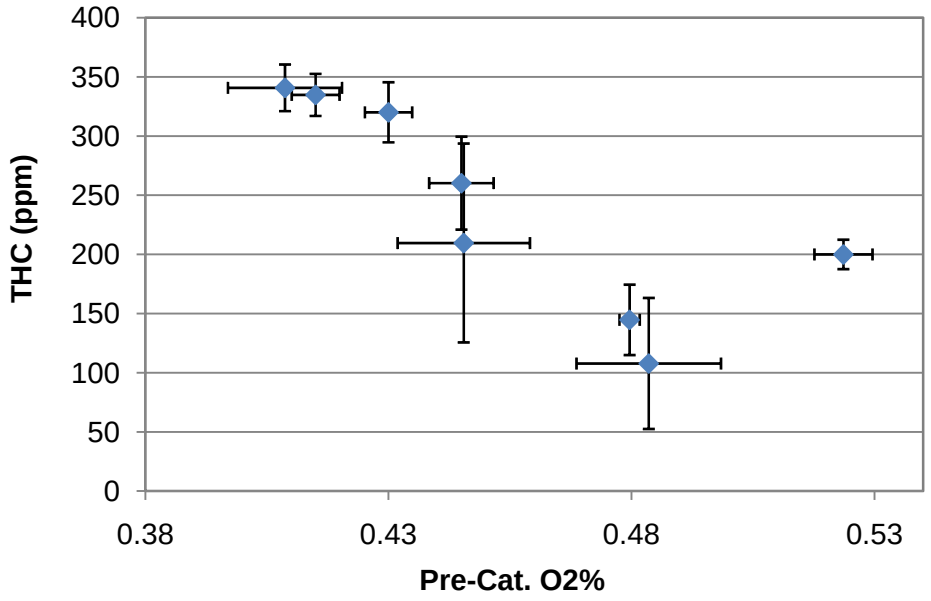

Figure 3.21 Influence of pre-catalyst O_2% on THC

Ammonia

During the mapping test, the ammonia emissions were quantified and correlated with other exhaust emissions, especially NO. EPA has identified ammonia as a precursor to fine particulate and thus a potential contributor to $PM_{2.5}$ NAAQS nonattainment and regional haze issues. It is not classified as a Hazardous Air Pollutant (HAP) under the EPA NESHAP program, but is considered an air toxic in some states, and is often regulated. For example, large utility boilers or turbines that use selective catalytic reduction will typically have an ammonia emission limit (i.e., "ammonia slip" limit) of 10 ppmv or lower. Ammonia concentration was measured using the FTIR technique before and after the catalyst.

Figure 3.22 shows the relationship between post-catalyst ammonia concentration and pre-catalyst oxygen concentration. Lower pre-catalyst oxygen corresponded to higher post-catalyst ammonia concentrations. At all operating conditions, the pre-catalyst ammonia concentration, typically below 2 ppm, was lower than the post-catalyst ammonia concentration. These data indicate that ammonia is a secondary pollutant that is formed inside the catalyst rather than during the combustion process in the engine.

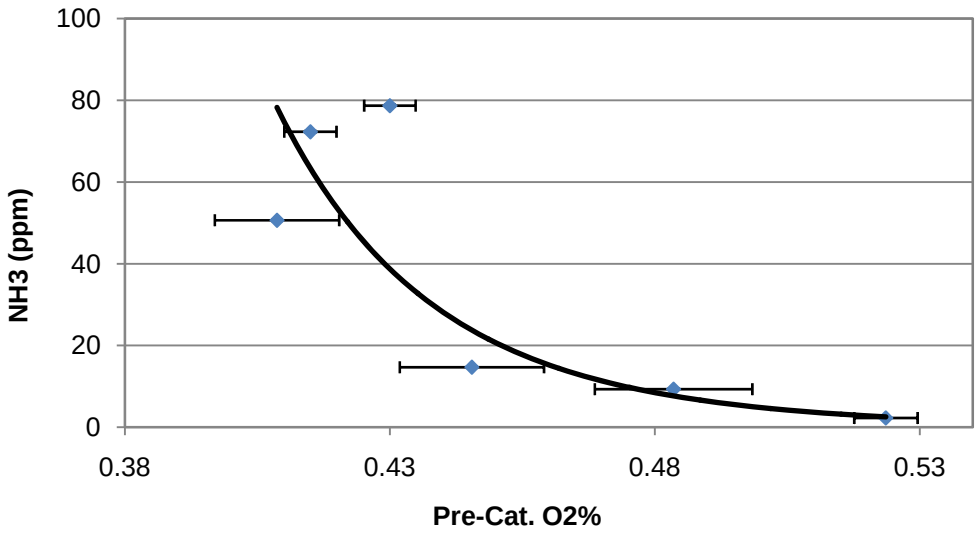

Figure 3.22 Influence of pre-catalyst O_2% on ammonia.

The inverse relationship between oxygen concentration and ammonia formation shown in Figure 3.22 suggests a trade-off between ammonia and NO emissions for an engine equipped with NSCR. NO and H_2 are considered the precursor molecules for ammonia formation in the

catalyst (Heeb et al., 2006). Because both molecules are produced during rich combustion with an oxygen-deficient or low-oxygen mixture, the ammonia formation reactions occur as:

$$2NO + 5CO + 3H_2O \rightarrow 2NH_3 + 5CO_2 \quad \textbf{(3-1)}$$

$$2NO + 5H_2 \rightarrow 2NH_3 + 2H_2O \quad \textbf{(3-2)}$$

The relationship between ammonia concentration and NO concentration is shown in Figure 3.23. This figure shows the trade-off between NO and ammonia on a logarithmic scale. Operating the catalyst under rich reducing conditions increases NO conversion, but forces the formation and subsequent release of ammonia. At the other end of the rich-lean spectrum, no ammonia is formed under lean oxidizing conditions, but NO emissions increase.

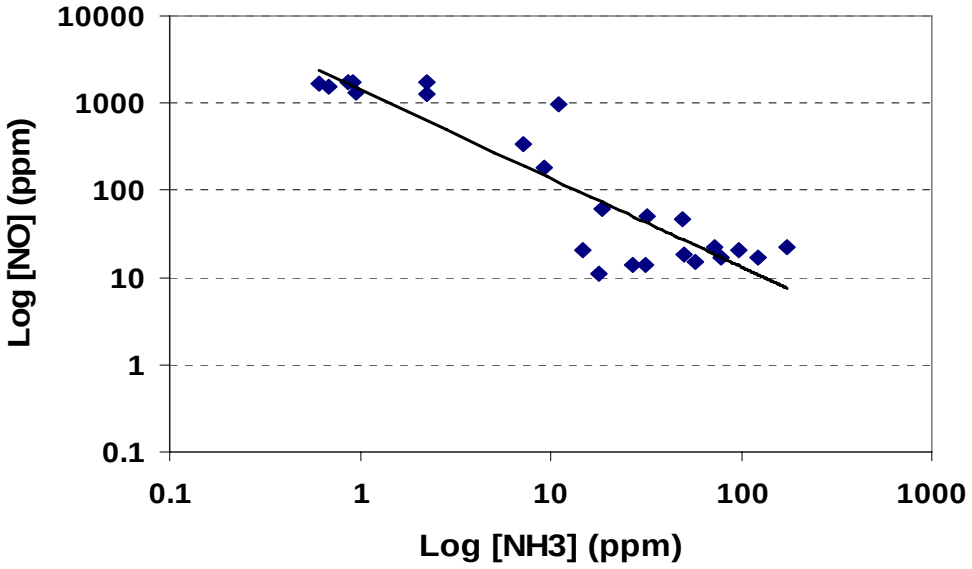

Figure 3.23 The trade-off between ammonia and NO

Formaldehyde

Formaldehyde is one of the HAPs emitted from natural gas engines. Formaldehyde is a carcinogenic aldehyde that is regulated for some engines under the NESHAP. Unlike ammonia, which is a secondary pollutant, formaldehyde is formed in the engine cylinder as a result of the partial oxidation of hydrocarbons that takes place near the cylinder wall and engine crevices, and

formaldehyde is an intermediate product in the combustion of methane, the primary constituent in natural gas.

The engine mapping results showed formaldehyde pre-catalyst emissions ranging from 15 to 33 ppm and post-catalyst emissions ranging from below the detection limit of 0.2 ppm to about 0.6 ppm. Figure 3.24 shows the formaldehyde concentration before and after the catalyst with the pre-catalyst oxygen percentage. This figure illustrates the ability of the catalyst to almost completely oxidize formaldehyde.

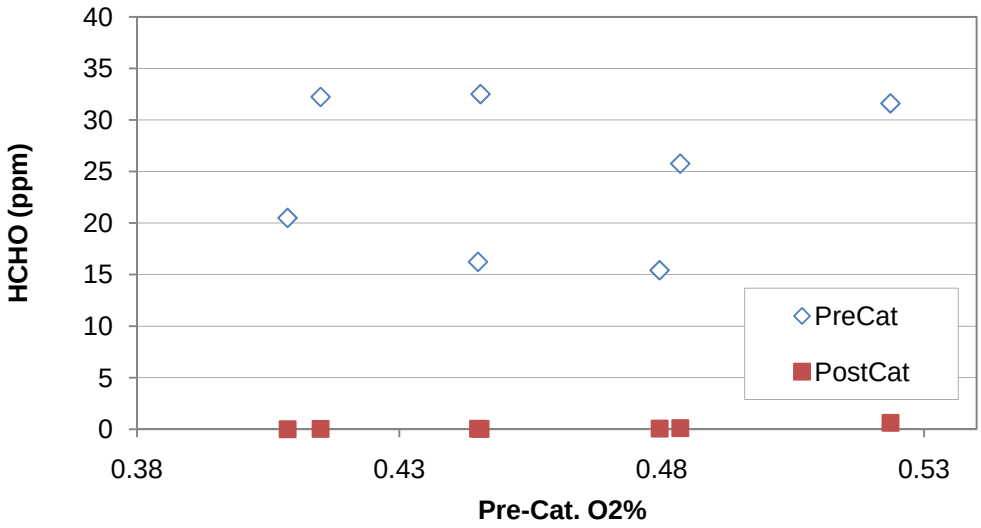

Figure 3.24 Pre- and post-catalyst formaldehyde emission

EGO Sensor

Figure 3.25 shows the data collected from the EGO sensor during the engine mapping. This figure shows the influence of the pre-catalyst oxygen percentage on the sensor output. The numbers included in this figure refer to the test number. The tests depicted in this figure are the only tests were the EPA reference method analyzer was switched to the pre-catalyst side to measure oxygen concentration. The rest of the other 37 tests were used for post-catalyst measurements or transient tests when the engine was tuned from one operating point to another.

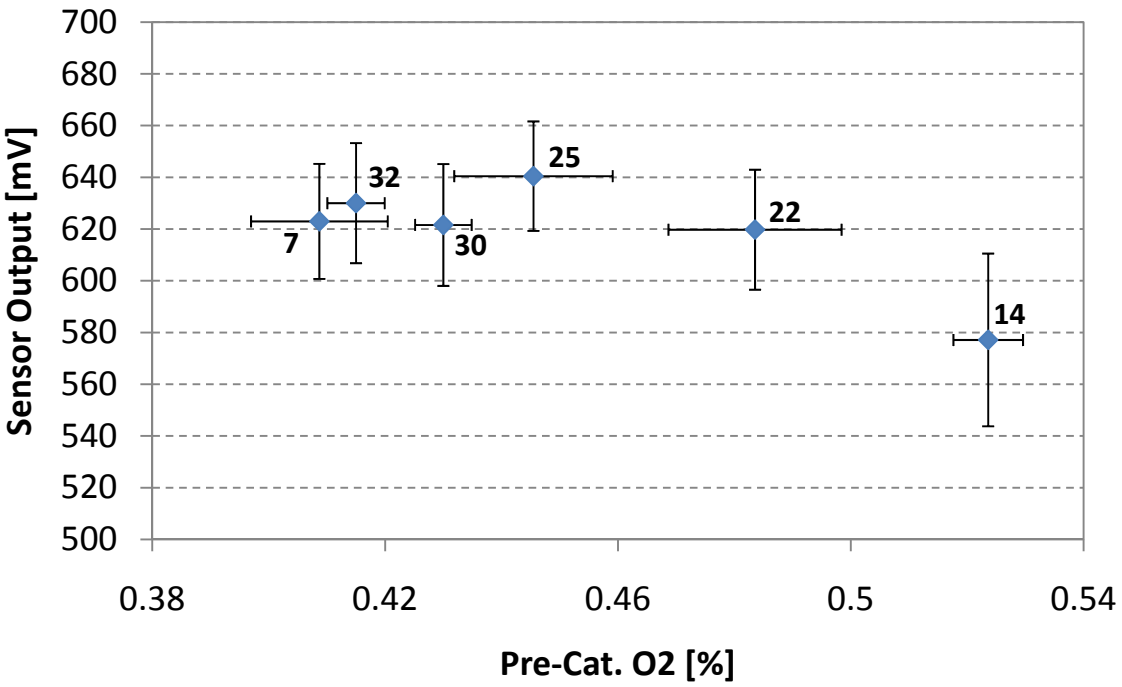

Figure 3.25 The sensor output from engine mapping study

The error bars included in Figure 3.25 represent the standard deviation of the collected data, because the points shown here are the average of 5 minutes of data collection during each test. Figure 3.25 shows that there is an overall inverse correlation between the sensor output and the exhaust oxygen concentration. However, the data showed that some points have the same sensor output even with different oxygen concentrations. Also, there is an unexpected decrease in the sensor voltage for Test 7 and Test 32, although the engine was operated at lower pre-catalyst oxygen percentage during Test 7 and Test 37. This kind of inconsistency and unexpected results needs to be interpreted and analyzed correctly by using the current developed model.

Table 3-6 shows the details of the exhaust gas species for each of the engine mapping tests. This table also presents the pre-catalyst exhaust temperature and pressure as well as the lambda sensor output. This data was measured using an FTIR analyzer, except the oxygen concentration was measured using an EPA reference method analyzer. Hydrogen concentrations are assumed to equal one third of the CO concentration. Most of the previous work agreed that there is a strong correlation between CO and H_2. Hydrogen concentration is approximately one third of the CO measurement.

Table 3-6 Details of the engine mapping results

	Test 7	Test 14	Test 22	Test 25	Test 30	Test 32
O_2 [%]	0.4087	0.5236	0.4835	0.4455	0.4300	0.4150
H_2O [%]	13.12	12.94	19.20	21.48	18.30	16.03
CO_2 [%]	10.39	10.39	9.67	9.29	9.79	10.01
CO [ppm]	4453.89	3306.97	3972.66	4811.96	4369.23	4663.02
NO [ppm]	1686.31	1722.27	1551.10	1501.67	1728.53	1737.43
H_2 [ppm]	1484.63	1102.32	1324.22	1603.99	1456.41	1554.34
CH_4 [ppm]	901.10	808.91	766.54	781.96	818.49	852.47
N_2 [%]	75.22	75.45	69.88	67.91	70.64	72.66
P [Pa]	94368.37	93608.40	95473.90	94836.69	91908.57	94089.10
T [K]	845.41	838.69	826.10	829.97	825.32	820.75
Sensor Output [mV]	622.97	577.14	619.76	640.45	621.58	630.02

Figure 3.26 and Figure 3.27 are a graphical representation of the data shown in Table 3-6. In these two figures, emissions are plotted as functions of the pre-catalyst oxygen percentage. Figure 3.26 presents the CO_2 and H_2O concentrations in volume percentage, while Figure 3.27 shows the emissions concentration in ppm. Generally, these two figures illustrate that the functional variation of all species with O2 except H_2O and CO, is almost zero.

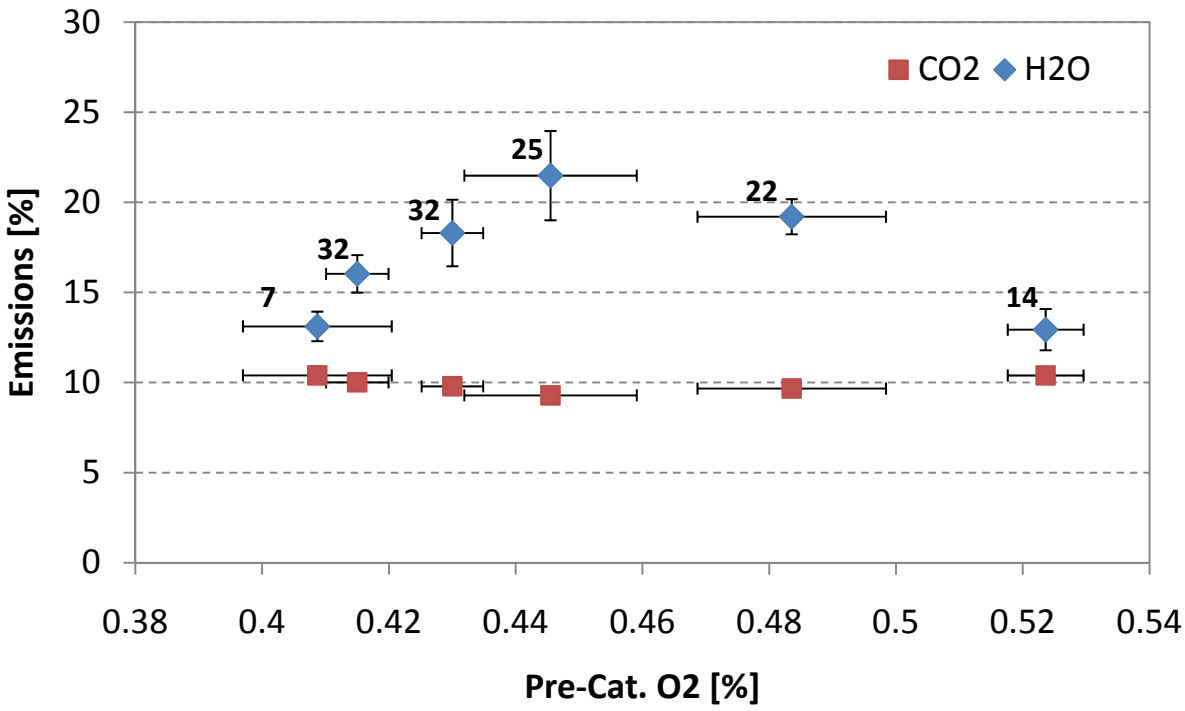

Figure 3.26 CO_2 and H_2O emissions

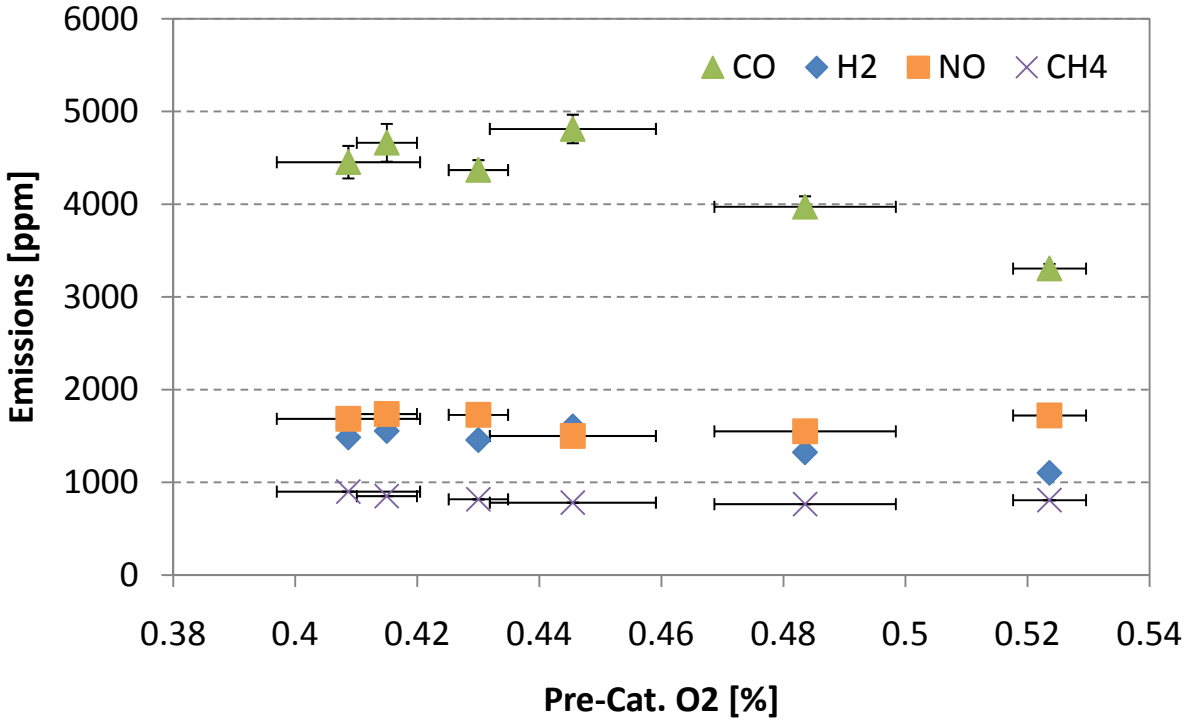

Figure 3.27 CO, H_2, NO, and CH_4 emissions

The mapping data indicate that the oxygen concentration ranging from approximately 0.4% to 0.52%. This range of 0.12% change of oxygen is considered very small. This mapping was intentionally done to fine tune the NSCR system. Thus, the research team adjusted the air-to-fuel ratio just in the range of very low emissions. Once, the emissions reach higher levels they re-adjust the air-to-fuel ratio back to achieve lower concentration. In fact, this allows only a very small range of air-to-fuel ratio which is almost around the narrow catalytic window of the NSCR system. Unfortunately, this mapping was not conducted for the purpose of providing a wide range of operation to validate the model.

In order to estimate the range of operation of the mapping data, lambda was calculated using the mole fraction of each exhaust gas constituents (Mario Balenvic, 2002):

$$\lambda = \frac{2x_{CO_2} + x_{CO} + 2x_{O_2} + x_{NO} + x_{H_2O}}{2x_{CO_2} + 2x_{CO} + x_{H_2} + \left(2\alpha + \frac{\beta}{2}\right)x_{C_\alpha H_\beta} + x_{H_2O}} \quad \textbf{(3-3)}$$

This equation is a result of solving a system of equations that describe the mass balance of each individual atom included in the combustion process and the equilibrium constant equations. The analysis reveals that the lambda operating range is also very narrow. Figure 3.28 illustrates the same mapping data with the lambda in the horizontal axis. As shown from this figure, lambda is ranges between 0.995 and 1.007. This calculation indicates that the operating range of this mapping test is only 0.012.

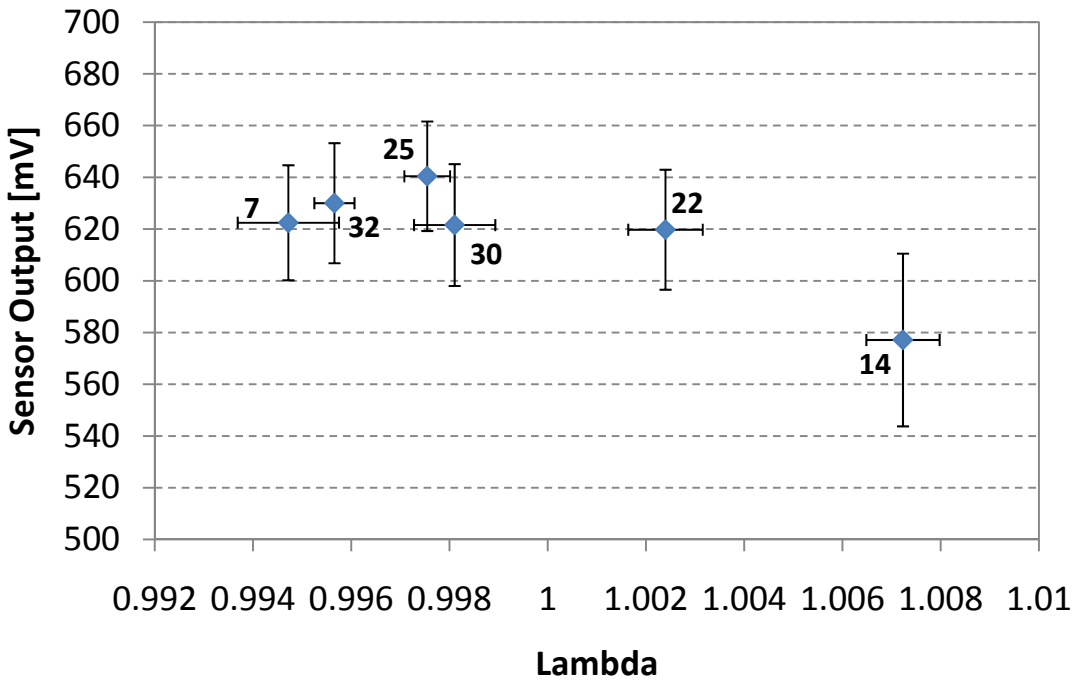

Figure 3.28 The sensor output versus lambda

The air-to-fuel ratio calculation shows that there is a correlation between oxygen concentration and lambda. This correlation is illustrated in Figure 3.29. Four of the six points are correlated very well with lambda while the other two points (i.e., Test 25 and Test 30) do not have this strong correlation. However, Test 30 has a lower oxygen concentration than Test 25, whereas the calculated lambda of Test 30 is greater than that of Test 25. This deviation might be caused by the uncertainty in the emissions measurements during these two specific tests. The difference in oxygen concentration is very small compared to the fluctuations in the emission measurements and this may cause the shift between these two points.

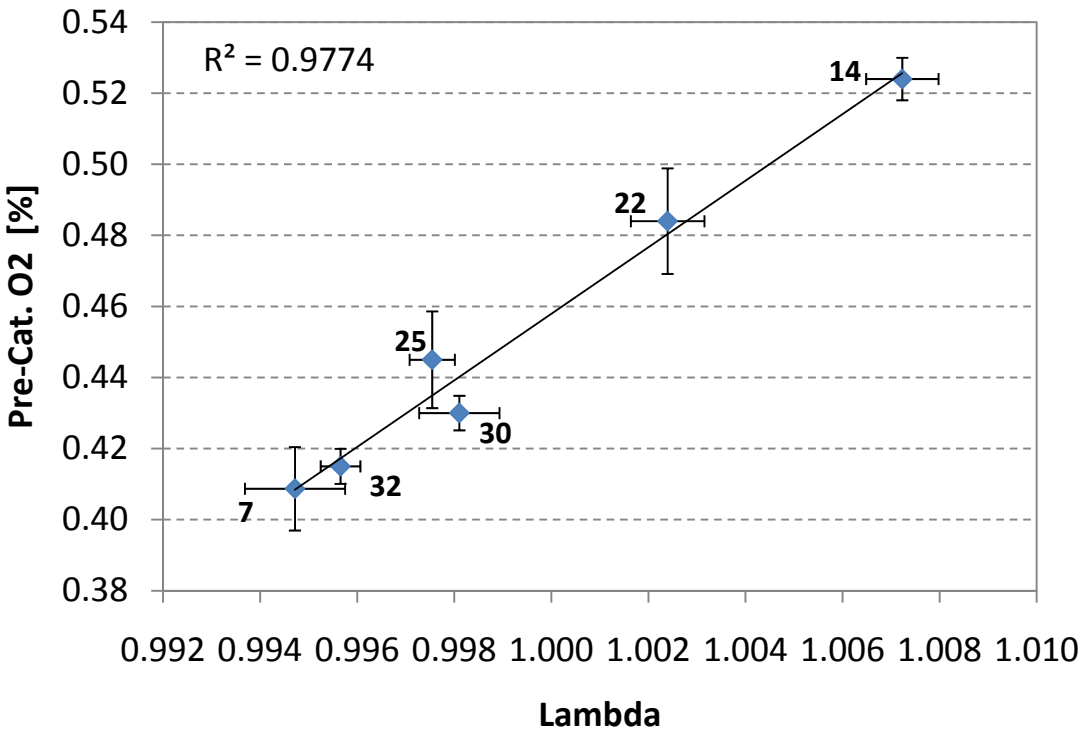

Figure 3.29 The correlation between lambda and oxygen concentration

The exhaust gases concentration were redrawn again versus lambda as shown in Figure 3.30 and Figure 3.31. The overall trend is the same as presented before with oxygen concentration, except the shift that occurred between test numbers 25 and 30.

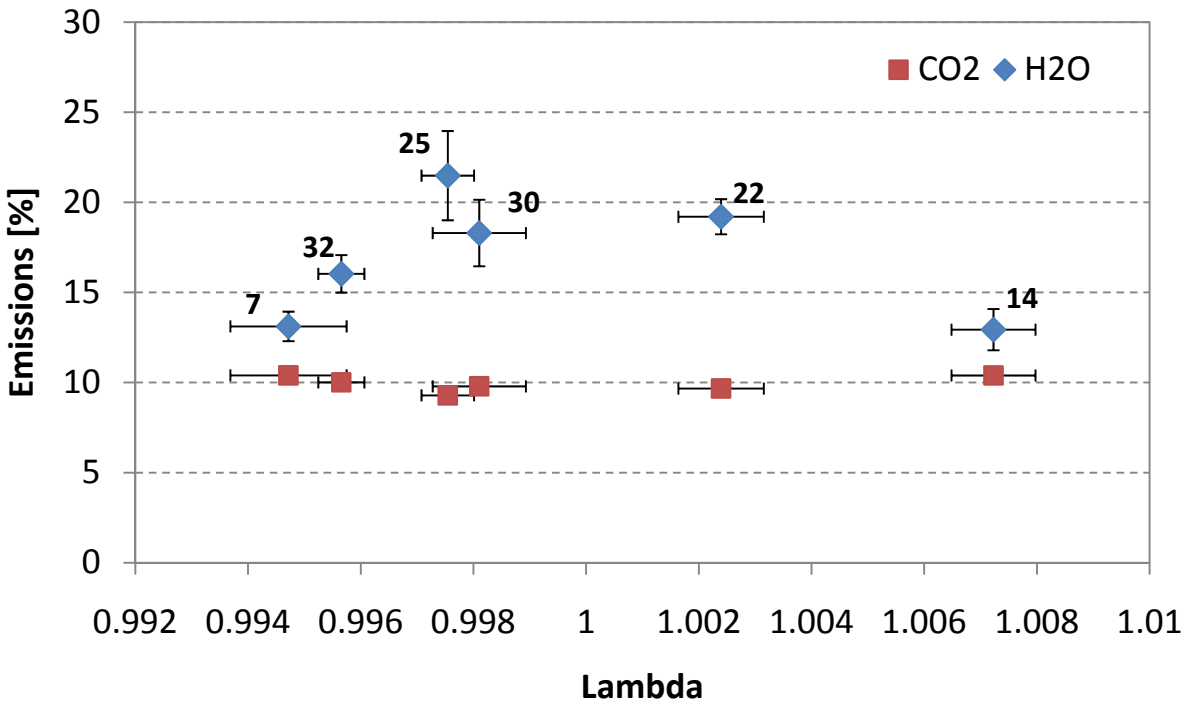

Figure 3.30 CO_2 and H_2O versus lambda

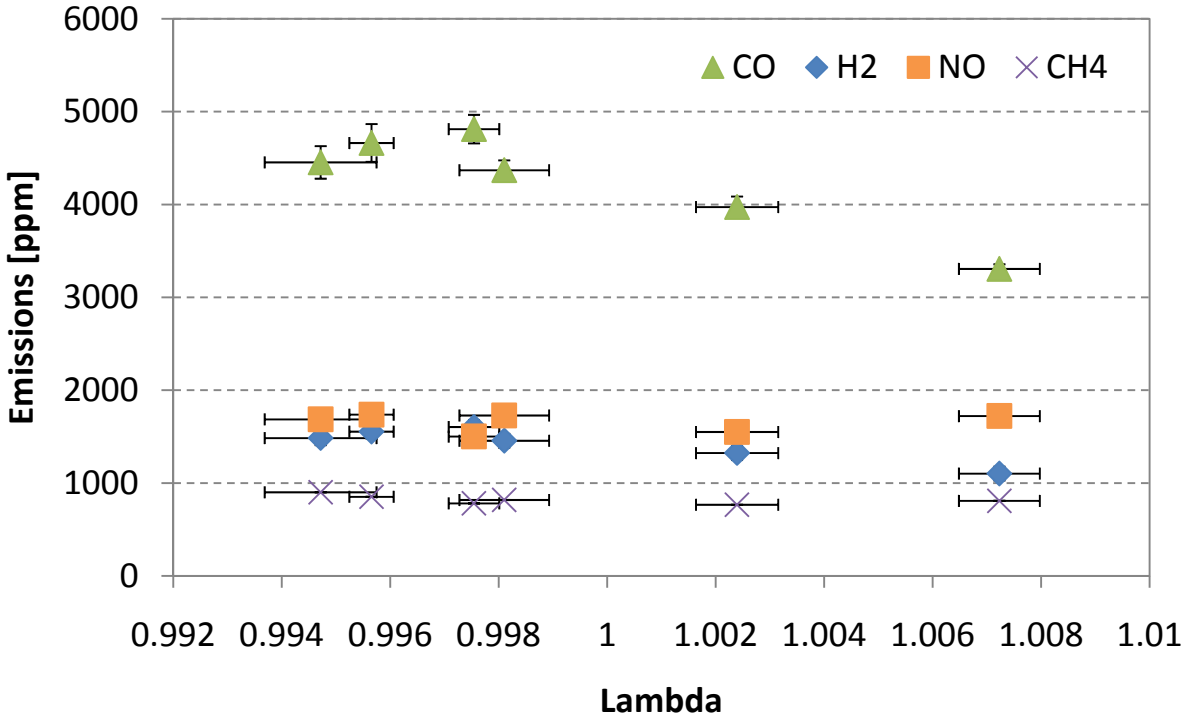

Figure 3.31 Emissions versus lambda

Conclusions from NSCR Field Testing

This long term study examined the reliable capabilities of currently-available NSCR/AFRC solutions for small field gas-fired engines employed in gas gathering. The extensive set of data collected during the NSCR field testing shows that currently-available NSCR/AFRC systems were capable of intermittently controlling NO_x and CO emissions. Emissions were not consistent from day-to-day, or even over a few hours. At times, volumetric emissions concentrations varied significantly within a short time period and caused either levels of one or both emissions species to increase or decrease. For the majority of the operation, one species was more effectively controlled than the other. While the data indicated that a tight operating window exists to simultaneously control NO_x to below 0.5 g/hp-hr and CO to below 2 g/hp-hr, the AFRC was not able to consistently control to this tight operating window. The data show the seasonal impact on the emissions variations. It is shown that NO_x is more sensitive than CO to ambient temperature variation. NO_x emissions experienced higher conversion efficiencies during higher ambient temperatures.

These results extend the applicability of those tests conducted in California in 2007 (Arney). While the 2007 study was unable to show simultaneous effective control of NO_x and CO at California BACT limits of 0.15 g/bhp-hr NO_x and 0.6 g/bhp-hr CO over the course of a few weeks, the current work shows similar difficulties at less stringent targeted emissions levels and over several climatic seasons. The "Four Corners" work eliminates the possibilities left open by the California study that difficulties in simultaneous control of NO_x and CO occur only at extremely stringent emissions levels, are the result of insufficient time to allow the engine/NSCR system to stabilize, or are limited to specific seasonal/climactic conditions.

The author acknowledges that while consistent emissions control has not been observed during this project, this does not mean all NSCR systems (from all vendors for all applications) cannot consistently control CO and NO_x emissions. This thesis only comments on the difficulties encountered during this project for the NSCR application to natural gas production compressor engines. For example, if fuel variability plays an important role, this may be less of an issue with pipeline quality gas.

Although it has been possible to collect a large amount of semi-continuous data throughout this study, technical difficulties with using a portable analyzer for an application other than that for which it was designed have resulted in a significant number of days when the

engine emissions could not be monitored. To mitigate these problems, multiple maintenance steps were required on the data acquisition and communication systems. Monthly or bi-monthly analyzer calibrations were conducted for this project and generally provided confidence in the data. However, when over-concentration operation was encountered during the intervening time, more frequent calibrations would have be desirable to increase confidence in collected data. While a portable analyzer operating in semi-continuous measurement mode performed reasonably well for this field evaluation, such a system may not be comparable to a Continuous Emissions Monitoring System (CEMS).

One of the key outcomes of this study is the two very extensive data sets: the semi-continuous data set that includes over 200,000 minutes of data and the complete engine mapping data set. The semi-continuous data set includes very broad ambient and operational data that can now be used to improve/understand NSCR performance and the ability of the AFRC to optimally control that performance. This data can be used to design improved control systems that can plausibly extend the effective operating range of NSCR systems to the sub-1 g/bhp-hr range for NO_x and sub-2 g/bhp-hr range for CO without other deleterious effects.

The data also clearly indicate that there are unaccounted for degrees of freedom in existing NSCR systems, such as ambient temperature, ambient pressure, and the impact of ammonia and methane on the signal that is produced by the EGO.

Due to the inconsistency of EGO sensor output and its impact on the overall NSCR/AFRC systems capabilities, the research team believes a focused effort on modeling and interpreting the EGO sensor output is absolutely necessary. The rest of this thesis will focus on developing physics-based computer model of the EGO sensor. This model can be used to interpret the EGO output signal correctly and consistently achieve low NO_x and CO emissions.

Chapter 4 - Mathematical Model

The methodology used in this study focused on modeling the widely used, planar switch type lambda sensor shown in Figure 4.1. The planar type lambda sensor is composed of several active layers stacked together. The planar design enhances the use of an integrated strip heater element, improving the dynamic characteristics of the sensor. This work is considered an extension of Auckenthaler's study (2002), using the same approach, but for natural gas exhaust.

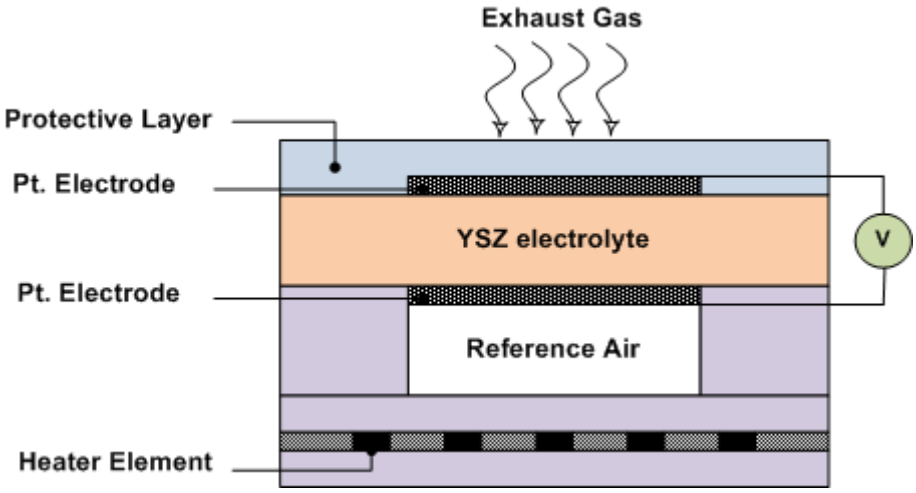

Figure 4.1 Schematic of planar switch-type sensor

Modeling Overview

The general overview of the modeling process is presented in Figure 4.2 where the EGO sensor model is divided into three main modules. The input parameters to the model are basically the exhaust gas compositions. The research team focused on the exhaust gases from natural gas fueled engines to examine the effect of methane on the electrode reaction and hence on the sensor output. Another input parameter is the exhaust temperature which is assumed to be in the actual experimental exhaust gas range.

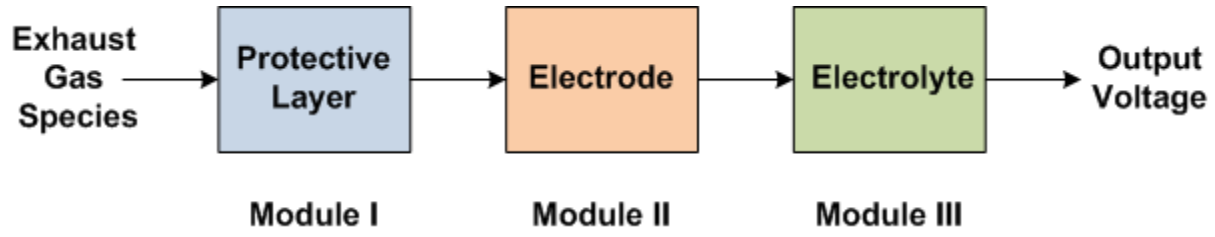

Figure 4.2 Schematic of EGO sensor modeling approach

The modules divide the sensor into three parts. The first is the simulation of the protective diffusion layer, the second part encompassed the platinum electrodes, and the third part describes the solid electrolyte material. The output from the EGO sensor is the voltage difference that is developed between the two electrodes. This output voltage is proportional to the difference in equilibrium oxygen concentration across the two electrodes, as well as on the gas constituents that indirectly affect the oxygen consumption or release in the electrode.

Module I: Simulation of Protective Layer

Mass transfer of various exhaust species through the protective layer are modeled using this module. The transport of these species is purely diffusive. The exhaust gas mixture is composed of CO_2, H_2O, N_2, O_2, CO, H_2, NO, and CH_4. The input to this module is the exhaust gas mole fraction $x_i^{exhaust}$ of each species, and the output is the gas mole fraction at the electrode $x_i^{electrode}$. There is also interaction between this module and the Pt. electrode module due to the desorption process that occurs at the platinum electrode.

Module II: Simulation of Pt-Electrode

This module is responsible for calculating the occupancies of the adsorbed species on the platinum electrode surface by knowing the gas concentration of each constituent from the protective layer module. All the reactions were modeled according to Langmuir-Hinshelwood kinetics, which is the method used by Auckenthaler (2005), although the use of natural gas exhaust requires the addition of more reactions including methane catalytic reactions.

Module III: Simulation of Electrolyte

In this module, the actual sensor output voltage is calculated. By applying the Nernst equation, the generated potential difference across the electrodes is correlated to the oxygen concentrations. The literature review revealed that there are many approaches that can be followed to simulate the YSZ electrolyte. The simplest approach considers the oxygen concentration on the electrode and the transition of oxygen between the electrode and the electrolyte based on the concentration gradient only. A second approach takes into account the direct reactions of reducing species on the electrode, and thereby introduces a driving force of oxygen transition which is the chemical potential of the redox reactions that occur on the electrode. Yet another approach is based on incorporating the adsorption of various species on the electrolyte itself. According to Auckenthaler (2005), the second approach provides an excellent accuracy compared to the other two methods and hence this work focuses only on the second approach.

Protective Layer Modeling

The protective layer is the uppermost part of the lambda sensor, and is composed of highly porous ceramic material. The function of this layer is to protect the outer platinum electrode from the direct exposure to exhaust gases to avoid gas contamination in addition to electrode erosion. The main process that occurs through this protective layer is a diffusive mass transfer of the various exhaust gas species.

Figure 4.3 shows the input/output of the protective layer module. The input parameters of this module are the exhaust gas temperature, pressure, and the mole fractions of all exhaust gas constituents. The output parameters are the mole fraction at the interface between the protective layer and the sensor outer electrode.

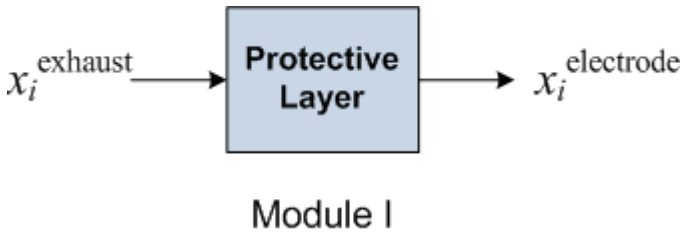

Figure 4.3 The protective layer module

The diffusion of the exhaust gas species through the protective layer is modeled using mass conservation law (Equation (2-27)). This model assumes one-dimensional steady diffusive mass transfer within the protective layer. For the one-dimensional steady model, the mass conservation equation is simplified as:

$$\frac{\partial J_i}{\partial z} = 0 \tag{4-1}$$

where z is the one-dimensional coordinate. Therefore, the diffusive fluxes are constant throughout the protective layer. This model assumes uniform temperature and concentration profiles across the sensor cross sectional area. In this module, the diffusive mass fluxes in the above mass conservation equation are calculated using the Maxwell-Stefan equation (Equation ((2-22)).

Throughout this thesis, there will be two sets of equations. The first set describes the model without counting methane in the exhaust gas species. This set of equations is used to validate the current developed model with the data available from the literature. These data were generated from gasoline engine studies without integrating methane into their model because methane exhausted from gasoline engines is substantially negligible. The author believes that in order to develop a new model including methane, it is valuable to start by assessing the reliability of this model with available literature data. Therefore, there will be two sets of equations when describing any part of the model. The first one does not include methane while the second one includes methane.

Table 4-1 presents the list and numbering system of the different exhaust gas species used in the model. Table 4-2 shows the set of equations used to validate the model without including methane. In this set of equations, there are seven exhaust gas species, while in Table 4-3 all eight species are used including methane.

Table 4-1 Numbering of exhaust gas species

Index	1	2	3	4	5	6	7	8
Species	N_2	CO_2	H_2O	O_2	CO	H_2	NO	CH_4

Table 4-2 Protective layer diffusion equations (without methane)

Species	Equation $(\boldsymbol{J_i}) = -\boldsymbol{C_t}\,[\boldsymbol{B}]^{-1}(\boldsymbol{\nabla x_i})$	Eq.#
N_2	$J_{N_2} = A_{11}\left(x_{N_2}^{elec} - x_{N_2}^{exh}\right) + A_{12}\left(x_{CO_2}^{elec} - x_{CO_2}^{exh}\right) + A_{13}\left(x_{H_2O}^{elec} - x_{H_2O}^{exh}\right) + A_{14}\left(x_{O_2}^{elec} - x_{O_2}^{exh}\right) + A_{15}\left(x_{CO}^{elec} - x_{CO}^{exh}\right) + A_{16}\left(x_{H_2}^{elec} - x_{H_2}^{exh}\right)$	**(4-2)**
CO_2	$J_{CO_2} = A_{21}\left(x_{N_2}^{elec} - x_{N_2}^{exh}\right) + A_{22}\left(x_{CO_2}^{elec} - x_{CO_2}^{exh}\right) + A_{23}\left(x_{H_2O}^{elec} - x_{H_2O}^{exh}\right) + A_{24}\left(x_{O_2}^{elec} - x_{O_2}^{exh}\right) + A_{25}\left(x_{CO}^{elec} - x_{CO}^{exh}\right) + A_{26}\left(x_{H_2}^{elec} - x_{H_2}^{exh}\right)$	**(4-3)**
H_2O	$J_{H_2O} = A_{31}\left(x_{N_2}^{elec} - x_{N_2}^{exh}\right) + A_{32}\left(x_{CO_2}^{elec} - x_{CO_2}^{exh}\right) + A_{33}\left(x_{H_2O}^{elec} - x_{H_2O}^{exh}\right) + A_{34}\left(x_{O_2}^{elec} - x_{O_2}^{exh}\right) + A_{35}\left(x_{CO}^{elec} - x_{CO}^{exh}\right) + A_{36}\left(x_{H_2}^{elec} - x_{H_2}^{exh}\right)$	**(4-4)**
O_2	$J_{O_2} = A_{41}\left(x_{N_2}^{elec} - x_{N_2}^{exh}\right) + A_{42}\left(x_{CO_2}^{elec} - x_{CO_2}^{exh}\right) + A_{43}\left(x_{H_2O}^{elec} - x_{H_2O}^{exh}\right) + A_{44}\left(x_{O_2}^{elec} - x_{O_2}^{exh}\right) + A_{45}\left(x_{CO}^{elec} - x_{CO}^{exh}\right) + A_{46}\left(x_{H_2}^{elec} - x_{H_2}^{exh}\right)$	**(4-5)**
CO	$J_{CO} = A_{51}\left(x_{N_2}^{elec} - x_{N_2}^{exh}\right) + A_{52}\left(x_{CO_2}^{elec} - x_{CO_2}^{exh}\right) + A_{53}\left(x_{H_2O}^{elec} - x_{H_2O}^{exh}\right) + A_{54}\left(x_{O_2}^{elec} - x_{O_2}^{exh}\right) + A_{55}\left(x_{CO}^{elec} - x_{CO}^{exh}\right) + A_{56}\left(x_{H_2}^{elec} - x_{H_2}^{exh}\right)$	**(4-6)**
H_2	$J_{H_2} = A_{61}\left(x_{N_2}^{elec} - x_{N_2}^{exh}\right) + A_{62}\left(x_{CO_2}^{elec} - x_{CO_2}^{exh}\right) + A_{63}\left(x_{H_2O}^{elec} - x_{H_2O}^{exh}\right) + A_{64}\left(x_{O_2}^{elec} - x_{O_2}^{exh}\right) + A_{65}\left(x_{CO}^{elec} - x_{CO}^{exh}\right) + A_{66}\left(x_{H_2}^{elec} - x_{H_2}^{exh}\right)$	**(4-7)**
NO	$J_{NO} = -\left(J_{N_2} + J_{CO_2} + J_{H_2O} + J_{O_2} + J_{CO} + J_{H_2}\right)$	**(4-8)**

Table 4-3 Protective layer diffusion equations (with methane)

Species	Equation: $(\boldsymbol{J_i}) = -\boldsymbol{C_t}\,[\boldsymbol{B}]^{-1}(\boldsymbol{\nabla x_i})$	Eq.#
N_2	$J_{N_2} = A_{11}\left(x_{N_2}^{elec} - x_{N_2}^{exh}\right) + A_{12}\left(x_{CO_2}^{elec} - x_{CO_2}^{exh}\right) + A_{13}\left(x_{H_2O}^{elec} - x_{H_2O}^{exh}\right) + A_{14}\left(x_{O_2}^{elec} - x_{O_2}^{exh}\right) + A_{15}\left(x_{CO}^{elec} - x_{CO}^{exh}\right) + A_{16}\left(x_{H_2}^{elec} - x_{H_2}^{exh}\right) + A_{17}\left(x_{NO}^{elec} - x_{NO}^{exh}\right)$	**(4-9)**
CO_2	$J_{CO_2} = A_{21}\left(x_{N_2}^{elec} - x_{N_2}^{exh}\right) + A_{22}\left(x_{CO_2}^{elec} - x_{CO_2}^{exh}\right) + A_{23}\left(x_{H_2O}^{elec} - x_{H_2O}^{exh}\right) + A_{24}\left(x_{O_2}^{elec} - x_{O_2}^{exh}\right) + A_{25}\left(x_{CO}^{elec} - x_{CO}^{exh}\right) + A_{26}\left(x_{H_2}^{elec} - x_{H_2}^{exh}\right) + A_{27}\left(x_{NO}^{elec} - x_{NO}^{exh}\right)$	**(4-10)**
H_2O	$J_{H_2O} = A_{31}\left(x_{N_2}^{elec} - x_{N_2}^{exh}\right) + A_{32}\left(x_{CO_2}^{elec} - x_{CO_2}^{exh}\right) + A_{33}\left(x_{H_2O}^{elec} - x_{H_2O}^{exh}\right) + A_{34}\left(x_{O_2}^{elec} - x_{O_2}^{exh}\right) + A_{35}\left(x_{CO}^{elec} - x_{CO}^{exh}\right) + A_{36}\left(x_{H_2}^{elec} - x_{H_2}^{exh}\right) + A_{37}\left(x_{NO}^{elec} - x_{NO}^{exh}\right)$	**(4-11)**
O_2	$J_{O_2} = A_{41}\left(x_{N_2}^{elec} - x_{N_2}^{exh}\right) + A_{42}\left(x_{CO_2}^{elec} - x_{CO_2}^{exh}\right) + A_{43}\left(x_{H_2O}^{elec} - x_{H_2O}^{exh}\right) + A_{44}\left(x_{O_2}^{elec} - x_{O_2}^{exh}\right) + A_{45}\left(x_{CO}^{elec} - x_{CO}^{exh}\right) + A_{46}\left(x_{H_2}^{elec} - x_{H_2}^{exh}\right) + A_{47}\left(x_{NO}^{elec} - x_{NO}^{exh}\right)$	**(4-12)**
CO	$J_{CO} = A_{51}\left(x_{N_2}^{elec} - x_{N_2}^{exh}\right) + A_{52}\left(x_{CO_2}^{elec} - x_{CO_2}^{exh}\right) + A_{53}\left(x_{H_2O}^{elec} - x_{H_2O}^{exh}\right) + A_{54}\left(x_{O_2}^{elec} - x_{O_2}^{exh}\right) + A_{55}\left(x_{CO}^{elec} - x_{CO}^{exh}\right) + A_{56}\left(x_{H_2}^{elec} - x_{H_2}^{exh}\right) + A_{57}\left(x_{NO}^{elec} - x_{NO}^{exh}\right)$	**(4-13)**
H_2	$J_{H_2} = A_{61}\left(x_{N_2}^{elec} - x_{N_2}^{exh}\right) + A_{62}\left(x_{CO_2}^{elec} - x_{CO_2}^{exh}\right) + A_{63}\left(x_{H_2O}^{elec} - x_{H_2O}^{exh}\right) + A_{64}\left(x_{O_2}^{elec} - x_{O_2}^{exh}\right) + A_{65}\left(x_{CO}^{elec} - x_{CO}^{exh}\right) + A_{66}\left(x_{H_2}^{elec} - x_{H_2}^{exh}\right) + A_{67}\left(x_{NO}^{elec} - x_{NO}^{exh}\right)$	**(4-14)**

NO	$J_{NO} = A_{61}\left(x_{N_2}^{elec} - x_{N_2}^{exh}\right) + A_{62}\left(x_{CO_2}^{elec} - x_{CO_2}^{exh}\right) + A_{63}\left(x_{H_2O}^{elec} - x_{H_2O}^{exh}\right) + A_{64}\left(x_{O_2}^{elec} - x_{O_2}^{exh}\right) + A_{65}\left(x_{CO}^{elec} - x_{CO}^{exh}\right) + A_{66}\left(x_{H_2}^{elec} - x_{H_2}^{exh}\right) + A_{77}\left(x_{NO}^{elec} - x_{NO}^{exh}\right)$	**(4-15)**
CH_4	$J_{CH_4} = -\left(J_{N_2} + J_{CO_2} + J_{H_2O} + J_{O_2} + J_{CO} + J_{H_2} + J_{NO}\right)$	**(4-16)**

The constants A in the flux equations represent a manipulation of the elements from matrix [B] with the total molar concentration C_t and the thickness of the protective layer. For the first system shown in Table 4-2, the total number of unknowns is 14 variables. Seven of these unknowns are for the diffusive fluxes J_i and the other seven account for the mole fractions of each exhaust gas species at the electrode interface $x_i^{electrode}$. For the second system shown in Table 4-3, this number will be 16 variables due to the addition of methane into this system.

Platinum Electrodes Modeling

The platinum electrode of the EGO sensor works as a miniature catalyst. The goal of the second module is to model all of the heterogeneous catalytic reactions that occur at the platinum electrode. The output from the second module is the occupancies of the adsorbed species on the platinum electrodes. The schematic of the second module is presented in Figure 4.4, which shows the input and output of this module.

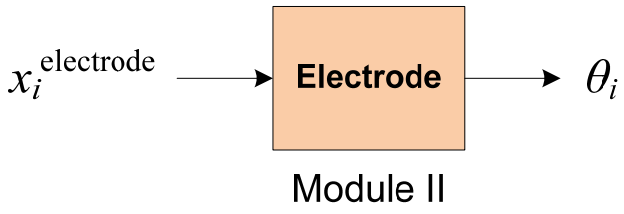

Figure 4.4 The electrode module

The occupancy (or the coverage) of each adsorbed species on the platinum electrode is calculated using Equation (2-28). For steady-state model, this equation is written as:

$$0 = r_a - r_d + \sum_j (\nu_{i,j} r_{i,j}) \tag{4-17}$$

where

r_a The adsorption rate

r_d The desorption rate

$\nu_{i,j}$ The stoichiometric coefficient between species *i* and *j*

$r_{i,j}$ The reaction rate between species *i* and *j*

Electrode Reaction Scheme without Methane

Table 4-4 shows the occupancy of each species on the electrode used in the simple model (i.e., without methane reaction). In this simple model, the number of species coverage is eight including the vacant sites (V) on the platinum electrode.

Table 4-4 Species occupancy on the electrode surface (without methane)

Index	1	2	3	4	5	6	7	8
Occupancy	O	CO	H	NO	H_2O	OH	N	V

Table 4-5 presents the complete reaction scheme used in the simple model. The symbol * denotes the vacant site. The subscript s represents the adsorbed species on the platinum active site. These elementary step reactions are taken from Auckenthaler (2005).

Table 4-5 Electrode reaction scheme without methane (Auckenthaler (2005))

		Reaction	Reaction rate	#
Adsorption	1	$O_2 + 2* \rightarrow 2O_s$	$r_{a1} = K_{a1}\theta_V x_{O_2}^{elec}$	**(4-18)**
	2	$CO + * \rightarrow CO_s$	$r_{a2} = K_{a2}\theta_V x_{CO}^{elec}$	**(4-19)**
	3	$H_2 + 2* \rightarrow 2H_s$	$r_{a3} = K_{a3}\theta_V x_{H_2}^{elec}$	**(4-20)**
	4	$NO + * \rightarrow NO_s$	$r_{a4} = K_{a4}\theta_V x_{NO}^{elec}$	**(4-21)**
	5	$H_2O + * \rightarrow H_2O_s$	$r_{a5} = K_{a5}\theta_V x_{H_2O}^{elec}$	**(4-22)**
Surface Reaction	6	$O_s + H_s \rightarrow OH_s + *$	$r_6 = K_6\theta_O\theta_H$	**(4-23)**
	7	$OH_s + * \rightarrow H_s + O_s$	$r_7 = K_7\theta_{OH}\theta_V$	**(4-24)**
	8	$OH_s + H_s \rightarrow H_2O_s + *$	$r_8 = K_8\theta_{OH}\theta_H$	**(4-25)**
	9	$H_2O_s + * \rightarrow OH_s + H_s$	$r_9 = K_9\theta_{H_2O}\theta_V$	**(4-26)**
	10	$2OH_s \rightarrow H_2O_s + O_s$	$r_{10} = K_{10}\theta_{OH}\theta_{OH}$	**(4-27)**
	11	$CO_s + O_s \rightarrow CO_2 + 2*$	$r_{11} = K_{11}\theta_{CO}\theta_O$	**(4-28)**
	12	$NO_s + * \rightarrow N_s + O_s$	$r_{12} = K_{12}\theta_{NO}\theta_V$	**(4-29)**
	13	$NO_s + N_s \rightarrow N_2 + O_s + *$	$r_{13} = K_{13}\theta_{NO}\theta_N$	**(4-30)**
	14	$2N_s \rightarrow N_2 + 2*$	$r_{d14} = K_{14}\theta_N$	**(4-31)**
Adsorption	15	$2O_s \rightarrow O_2 + 2*$	$r_{d15} = K_{d15}\theta_O$	**(4-32)**
	16	$CO_s \rightarrow CO + *$	$r_{d16} = K_{d16}\theta_{CO}$	**(4-33)**
	17	$2H_s \rightarrow H_2 + 2*$	$r_{d17} = K_{d17}\theta_H$	**(4-34)**
	18	$NO_s \rightarrow NO + *$	$r_{d18} = K_{d18}\theta_{NO}$	**(4-35)**
	19	$H_2O_s \rightarrow H_2O + *$	$r_{d19} = k_{d19}\theta_{H_2O}$	**(4-36)**

Table 4-6 lists the reaction rate equations based on the above reaction scheme. For steady state performance, the time rate of change of any occupancy will vanish to zero. For this reaction scheme, the number of elementary step reactions is 19. The number of equations resulting from this system is eight, which corresponds to the number of species occupancies.

Table 4-6 Reaction rate equations without methane

Species	Equation $\frac{\partial \theta_i}{\partial t} = r_a - r_d + \sum_j (\nu_{i,j} r_{i,j})$	Eq. #
O	$0 = r_{a1} - r_{d15} - r_6 - r_{11} + r_7 + r_{10} + r_{12} + r_{13}$	**(4-37)**
CO	$0 = r_{a2} - r_{d16} - r_{11}$	**(4-38)**
H	$0 = r_{a3} - r_{d17} - r_6 - r_8 + r_7 + r_9$	**(4-39)**
NO	$0 = r_{a4} - r_{d18} - r_{12} - r_{13}$	**(4-40)**
H_2O	$0 = r_{a5} - r_{d19} - r_9 + r_8 + r_{10}$	**(4-41)**
OH	$0 = 0 - 0 - r_7 - r_8 - 2r_{10} + r_6 + r_9$	**(4-42)**
N	$0 = 0 - 2r_{14} - r_{13} + r_{12}$	**(4-43)**
V	$\theta_V = 1 - \sum_i \theta_i$	**(4-44)**

Because the diffusion through the protective layer is governed by the adsorption/desorption rate, another set of equations is derived to balance the species concentration at the electrode interface. These equations are based on the fact that the flux of any species must be balanced by the difference between adsorption and desorption rates. Figure 4.5 shows a schematic of the species mass balance at the porous protective layer and the electrode interface. The general equation used in this mass balance is:

$$J_i = L_{elec}(r_{a,i} - r_{d,i}) \quad \textbf{(4-45)}$$

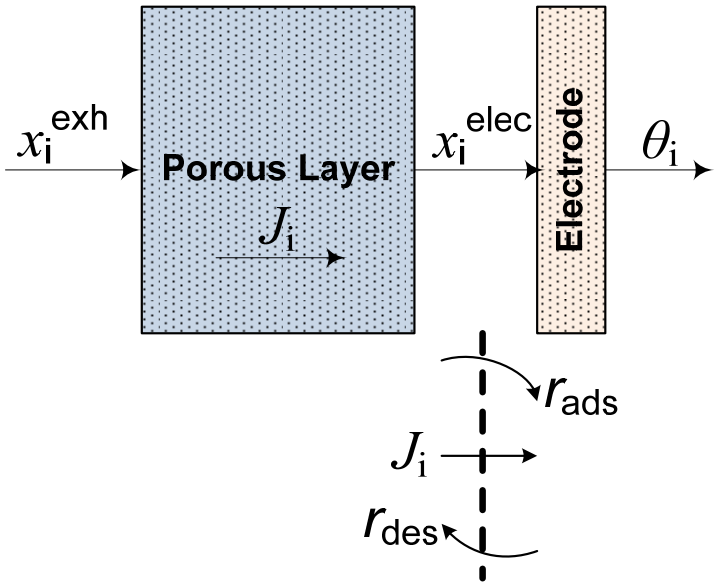

Figure 4.5 Mass balance at the electrode interface

Table 4-7 lists the set of equations that results from the interface mass balance. The number of equations is seven, which is the same number of input species.

Table 4-7 Mass balance at the electrode interface (without methane)

Species	**Equation** $J_i = L_{elec}(r_{a,i} - r_{d,i})$	**Eq. #**
O_2	$J_{O_2} = L_{elec}(r_{a1} - r_{d15})$	**(4-46)**
CO	$J_{CO} = L_{elec}(r_{a2} - r_{d16})$	**(4-47)**
H_2	$J_{H_2} = L_{elec}(r_{a3} - r_{d17})$	**(4-48)**
H_2O	$J_{H_2O} = L_{elec}(r_{a5} - r_{d19})$	**(4-49)**
NO	$J_{NO} = L_{elec}(r_{a4} - r_{d18})$	**(4-50)**
N_2	$J_{N_2} = L_{elec}(0 - 2r_{14} - r_{13})$	**(4-51)**
CO_2	$J_{CO_2} = L_{elec}(0 - r_{11})$	**(4-52)**

The total number of the unknowns is 22 variables. These variables are determined by solving this system of nonlinear equations, represented in Table 4-2 , Table 4-6, and Table 4-7, simultaneously. MATLAB® commercial software is used to solve this system of equations.

Electrode Reaction Scheme with Methane

Table 4-8 shows the number of species occupancy used in the extended model. This extended model integrates methane catalytic reactions on the platinum electrode. The number of species is nine individual species. The complete reaction scheme in this model is illustrated in Table 4-9. This scheme has 22 elementary step reactions. Six of these reactions represent the adsorption process, five represent the desorption process, and finally 11 reactions represent the surface catalytic reactions between the adsorbed species.

Table 4-8 Species occupancy on the electrode surface (with methane)

Index	1	2	3	4	5	6	7	8	9
Occupancy	O	CO	H	NO	H_2O	OH	N	C	V

This scheme has three additional reactions compared to the previous scheme that does not consider methane catalytic reactions. One of these reactions (reaction number 6) models the adsorption of methane into the platinum surface. The other two reactions (12 and 13) account for CO formation and dissociation.

Table 4-9 Electrode reactions scheme with methane (Auckenthaler (2005) and Hickman et al. (1993))

		Reaction	Reaction rate	#
Adsorption	1	$O_2 + 2* \rightarrow 2O_s$	$r_{a1} = K_{a1}\theta_V x_{O_2}^{elec}$	**(4-53)**
	2	$CO + * \rightarrow CO_s$	$r_{a2} = K_{a2}\theta_V x_{CO}^{elec}$	**(4-54)**
	3	$H_2 + 2* \rightarrow 2H_s$	$r_{a3} = K_{a3}\theta_V x_{H_2}^{elec}$	**(4-55)**
	4	$NO + * \rightarrow NO_s$	$r_{a4} = K_{a4}\theta_V x_{NO}^{elec}$	**(4-56)**
	5	$H_2O + * \rightarrow H_2O_s$	$r_{a5} = K_{a5}\theta_V x_{H_2O}^{elec}$	**(4-57)**
	6	$CH_4 + 5* \rightarrow C_s + 4H_s$	$r_{a6} = K_{a6}\theta_V x_{CH_4}^{elec}$	**(4-58)**
Surface Reaction	7	$O_s + H_s \rightarrow OH_s + *$	$r_7 = K_7\theta_O\theta_H$	**(4-59)**
	8	$OH_s + * \rightarrow H_s + O_s$	$r_8 = K_8\theta_{OH}\theta_V$	**(4-60)**
	9	$OH_s + H_s \rightarrow H_2O_s + *$	$r_9 = K_9\theta_{OH}\theta_H$	**(4-61)**
	10	$H_2O_s + * \rightarrow OH_s + H_s$	$r_{10} = K_{10}\theta_{H_2O}\theta_V$	**(4-62)**
	11	$2OH_s \rightarrow H_2O_s + O_s$	$r_{11} = K_{11}\theta_{OH}\theta_{OH}$	**(4-63)**
	12	$C_s + O_s \rightarrow CO + *$	$r_{12} = K_{12}\theta_C\theta_O$	**(4-64)**
	13	$CO_s + * \rightarrow C_s + O_s$	$r_{13} = K_{13}\theta_{CO}\theta_V$	**(4-65)**
	14	$CO_s + O_s \rightarrow CO_2 + 2*$	$r_{14} = K_{14}\theta_{CO}\theta_O$	**(4-66)**
	15	$NO_s + * \rightarrow N_s + O_s$	$r_{15} = K_{15}\theta_{NO}\theta_V$	**(4-67)**
	16	$NO_s + N_s \rightarrow N_2 + O_s + *$	$r_{16} = K_{16}\theta_{NO}\theta_N$	**(4-68)**
	17	$2N_s \rightarrow N_2 + 2*$	$r_{17} = K_{d17}\theta_N\theta_N$	**(4-69)**
Desorption	18	$2O_s \rightarrow O_2 + 2*$	$r_{d18} = K_{d18}\theta_O$	**(4-70)**
	19	$CO_s \rightarrow CO + *$	$r_{d19} = K_{d19}\theta_{CO}$	**(4-71)**
	20	$2H_s \rightarrow H_2 + 2*$	$r_{d20} = K_{d20}\theta_H$	**(4-72)**
	21	$NO_s \rightarrow NO + *$	$r_{d21} = K_{d21}\theta_{NO}$	**(4-73)**
	22	$H_2O_s \rightarrow H_2O + *$	$r_{d22} = k_{d22}\theta_{H_2O}$	**(4-74)**

Table 4-10 shows the complete set of equations that result from the above extended reaction scheme. The total number of equations is 13, which represents the mathematical model of the occupancy conservation on the platinum electrode surface.

Table 4-10 Reaction rate equations with methane

Species	**Equation** $\frac{\partial \theta_i}{\partial t} = r_{a,i} - r_{d,i} + \sum_j (\nu_{i,j} r_{i,j})$	**Eq. #**
O	$0 = r_{a1} - r_{d18} - r_7 - r_{12} - r_{14} + r_8 + r_{11} + r_{13} + r_{15} + r_{16}$	**(4-75)**
CO	$0 = r_{a2} - r_{d19} - r_{13} - r_{14} + r_{12}$	**(4-76)**
H	$0 = r_{a3} - r_{d20} - r_7 - r_9 + r_8 + r_{10} + 4r_{a6}$	**(4-77)**
NO	$0 = r_{a4} - r_{d21} - r_{15} - r_{16}$	**(4-78)**
H_2O	$0 = r_{a5} - r_{d22} - r_{10} + r_9 + r_{11}$	**(4-79)**
OH	$0 = 0 - 0 - r_8 - r_9 - 2r_{11} + r_7 + r_{10}$	**(4-80)**
N	$0 = 0 - 0 - r_{16} - 2r_{17} + r_{15}$	**(4-81)**
C	$0 = 0 - 0 - r_{12} + r_{a6} + r_{13}$	**(4-82)**
V	$\theta_V = 1 - \sum_i \theta_i$	**(4-83)**

Table 4-11 lists the set of equations that results from the interface mass balance. The number of equations is seven, which is the same number of input species.

Table 4-11 Mass balance at the electrode interface (with methane)

Species	Equation $J_i = L_{elec}(r_{a,i} - r_{d,i})$	Eq. #
O_2	$J_{O_2} = L_{elec}(r_{a1} - r_{d18})$	**(4-84)**
CO	$J_{CO} = L_{elec}(r_{a2} - r_{d19})$	**(4-85)**
H_2	$J_{H_2} = L_{elec}(r_{a3} - r_{d20})$	**(4-86)**
NO	$J_{NO} = L_{elec}(r_{a4} - r_{d21})$	**(4-87)**
H_2O	$J_{H_2O} = L_{elec}(r_{a5} - r_{d22})$	**(4-88)**
N_2	$J_{N_2} = L_{elec}(0 - r_{16} - r_{17})$	**(4-89)**
CO_2	$J_{CO_2} = L_{elec}(0 - r_{14})$	**(4-90)**
CH_4	$J_{CH_4} = L_{elec}(r_{a6} - 0)$	**(4-91)**

Electrolyte Material Modeling

This part of the model calculates the output voltage from the sensor. By applying the Nernst equation, the generated potential difference across the electrodes is correlated to the oxygen concentrations. The input/output of this module are depicted in Figure 4.6.

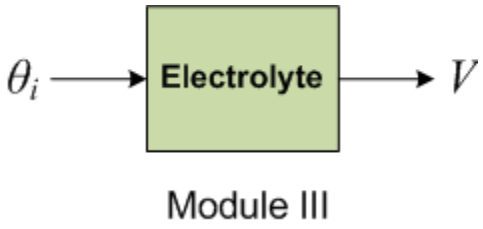

Figure 4.6 The electrolyte module

Once the adsorbed species occupancies are determined, the third module applies Nernst equation to calculate the sensor output voltage. The form of Nernst equation that used to calculate the sensor voltage is:

$$V = \frac{R_u T}{2F} ln \left[\frac{\theta_{O,ref}(\theta_v + \mathcal{K}_{COf}\theta_{CO} + \mathcal{K}_{Hf}\theta_H)}{\theta_{v,ref}(\theta_O + \mathcal{K}_{Hb}\theta_{OH})} \right] \quad \textbf{(4-92)}$$

where

$\mathcal{K}_{COf}$ The ratio between the forward reaction coefficients of CO and O.

$\mathcal{K}_{Hf}$ The ratio between the forward reaction coefficients of H and O.

$\mathcal{K}_{Hb}$ The ratio between the backward reaction coefficients of CO and O.

Equation (4-92) accounts for the effect of reducing species reactions on the platinum electrode, as discussed in detail in Chapter 2.

Chapter 5 - Results and Discussion

This chapter presents the results of the lambda sensor model. This chapter is divided into two main parts. The first part shows the validation of the developed model. In this part, the model results are compared to experimental data that is available in the open literature. The results presented in this part are based on gasoline engine exhaust emissions. To validate the model, methane was not included in this part because there is no available data from the literature that used methane as a constituent of the exhaust gas mixtures. Most of the previous work was conducted for automotive applications, and therefore, focused mainly on emissions from gasoline engines.

The second part of this chapter presents the results from the extended model that includes methane reactions on the sensor electrode. This extended model allows the use of actual natural gas engine exhaust mixtures. In this part, the model is used to interpret and analyze the data collected from the engine mapping study presented in Chapter 3.

Model Validation with Gasoline Exhaust Products

This model is composed of the equations described in Table 4-2, Table 4-6, and Table 4-7. This set of equations has 22 equations with 22 unknown variables. The inputs to this model are the typical emissions from gasoline engines as shown in Figure 5.1. This data was taken from Baker et al. (1996). Using Figure 5.1, the input exhaust gas specie mole fractions $x_i^{exhaust}$ are determined.

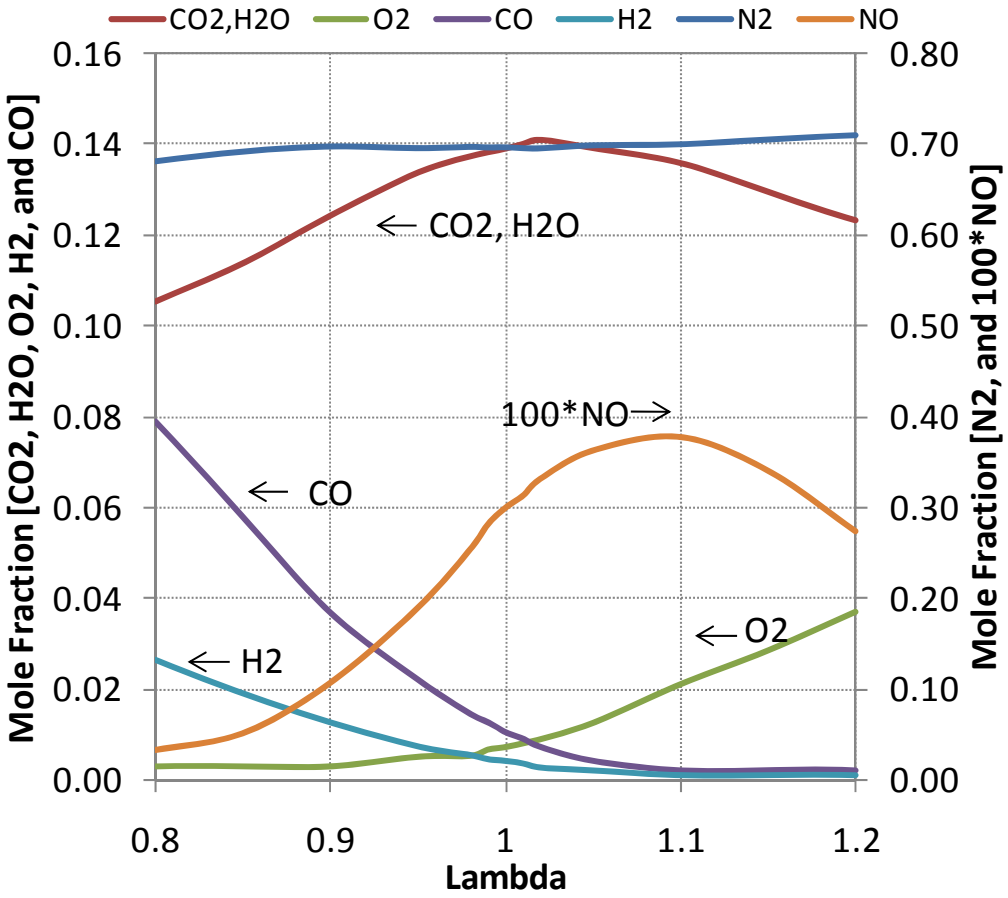

Figure 5.1 Typical exhaust gas emissions (Baker et al., 1996)

Figure 5.2 compares the output of the lambda sensor model to the experimental data. Overall, the model reproduces the experimental results with less than 6.1% difference. The measurements taken from Auckenthaler (2005) cover only the range of lambda between 0.9 and 1.1. The model accurately identifies the step change that occurs at stoichiometric conditions.

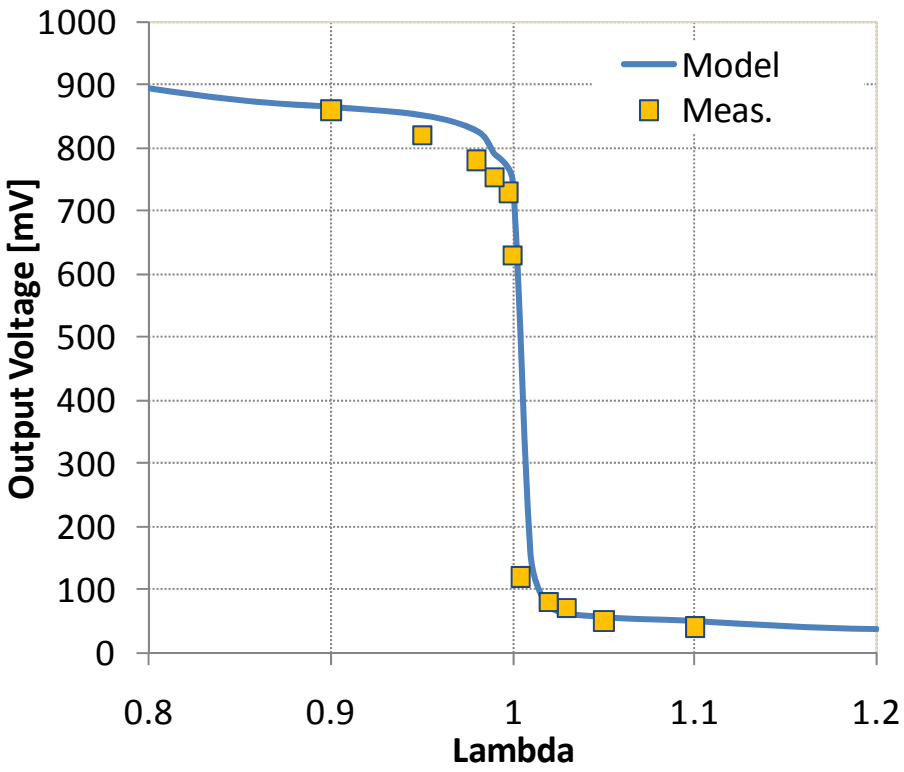

Figure 5.2 The sensor response

The modeled occupancy of each adsorbed specie on the electrode is depicted in Figure 5.3. This figure gives a clear picture of the species coverage on the measurement electrode. It is noted from this figure the abrupt change in species occupancy that occurs at stoichiometric conditions. These concentrations are completely different than the smooth behavior of the exhaust gas species, as presented in Figure 5.1. The occupancies of these species are the main driving force for the sensor output electromotive force (emf). This step change behavior is very clear for O, CO, H, and OH. The oxygen occupancy at rich conditions is of the order 10^{-6} while its value at lean conditions is approximately 0.7. The opposite behavior is observed for both CO and H. These two species (CO and H) have higher coverage values at rich conditions and switched to very low values at lean conditions. The main reason comes from the catalytic reactions that occur on the Pt. electrode. At stoichiometric conditions, the reducing species such as CO and H start to be oxidized by oxygen, creating a large decrease in their concentrations.

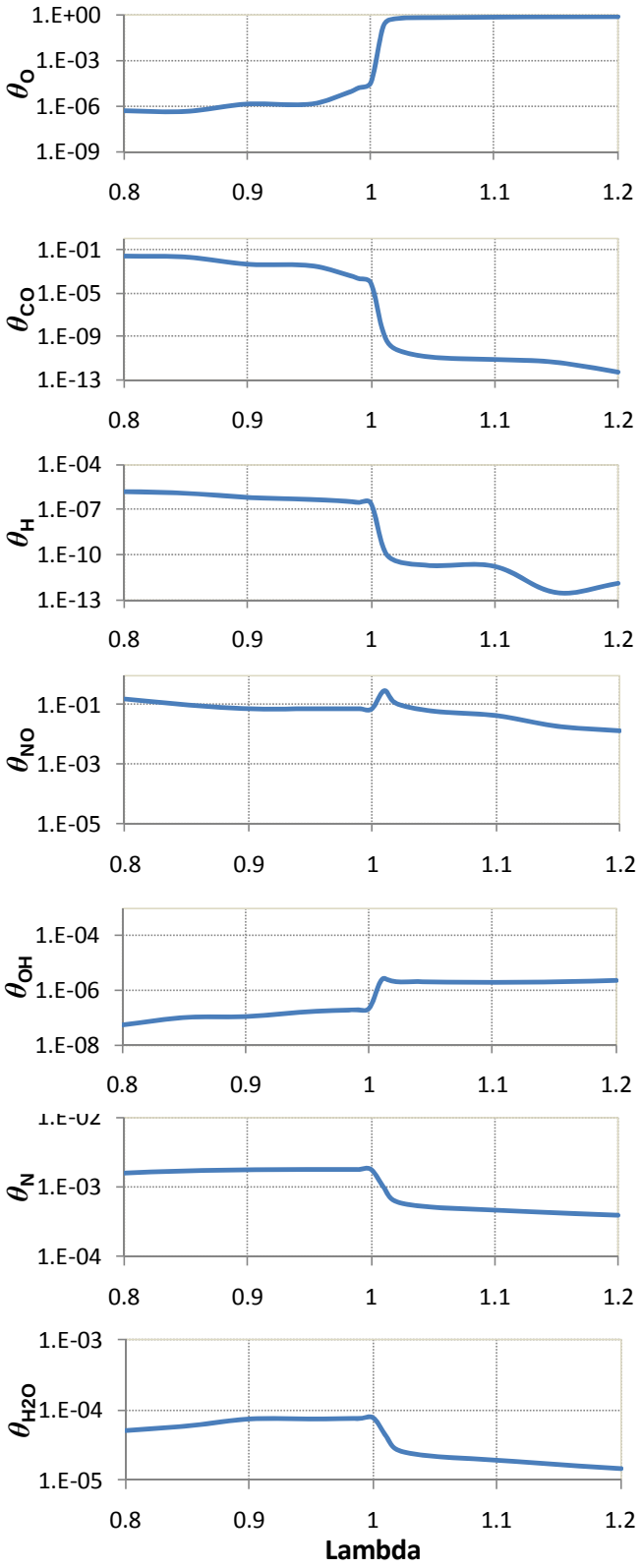

Figure 5.3 Occupancies of adsorbed species (θ in log. scale)

Figure 5.4 compares the exhaust stream mole fraction of oxygen at the sensor inlet to the oxygen at the boundary of the Pt electrode. The step change in the oxygen concentration at the stoichiometric point is clearly observed. As discussed previously, this step change is due to the oxidation of the reducing species that occurs at the stoichiometric point. It is also observed from this figure that the oxygen concentration at the electrode increases with decreasing lambda on the rich side of the stoichiometric point. This increase was not expected because the exhaust oxygen concentration is decreasing with the decrease in the air-to-fuel ratio (i.e., lambda). The mole fraction at the boundary between the protective layer and the electrode is also influenced by the desorption rate that occurs inside the electrode. This increase in oxygen mole fraction is due to the increase of oxygen released or desorbed from the electrode reaction.

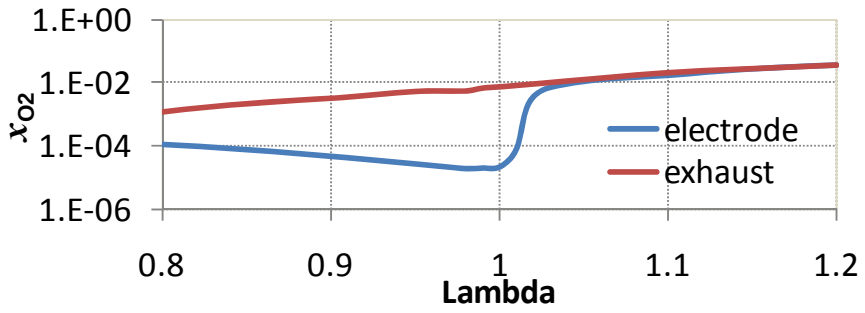

Figure 5.4 Oxygen mole fraction at both inlet exhaust and electrode

The dependence of the sensor output on exhaust gas temperature is shown in Figure 5.5. Three different temperatures are used that are 100 K apart. The research team chose the baseline temperature to be 973 K because this is the temperature used in the literature as illustrated in Figure 5.2. The trend of increasing temperature in the rich region is more pronounced than the trend in the lean region. On the lean side, the dependence of output voltage on temperature is governed by the Nernst equation as presented in equation (2-36). In the lean region, the sensor voltage increases slightly with increasing exhaust gas temperature. On the rich side, the influence of temperature is much more significant. At rich operation, the sensor output voltage decreases with increasing temperature. This voltage reduction is caused by the change in the reaction rate constants on the measured electrode. The influence of temperature on the reaction rate constant is the dominant factor at rich operation. The effect of temperature on the voltage curve shape is

also noticeable from Figure 5.5. The switch from lean to rich becomes more discontinuous at lower temperatures.

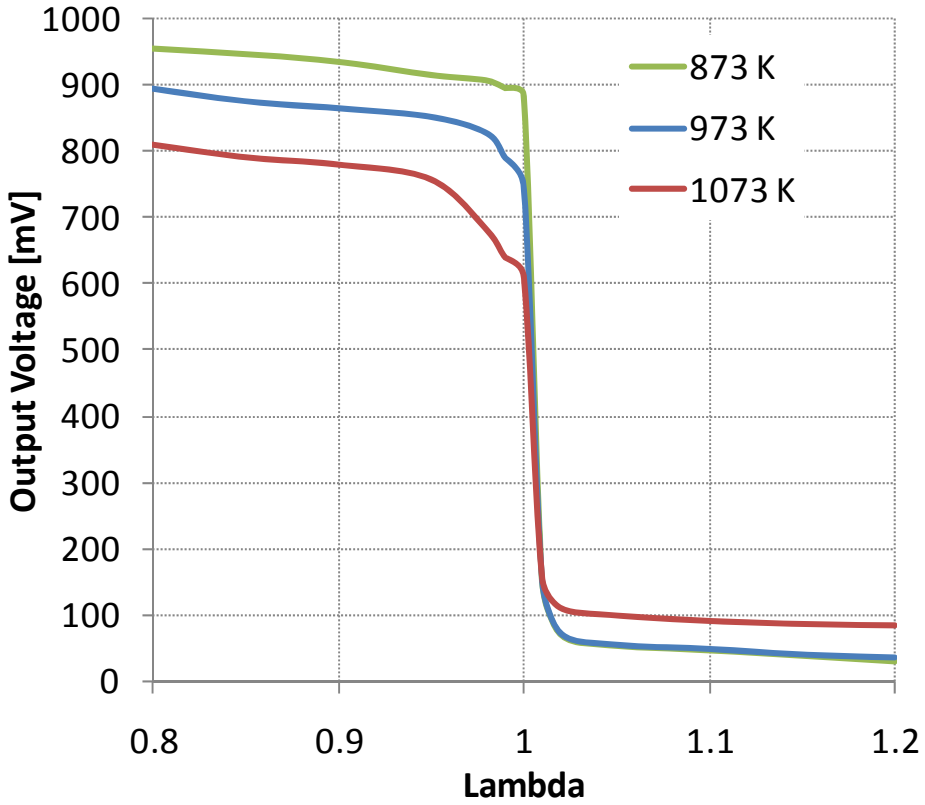

Figure 5.5 Effect of temperature on the sensor output

Figure 5.6 shows the cross-sensitivity of hydrogen and carbon monoxide on the sensor output. The vertical axis of this figure represents the difference between the sensor voltage when the input mole fraction of CO and H_2 increases by 20% and the normal species concentrations. In actual engine operation, the change of these species by 20% might be large. However, the use of this exaggerated percentage change is to show the effect of these reducing species on the sensor response. The effect of CO and H_2 in the rich region is more significant than the effect in the lean region. The highest voltage change due to the presence of these species occurs at the stoichiometric point and slightly rich condition. The typical operating operation of the NSCR system ranges between 0.98 to 1 lambda. This very narrow range is called the catalytic window of the catalytic converter. In this region, a high conversion efficiency of CO, NO_x and HC are achieved. Unfortunately, the highest deviation of sensor voltage with the change in reducing

species concentration also occurs in the same catalytic window. The cross-sensitivity of these species, then, affects the overall performance of the NSCR/AFRC system.

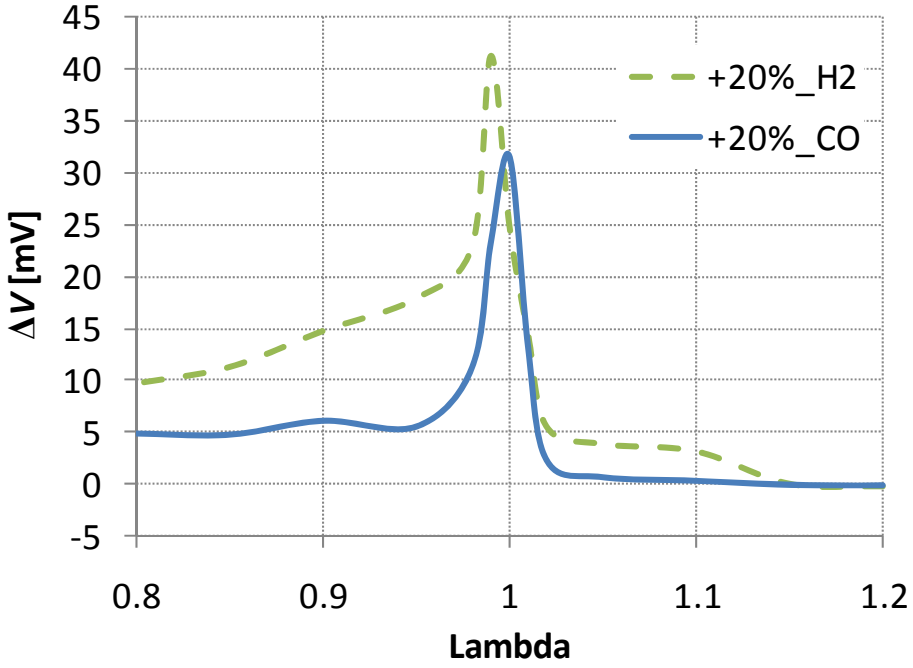

Figure 5.6 Sensor cross-sensitivity to CO and H_2

Results from Model with Methane Reactions

This section presents the results from the extended model that includes methane catalytic reactions. This model was described by the set of equations presented in Table 4-3, Table 4-10, and Table 4-11. To examine the influence of methane on the sensor performance, the research team added methane into the exhaust gas mixture as shown in Figure 5.7. This figure was used in the previous section to validate the model results with experimental data published in previous work. The exhaust emissions in this figure were originally obtained from gasoline engine testing. The author used methane with these emissions data just to examine the effect of methane addition on the sensor output. The methane concentration used in this data was assumed based on experimental data obtained in the early stages of this comprehensive project. The methane concentration is assumed to behave as the typical trend of unburned hydrocarbons. Higher concentrations of methane are obtained at rich operation due to incomplete combustion.

Emissions of methane reach a lower concentration at slightly lean operation, and then increases again due to engine combustion instabilities and misfires.

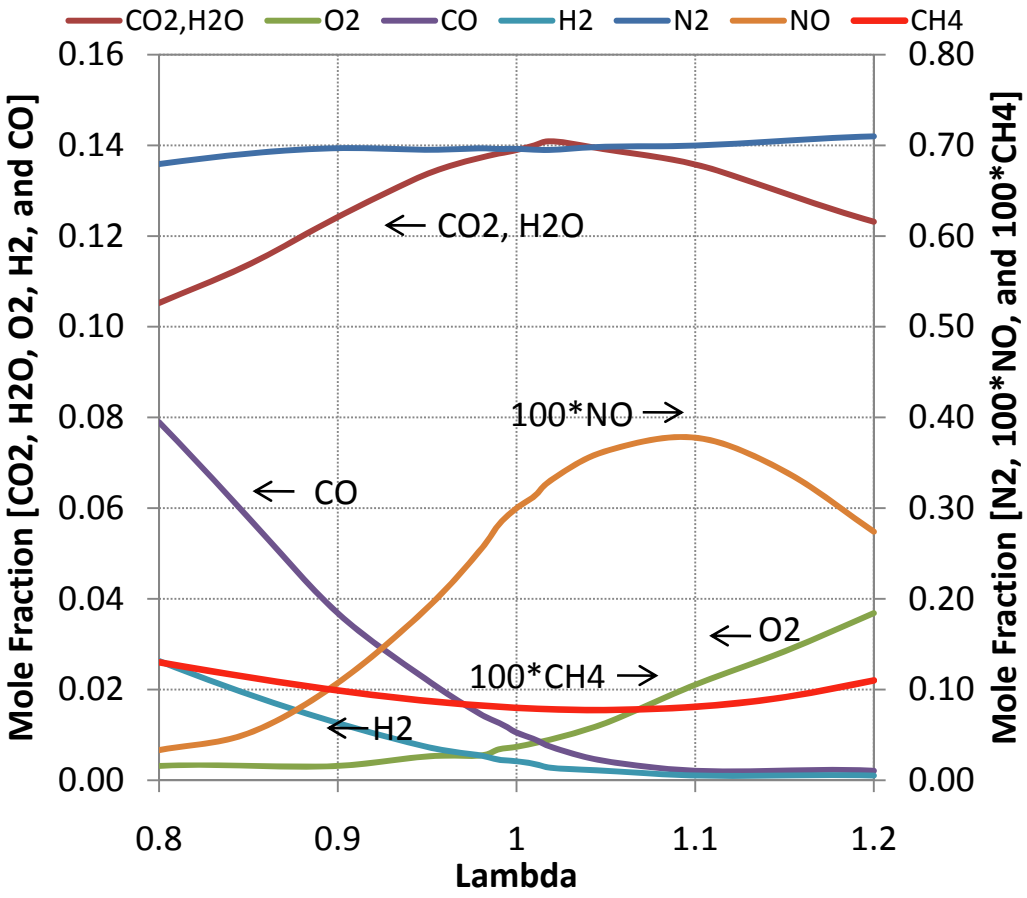

Figure 5.7 Engine exhaust emissions includes methane

Figure 5.8 shows the model sensor response for two different cases. The baseline represents the sensor output voltage without methane reactions. The dashed line represents the sensor output when methane exists in the exhaust emissions. The calculated results reveal that methane slightly increases the sensor output voltage. This figure shows that the addition of methane into the exhaust emissions has a limited effect on the sensor response. This change is not significant, but it proves the hypothesis that methane may affect the sensor performance. The increase in sensor output voltage is caused by the increase in reducing species, which are hydrogen and carbon in the electrode catalytic surface. Therefore, hydrocarbon adsorption into the platinum surface means the formation of more reducing species into the platinum electrode. These reducing species compete to consume more oxygen atoms on the catalytic surface.

Consequently, a higher output voltage is produced from the sensor causing what is called "lean shift." Lean shift is the increase in the sensor output voltage, which causes the step response of the sensor to shift toward the right side of the curve. This right shift implies that the sensor switches from lean to rich at a point leaner than the desired switch point. The insignificant effect of methane that was found from this result might be attributed to the fact that the relative percentage of methane concentration compared to the other exhaust emissions was not perfectly correct. As mentioned earlier, these emissions were originally obtained from gasoline engines. Therefore, the concentration of methane is most likely very low compared to the other emission species, such as CO and NO. The actual natural gas emissions with real percentages of each exhaust gas constituent are considered the best case to examine this model. Through the rest of this chapter, the model will be used with the actual exhaust gas mixtures from natural gas fueled engines.

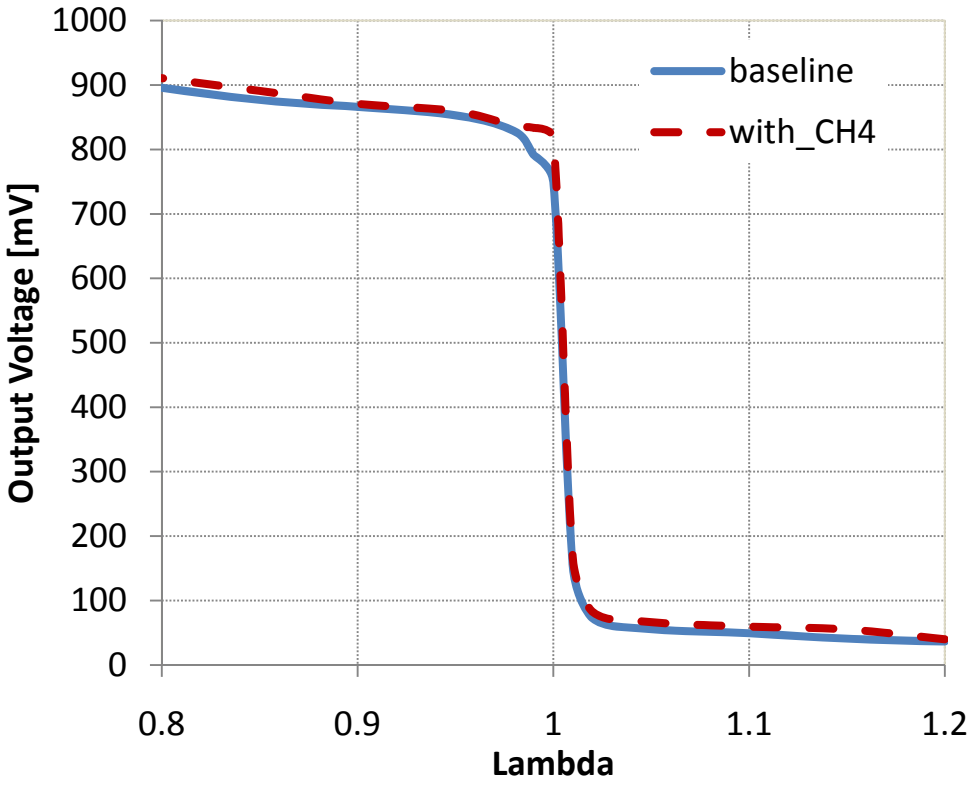

Figure 5.8 Effect of methane on the sensor output

Comparison with the Experimental Data

For actual natural gas exhaust, the model is used to deeply understand the experimental data obtained from the "Four Corners" engine mapping test. One of the goals of this modeling study is to correctly interpret the lambda sensor output. The field test data was revisited again in this section for more analysis and understanding. The model is used as a reliable tool to re-evaluate the measured data to find an explanation of the sensor unexpected behavior.

The model is used to calculate the output voltage that is presented in Figure 3.28. This experimental data represents the sensor output voltage that was collected during the engine mapping. The comparison between the model result and the measured sensor output is presented in Figure 5.9. It is shown from this figure that the model output voltage qualitatively matches the sensor voltage. The model and testing results have similar trends. Before conducting the current lambda sensor modeling study, the research team concluded that there is inconsistency in the measured sensor output voltage. The experimental data shows that there is a decrease in the sensor voltage with lower lambda (i.e., richer operation) as occurred in Test 7 and Test 32 which contradicts the inverse correlation between the sensor output voltage and lambda. Additionally, the sensor voltage measured during tests 7, 30, and 22 are almost the same even though the engine operated with three different values of lambda. The model output voltage agrees with the sensor output pattern. The model result of Test 7 and Test 32 exhibit a decrease in the sensor voltage. The decrease in the model output voltage matches the reduction obtained in the measured sensor voltage for Test 7 and Test 32. Throughout this section, the model result is presented in point instead of continuous lines because each point has a different temperature and pressure. Therefore, each point represents a specific test with specific conditions and this might explain the discontinuity in the data pattern.

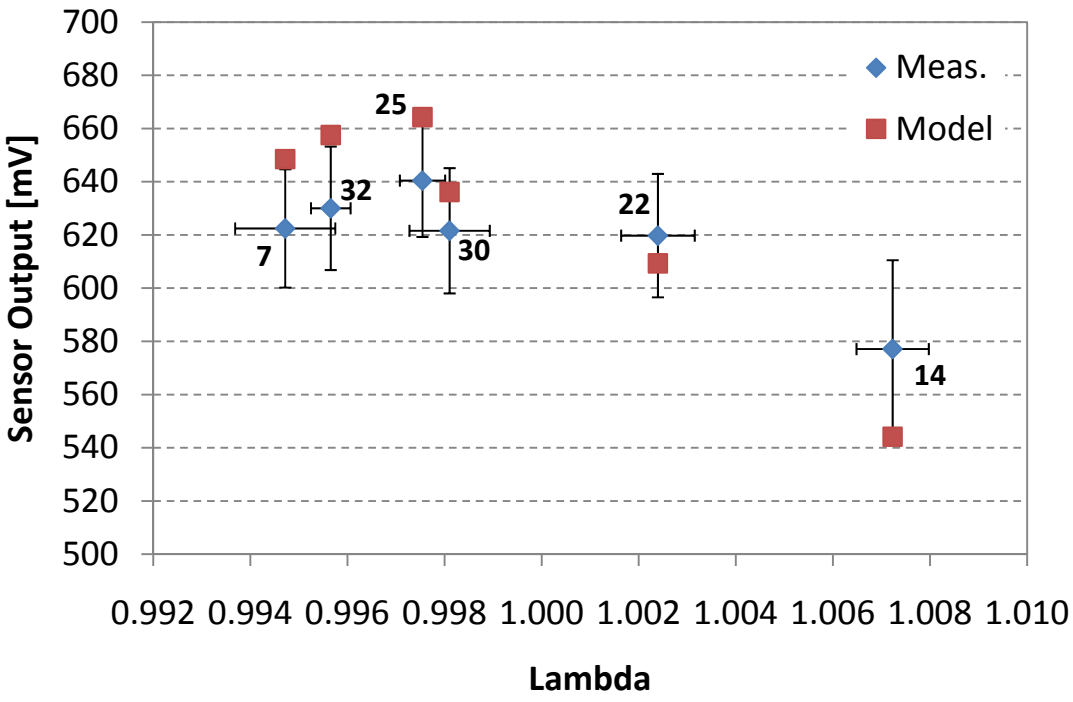

Figure 5.9 Comparison between sensor output and model result

The model results motivated the research team to understand the reason of having this reduction in the output voltage in Test 7 and Test 32. First, the electrode occupancies are the important parameters to be checked because the output voltage directly depends on their values. Figure 5.10 presents the occupancy of various species on the sensor electrode. This figure shows that the specie occupancies have similar patterns as the output voltage. The reducing species, such as CO, H and C, experience the same behavior as the sensor voltage. For those three species (CO, C, and H), the occupancy increases with decreasing lambda except for the last two points, which represent Test 7 and Test 32. The oxygen and hydroxyl species (O and OH) have an opposite trend. These two species show a decrease in occupancy with decreasing lambda except also for the Test 7 and Test 32. Figure 5.10 indicates that the model output voltage follows the same physical characteristic as the reducing specie occupancies.

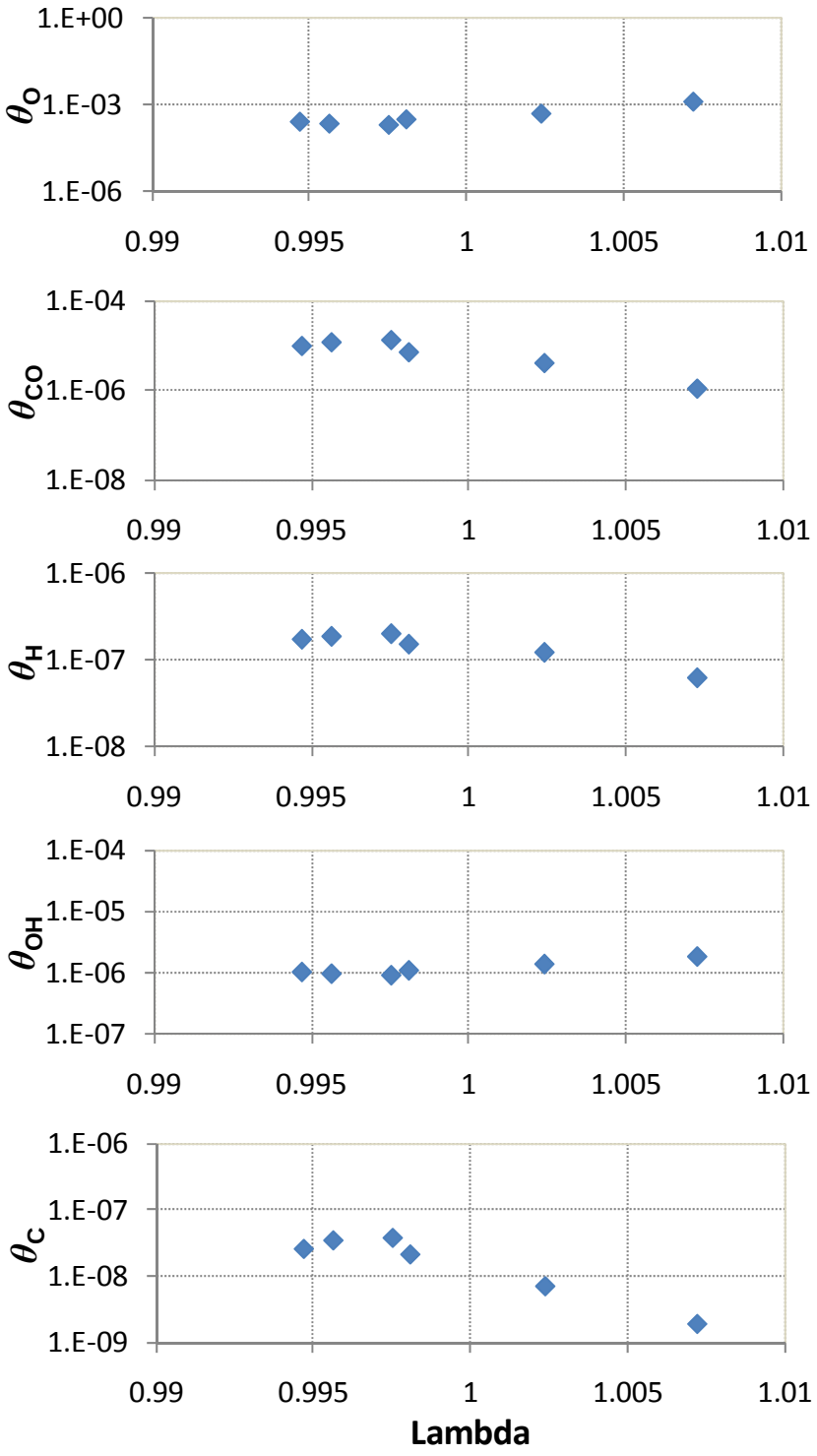

Figure 5.10 Species occupancies versus lambda

Figure 5.11 presents the effect of the reducing specie occupancies on the model output voltage. The figure shows the positive correlation between the voltage and these three reducing

species. The increase of CO, H, and C specie occupancies will result in an increase in the output voltage. The existence of these reducing species directly affects the oxygen concentration at the platinum electrode.

Figure 5.12 presents the influence of O and OH occupancies on the output voltage. It is clear from this figure that these two species have an inverse effect on the sensor output. The increase in O and OH occupancies on the platinum active sites will decrease the sensor output voltage.

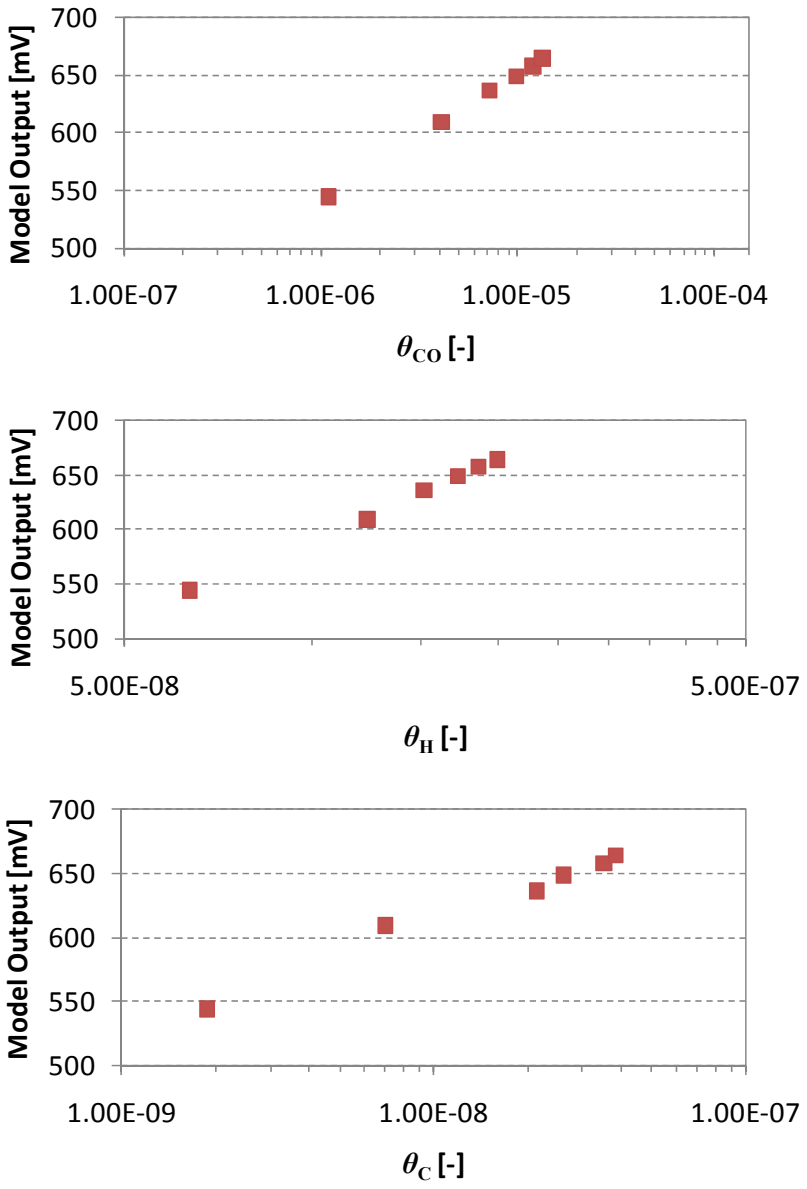

Figure 5.11 Effect of CO, H, and C occupancies on the model output

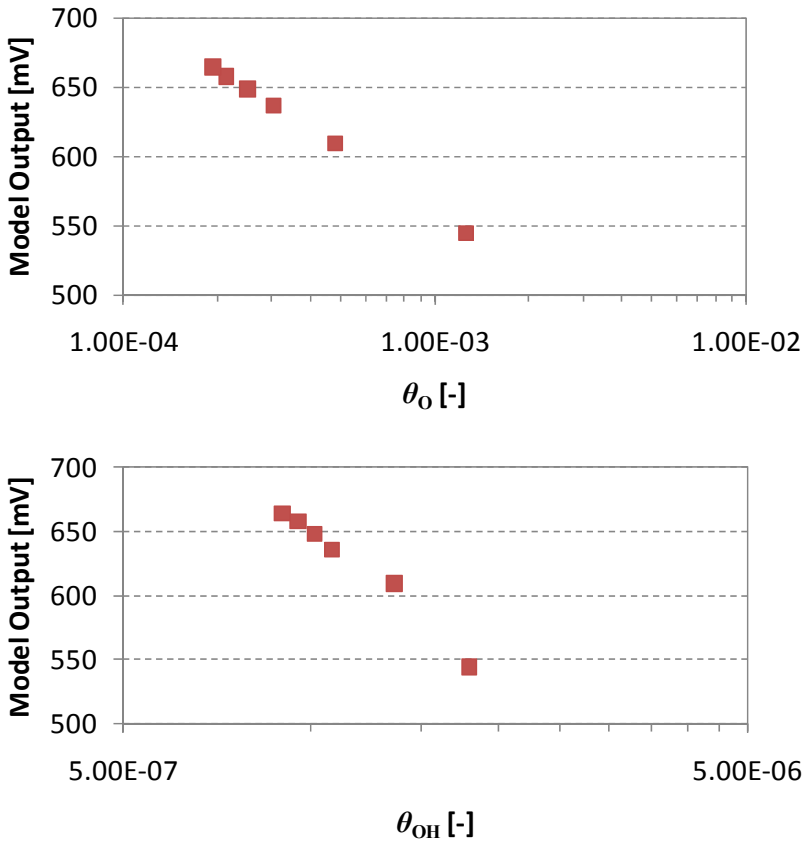

Figure 5.12 Effect of O and OH occupancies on the model output

Figure 5.11 and Figure 5.12 showed the dependence of the sensor output voltage on the electrode species occupancies. These occupancies are affected by the concentration of the reducing exhaust gas species, which mainly are CO, H_2, and CH_4. Hence, the research team analyzed the effect of reducing species on the sensor output. The analysis of the exhaust gases revealed that CO emissions significantly affect electrode occupancies and the output voltage. Figure 5.13 shows the CO concentration of the six tests measured during the engine mapping. This figure shows that the CO emission follows the output voltage and the reducing occupancies. This figure shows the reduction in CO concentration for Test 7 and Test 32. The hydrogen has a similar effect on the sensor output as discussed in the model validation (Figure 5.6).

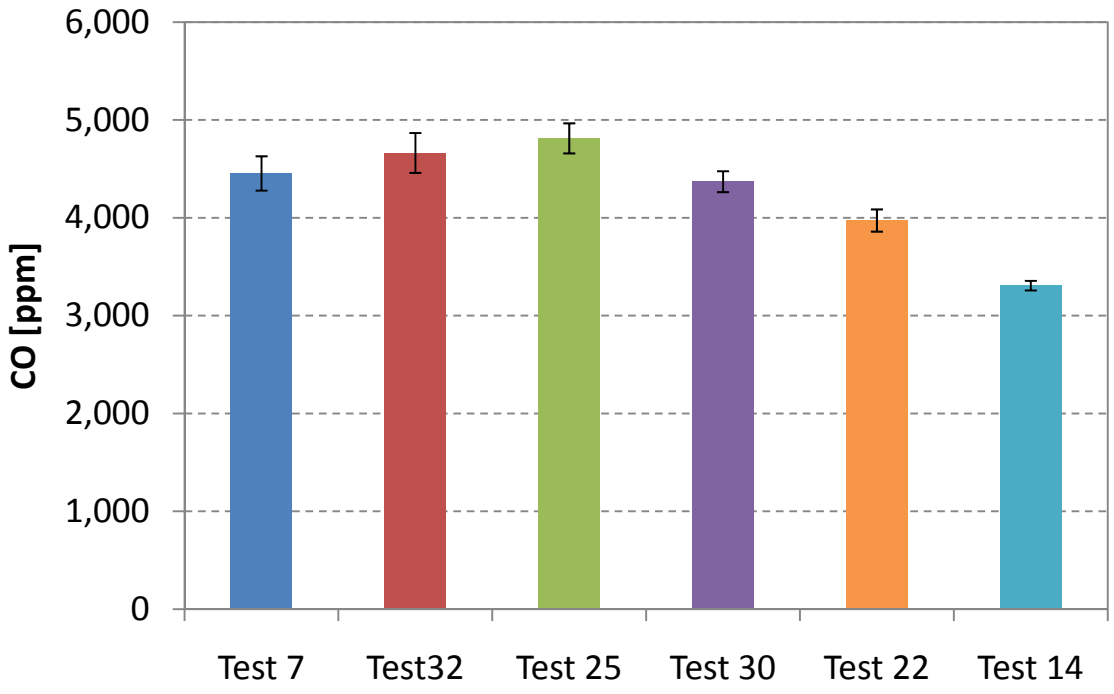

Figure 5.13 CO concentration for each mapping test

Figure 5.14 illustrates the dependence between the output voltage and the CO exhaust concentration. The figure shows that there is a correlation between CO and the voltage output obtained from the sensor as well as from the model output voltage. This correlation explains the behavior of electrode occupancies especially the reduction that occurred in Test 7 and Test 32. This effect is also applicable for hydrogen as it mentioned previously. Figure 5.14 shows that model data has steeper slope that the measured sensor data. The reason for the deviations that occurred between the model and the sensor data might be attributed to the lack of accurate information for the sensor used during this mapping. The actual properties of the sensor were not available such as the sensor geometry and the platinum electrode adsorption properties. The linear relationship of CO with the output voltage may be only valid within this small range of the testing data. The range of lambda during this mapping was 0.012, which covers the very small catalytic window around the stoichiometric point. Therefore, this linear correlation between the CO and the sensor voltage may not be generalized to a wider range of lambda.

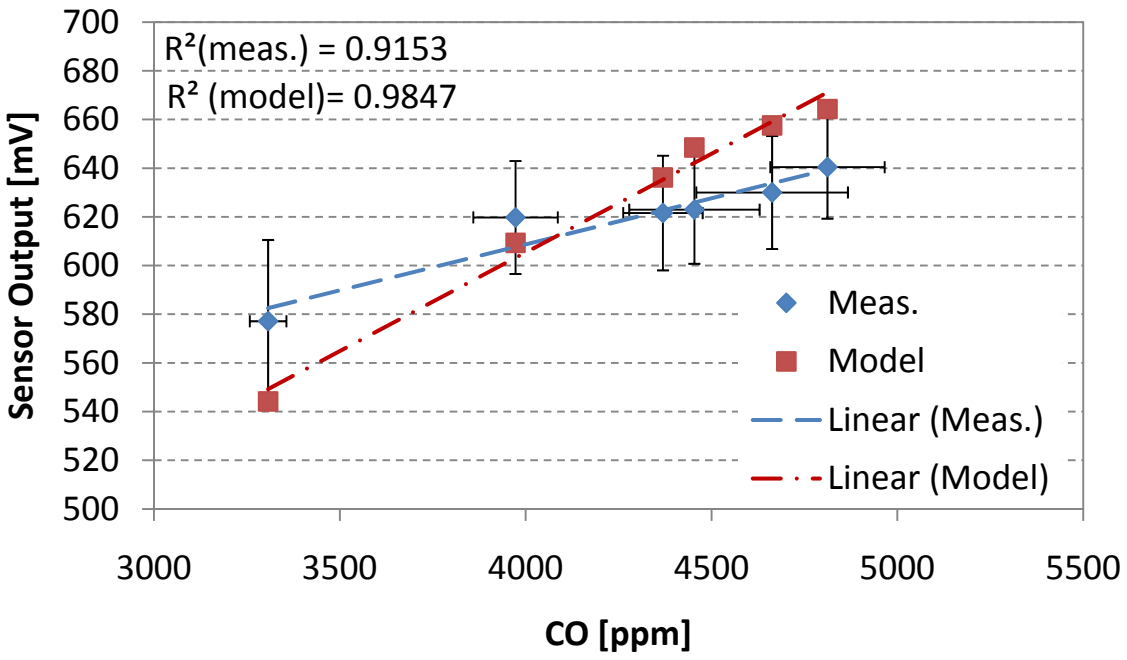

Figure 5.14 Correlation between CO concentration and sensor output

Carbon monoxide and hydrogen concentrations have a significant influence on the reducing species occupancies on the platinum active sites. Figure 5.15 shows the dependence of CO and C occupancies on the CO exhaust concentration. This figure indicates that CO mainly affects the number of platinum active sites covered by reducing species C and CO. Methane existence also might contribute to the reducing specie occupancies, however the small concentration of CH_4 compared to CO causes the effect of CO to dominate.

Figure 5.16 presents the effect of H_2 on the H occupancy. This figure shows that the H occupancy correlates directly with the hydrogen concentration. Although the H occupancy might be formed by other species such as H_2O and CH_4, there is no clear correlation that was found between these two species and the H occupancy. Because of the net formation and dissociation reactions that occur on the platinum surface, the hydrogen occupancy depends mainly on the exhaust H_2 concentration. Figure 5.17 proves that there is no clear correlation between H_2O and CH_4 concentration and the H occupancy on the sensor electrode. Also, Figure 5.18 shows that there is no correlation between the C occupancy and the CH_4 concentration.

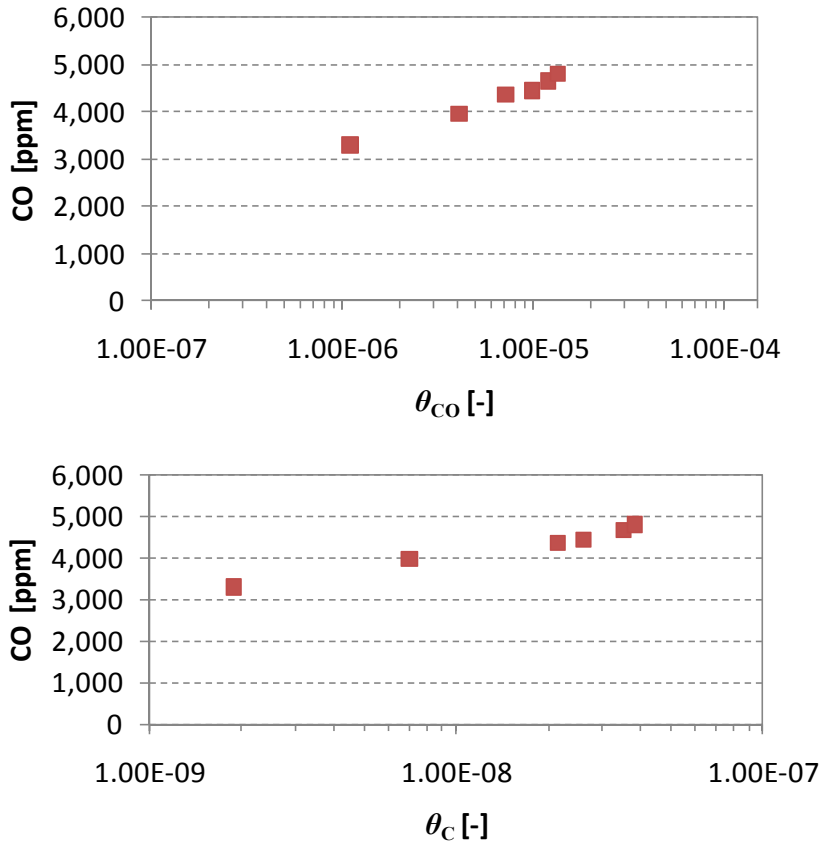

Figure 5.15 Dependence of CO and C occupancies on CO concentration

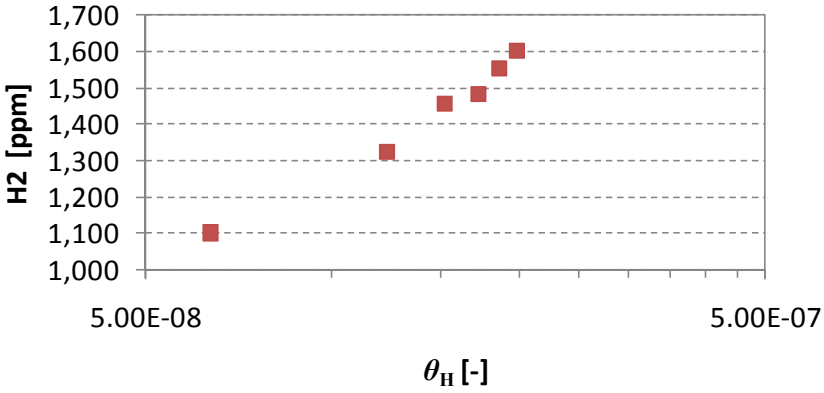

Figure 5.16 Dependence of H occupancy on H_2 concentration

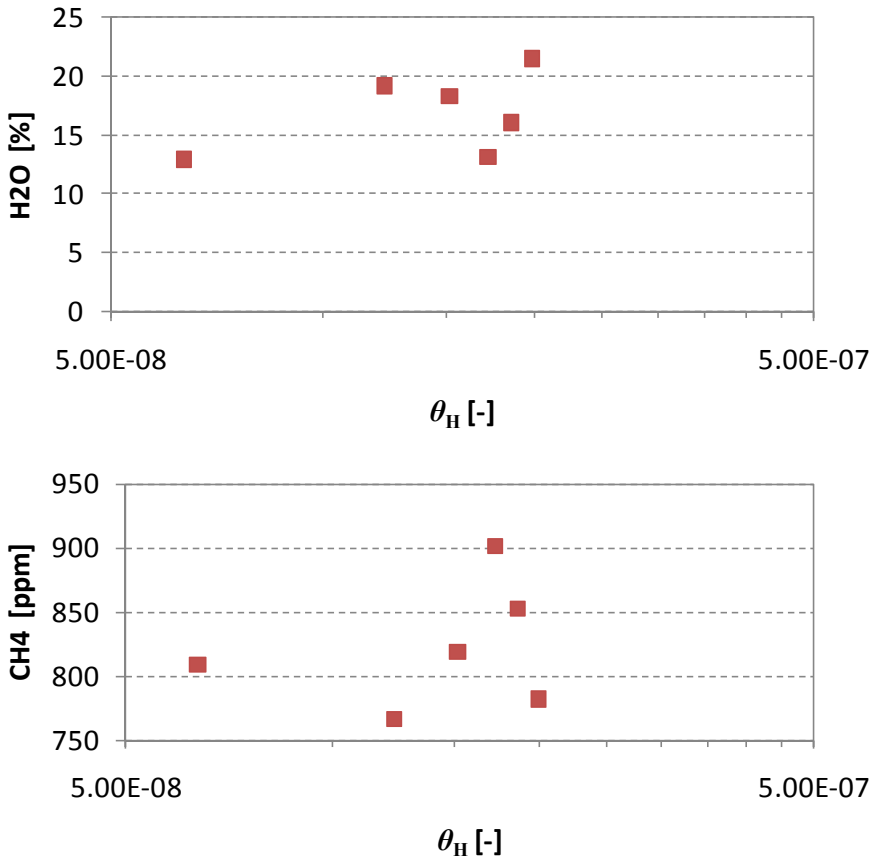

Figure 5.17 Dependence of H occupancy on CH_4 and H_2O concentrations

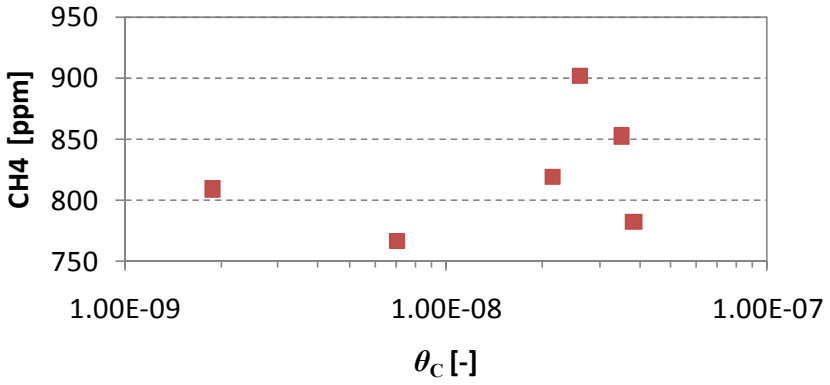

Figure 5.18 Dependence of C occupancy on CH_4 concentration

Figure 5.19 and Figure 5.20 present the influence of CH_4 and H_2O concentrations on the output voltage. These two figures show that the output voltage from the sensor and the model does not directly correlate with CH_4 and H_2O concentrations. It seems from this analysis that CO and H_2 play an important role on the sensor output. Most of the reducing specie occupancies (CO, C, and H) are mainly formed from CO and H_2 in the exhaust gas mixture. The existence of these reducing species on the Pt electrode surface directly affects the oxygen coverage, which consequently influences the sensor voltage. Figure 5.21 shows the relationship between the CO, C, H, and OH electrode occupancies on the number of oxygen occupied sites. Oxygen occupancy exhibits reverse correlation with CO, C, and H occupancies, while it has a proportional relationship with OH occupancy.

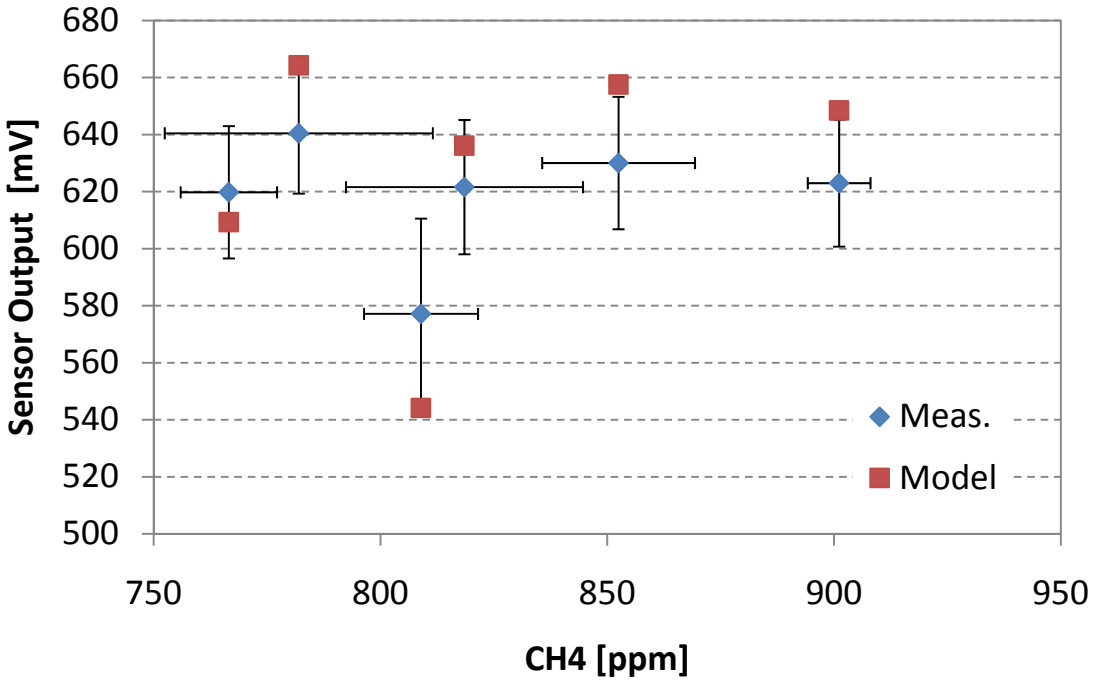

Figure 5.19 Effect of CH_4 on the sensor output

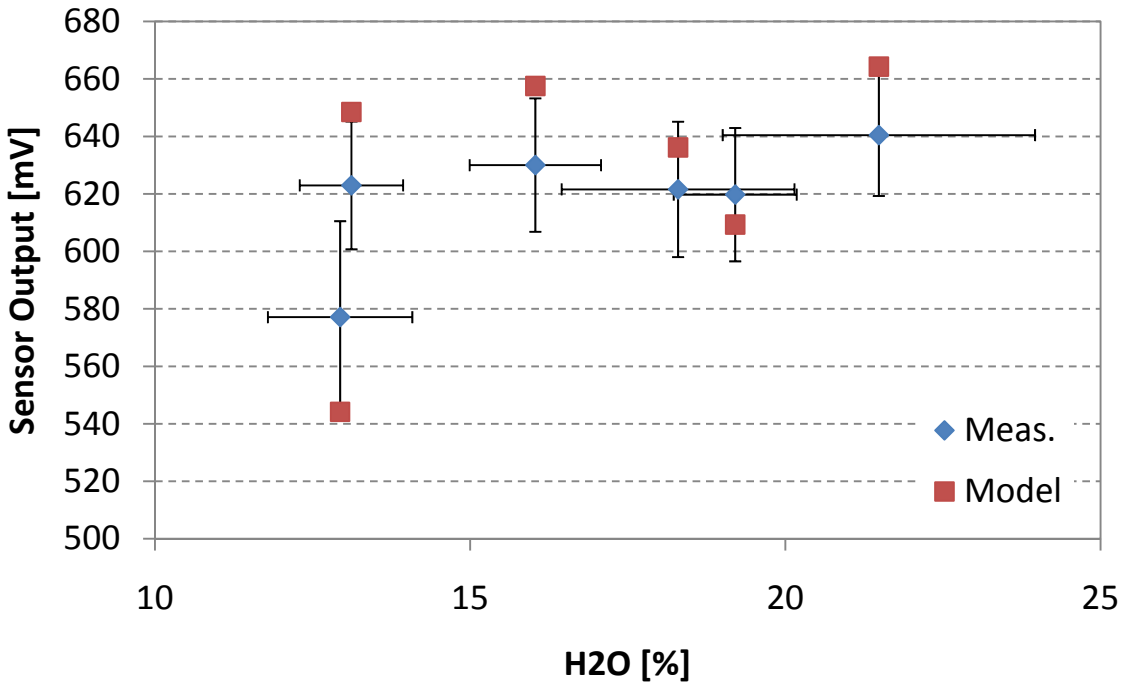

Figure 5.20 Effect of H_2O on the sensor output

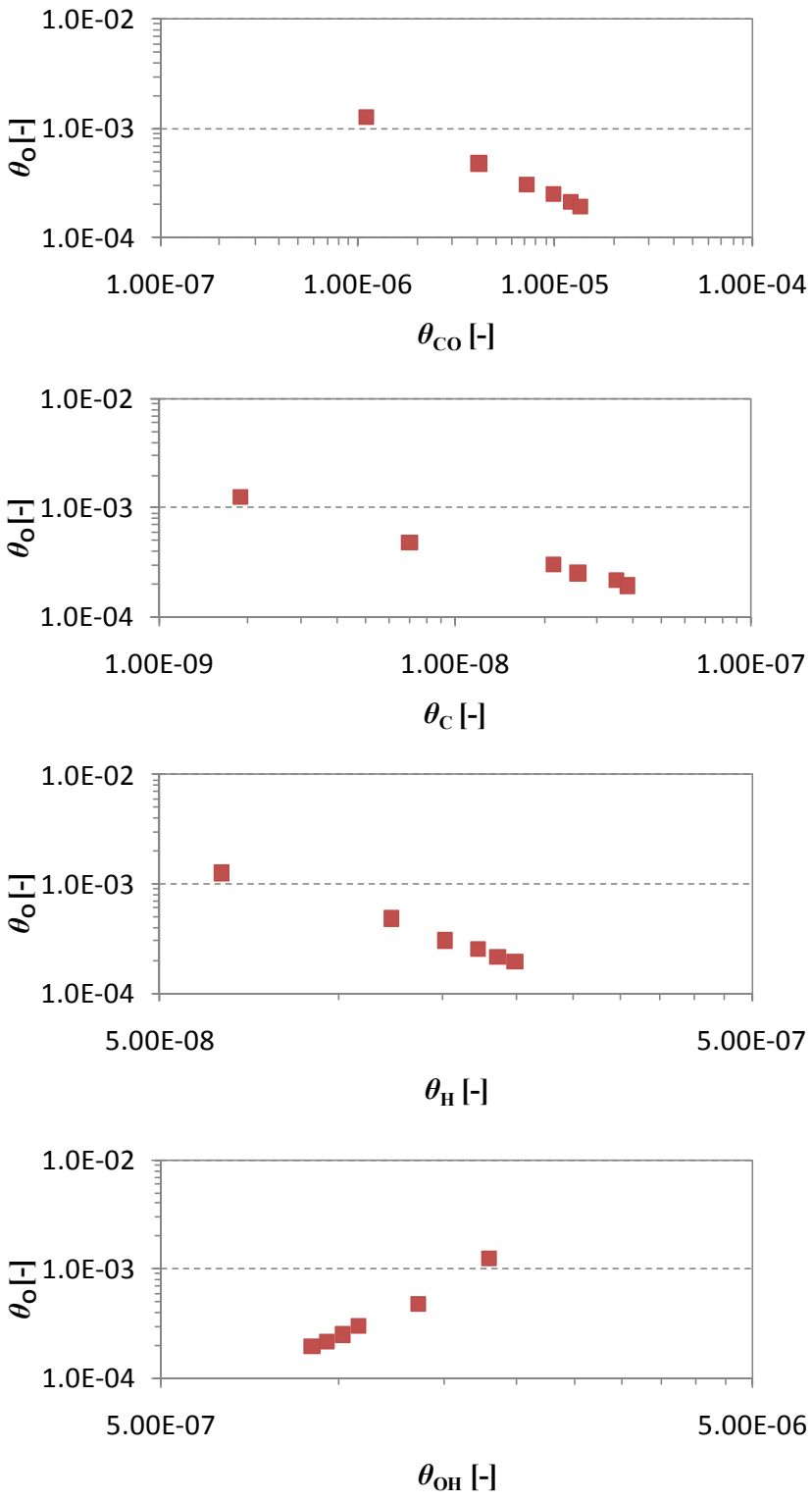

Figure 5.21 Influence of species occupancies on oxygen occupancy

It appears from this analysis that the sensor output voltage depends on the composition of the exhaust gas constituents, especially CO and H_2. The CO and H_2 have a significant impact on the concentration of the reducing species on the platinum electrode, which consequently affect the oxygen adsorbed occupancy. The decrease in the sensor output voltage that occurred during Test 7 and Test 32 is caused by the reduction in CO and H_2 concentrations. This analysis indicates that the measured sensor output voltage was not inconsistent, but that it was not interpreted correctly. The inconsistency of this experimental data was in the concentration of the exhaust gas constituents with the lambda (i.e., the air-to-fuel ratio). The question now is what causes the reduction in CO emission during tests 7 and 32 even though these two tests have a richer air-to-fuel ratio, and rich engine operation equates to higher CO emissions. The CO concentration increases with decreasing lambda. This increase did not occur during test numbers 7 and 32 as shown in Figure 5.9. The variation of engine load and ambient conditions might contribute to this inconsistency.

The model was able to capture all the physical processes that occur in the sensor. The model data is comparable with the data obtained from the literature and with the field testing data. Using this model, the engine mapping data is deeply understood and clearly explained.

Chapter 6 - Conclusions and Future Work

This thesis describes the detailed physics-based model of the lambda sensor. The developed model includes the transport of exhaust gas species through the sensor protective layer, the detailed surface catalytic reactions on the sensor electrode, and the electrochemistry of the electrolyte material. The model output voltage is very comparable to the experimental data and accurately captures the switch type trend of the lambda sensor. The model results provide a deeper insight into the various processes that occur within the sensor. The model confirms that the sensor output not only depends on the oxygen concentration, but also depends on the other exhaust gas reducing species, such as CO and H_2.

This model helps to acquire a comprehensive and detailed understanding of the underlying physics of the lambda sensor. The following points summarize the main conclusions about the lambda sensor performance drawn from this modeling study:

- The output voltage from the sensor depends mainly on the adsorbed concentration of oxygen on the Pt electrode, which is completely different than the free oxygen concentration in the exhaust gases.
- The occupancy of oxygen on the electrode active sites is controlled by the diffusion rate through the protective layers, and also by the catalytic reactions that occur on the Pt electrode itself.
- The behavior of Pt electrode catalytic reactions is similar to the performance of the ordinary catalytic converter, where the higher catalytic conversion efficiency occurred at the stoichiometric point. This explains the large decrease in species concentration at stoichiometric conditions.
- The dependence of the sensor output on the exhaust gas temperature is significant only in the rich operating range where the increase in the reaction rate constant is the dominant factor.
- The sensor performance is governed by the existence of the exhaust gas reducing species such as CO and H_2, which significantly influence the sensor output.
- The effect of methane is not significant compared to the influence of CO and H_2.

- This study confirms the fact that modeling is a reliable and robust tool to capture and improve the understanding of the complicated physics phenomena, such as in the case of the lambda sensor.

The recommendations for future work are:

- Conduct laboratory testing in a controlled environment to fine tune the model. The model is required to be validated with natural gas engine exhaust mapped for a wide range of lambda operations.
- Extend the developed model using the same approach to model the wide-band lambda (UEGO) sensor. The current model represents the main cell of the UEGO sensor. The additional cell that composes the UEGO sensor is called the "pumping cell," which pumps oxygen using external circuitry modulation. The current used through this external circuitry is proportional to the exhaust lambda.
- Develop a physics-based model of the NSCR catalytic converter. This model will focus on the simulation of the light hydrocarbons that have low carbon numbers, instead of the heavier hydrocarbons that were already covered in the previous work conducted on gasoline engine. The proposed model will be oriented mainly toward natural gas exhaust. This model will accurately model ammonia formation mechanism within the catalyst media. Also, this model will be able to quantify the formation of nitrous oxide which is considered one of the potential green house gases.
- Develop a model-based control that can be used to improve the NSCR/AFRC strategies. The controller should have a robust model of both the catalytic converter and the lambda sensor to accurately and precisely control the air-to-fuel ratio within the very narrow catalytic window.

References

Arney, G., McGivney, D., Beshouri, G., and Ashton, G., 2007, "Detection of Excess Emission Conditions for Rich Burn Engines Equipped with Non-Selective Catalytic Reduction Systems Operating at California Best Available Control Technology Limits," Proceedings of the 2007 Gas Machinery Conference, Oct. 1-3, Dallas, TX.

Auckenthaler, T.S., 2005, "Modeling and Control of Three-Way Catalytic Converter", Ph.D. thesis, Swiss Federal Institute of Technology, Zurich.

Auckenthaler, T.S., Onder, C.H., and Geering, H.P., 2002, "Modeling of a Solid-Electrolyte Oxygen Sensor," SAE paper 2002-01-1293.

Baker, R.D., and Verbrugge, M.W., 1994, "Mathematical Analysis of Potentiometric Oxygen Sensors for Combustion Gas Streams," AIChE Journal, vol. 40, no.9.

Baker, R.D., and Verbrugge, M.W., 1996, "Theory and Simulation of Solid-Electrolyte Wide-Range Sensors for Combustion-Gas Streams," J.Electrochem. Soc., Vol. 143, No. 7.

Beshouri, G., 2006, "Field Comparison of Portable Electrochemical Analyzers to a Continuous Emissions Monitoring System (CEMS) for Measurement of NO_x and CO Emissions from a Rich Burn Engine," Contract 06075, South Coast Air Quality Management District, Diamond Bar , CA.

Bird, R. Byron, Stewart, Warren E., and Lightfoot, Edwin N., 2002, "Transport Phenomena", John Wiley & Sons, Inc., 2nd edition.

Borman, G.L. and Regland, K.W., 1998, "Chemical Kinetics of Combustion," Combustion Engineering. Boston, MA: McGraw-Hill, 107-141.

Bosch's Oxygen Sensor Catalogs. URL: http://www.bosch.com.

Bowman, Craig T., 1975, "Kinetics of Pollution Formation and Destruction in Combustion," Prog. Energy Combust. Sci., Vol. 1, pp.33-45.

Brailsford, A.D., and Logothetis, E.M., 1998, "Selected Aspects of Gas Sensing," Sensors and Actuators, B: Chemical, B 52, p 195-203.

Brailsford, A.D., Yussouf, M., and Logothetis, E.M., 1993, "Theory of Gas Sensors," Sensors and Actuators, B: Chemical, B 13-14, p 135-138.

Brailsford, A.D., Yussouf, M., and Logothetis, E.M., 1996, "Theory of Gas Sensors: Response of an Electrochemical Sensor to Multi-Component Gas Mixtures," Sensors and Actuators, B: Chemical, B34, p 407-411.

Brailsford, A.D., Yussouf, M., and Logothetis, E.M., 1997, “A First-Principle Model of the Zirconia Oxygen Sensor,” Sensors and Actuators, B: Chemical, B 44, p 321-326.

Brailsford, A.D., Yussouf, M., Logothetis, E.M., and Shane, M.,1995, “Steady State Model of a Zirconia Oxygen Sensor in a Simple Gas Mixture,” Sensors and Actuators, B: Chemical, B 24-25, p 362-365.

Brailsford, A.D., Yussouf, M., Shane, M., and Logothetis, E.M., 1997, “A Model of the Transient Response of Mass-Transfer Limited Gas Sensors,” Sensors and Actuators, B: Chemical, B 45, p 27-33.

Connors, C.S., Barnes, J.C., and Mellor, A.M. 1996, “Semiempirical Predictions and Correlations of CO Emissions from Utility Combustion Turbines,” Journal of Propulsion and Power, Vol. 12, NO. 5, pp. 926-932.

Corr, R. A., Malte, P. C., and Marinov, N. M., 1991, "Evaluation of NO_x Mechanisms for Lean, Premixed Combustion," International Gas Turbine and Aeroengine Congress and Exposition, Anonymous Publ by ASME, New York, NY, USA, Orlando, FL, USA, pp. 12.

Correa, S.M., Sanjay, M., 1991, "Lean Premixed Combustion for Gas-Turbines: Review and Required Research," Proceedings of the 14th Annual Energy-Sources Technology Conference and Exhibition, Anonymous Publ. by ASME, New York, NY, USA, Houston, TX, USA, 33, pp. 1-9.

Cottrill, J., 1999, “Evaluation of Automotive Oxygen Sensors for Steady-State Air/Fuel Ratio Control and its OBD Characteristics on Natural Gas Engines,” 1999 Spring Technical Conference, ASME 1999, ASME paper No. 99-ICE-173.

Cussler, E.L., 1984, “Diffusion Mass Transfer in Fluid Systems”, Cambridge Press.

Defoort, M., Olsen, D., and Willson, B., 2004. “The Effect of Air-Fuel Ratio Control Strategies on Nitrogen Compound Formation in Three-Way Catalysts,” International Journal of Engine Research, Vol. 5, No. 1, pp. 91 – 122.

Deutschmann, O., Schmidt, R., Behrendt, F., and Warnatz, J., 1996, “Numerical Modeling of Catalytic Ignition,” Proc. Combustion Institute, 26, pp 1747-1754.

Diana K. Grauer, 2010, “Simulation and Optimization of Non-Isothermal Compressible Flow Through Large-Bore Two-Stroke Cycle Natural Gas Transmission Engines,” PhD thesis, Kansas State University, Manhattan, KS.

Energy Information Administration, August 2010, “Annual Energy Review 2009,” DOE/EIA-0384 (2009). http://www.eia.doe.gov.

Environmental Protection Agency, January 18, 2008, "Standards of Performance for Stationary Spark Ignition Internal Combustion Engines and National Emission Standards for Hazardous Air Pollutants for Reciprocating Internal Combustion Engines; Final Rule" Federal Register. 40 CFR Parts 60, 63, 85 et al.

Environmental Protection Agency, January 18, 2008. "Standards of Performance for Stationary Spark Ignition Internal Combustion Engines and National Emission Standards for Hazardous Air Pollutants for Reciprocating Internal Combustion Engines; Final Rule" Federal Register. 40 CFR Parts 60, 63, 85 et al.

Environmental Protection Energy, http://www.epa.gov.

Fenimore, C.P., 1971, "Formation of Nitric Oxide in Premixed Hydrocarbon flames," 13th Symp. (Int.) Combustion, 373-379 (1971)

Ferguson, C. R. Kirkpatrick, A. T., 2001, 2nd, "Internal Combustion Engines: Applied Thermosciences," John Wiley & Sons, New York, pp. ISBN: 0-471-35617-4.

Fleming, J.W.,1977, "Device Model of the Zirconia Oxygen Sensor," SAE Trans., paper 770400.

Fogler, H. S.,1999, "Elements of Chemical Reaction Engineering", Prentice-Hall, 3rd edition.

Four Corners Air Quality Task Force, 2007, "Four Corners Air Quality Task Force Report of Mitigation Options," Retrieved July 17. 2008 from http://www.nmenv.state.nm.us/aqb/4C/DraftTaskForce Report.html

Fuller, E.N., Schettler, P.D., Giddings, J.C, 1966, "A New Method for Prediction of Binary Gas-Phase Diffusion Coefficients", Ind. Eng. Chem., 58(5), 18.

Granger, P., Dathy, C., Lecomte, J.J., Leclercq, L., Prigent, M., Mabilon, G., and Leclercq, G., 1998, "Kinetics of the NO and CO Reaction Over Platinum Catalysts, I. Influence of the Support," Journal of Catalysis, 173:304-314.

Hagen, J., 2006, "Industrial Catalysis-A Practical Approach", Willey-VCH, 2nd edition.

Harmsen, J., Hoebink, J., and Schouten, J., 2001, "NO Reduction by CO over Automotive Exhaust Gas Catalysts in the Presence of O2," Catalysis Letters Vol. 71, No. 1-2.

Heeb, N.V., Forss, A., Brühlmann, S., Lüscher, R., Saxer, C., and Hug, P, 2006, "Three Way Catalyst Induced Formation of Ammonia—Velocity- and Acceleration-Dependent Emission Factors," Atmospheric Environment, 40, pp. 5986-5997.

Hewood, J.B., 1998, "Internal Combustion Engine Fundamentals," McGraw-Hill Inc., New York, NY.

Hickman, D.A., and Schmidt, L.D., 1993, "Steps in CH_4 Oxidation on Pt and Rh Surfaces: High-Temperature Reactor Simulations" AIChE Journal, Vol. 39, No. 7.
Higgins, B.G., 2008, Mass Transfer Lecture Notes, UCDavis.

Hines, A.L. and Maddox, R.N. 1985, "Mass Transfer: Fundamentals and Applications," Prentice Hall, New Jesey.

Holman, J.P., 2000, "Experimental Methods for Engineers," McGraw-Hill's, 7th edition.

International Energy Agency, 2010, "World Energy Outlook 2010 Factsheet." http://www.iea.org.

Interstate Natural Gas Association of America, 2009, "Natural Gas Pipeline and Storage Infrastructure Projections through 2030." http://www.ingaa.org.

Kumar, K.V., Porkodi, K., and Roch, F., 2008, "Langmuir-Hinshelwood Kinetics- A theoretical study", Catalysis Communications 9.

Kummer, J. T., 1980, "Catalysts for automobile emission control," Progress in Energy and Combustion Science, Vol. 5, No .2, pp. 77 – 199.

Kuo, K.K., 2005, "Principle of Combustion,"2nd ed., John Wiley & Sons, New York, NY.

Lambert, D. C., 1995. "Current Design, Operation, Performance, and Costs of 3-way Catalysts on Stationary Natural Gas Engines," 1995 Fall Technical Conference of the ASME Internal Combustion Engine Division, Vol. 4, No. 25, pp. 91 – 102.

Law, C.K., Makino, A., and Lu, T.F., 2005,"On the off-Stoichiometric Peaking of Adiabatic Flame Temperature," the 4th Joint Meeting of the U.S. Sections of the Combustion Institute, March 21-23, Drexel University.

Lefebvre, A.H., 1999, "Gas Turbine Combustion," Taylor & Francis, Philadelphia, ISBN: 1-56032-673-5.

Mario Balenovic, 2002, "Modeling and Model-Based Control of a Three-Way Catalytic converter," PhD thesis, Technische Universiteit Eindhoven, Eindhoven, Netherland.

McFarland, J., Grauer, D.K., Chapman, K.S., 2010,"Characterization of Exhaust Pollutant Emissions for Design, Implementation, and Validation of After-Treatment System Effectiveness," Gas Machinery Conference, October 4-6, Phoenix, AZ.

Mizusaki, J., Amano, K., Yamauchi, S., and Fueki, K., 1987, "Electrode Reaction at Pt, O2(g)/Stabilized Zirconia Interface. Part II: Electrochemical Measurements and Analysis," Solid State Ionics, 22:323-330.

Mizusaki, J., Amano, K., Yamauchi, S., and Fueki, K., 1987,"Electrode Reaction at Pt, O2(g)/Stabilized Zirconia Interface. Part I: Theoretical Consideration of Reaction Model," Solid State Ionics, 22:323-330.

Mizusaki, J., Tagawa, H., Miyaki, Y., Yamauchi, S., Fueki, K., Koshiro, I., and Hirano, K., 1992, "Kinetics of the Electrode Reaction at the CO-CO_2, porous Pt/Stabilized Zirconia Interface," Solid State Ionics, 53-56, 126-134.

Mizutani, A., Okawa, T., Matsuzaki, H., Kubota, H., and Hosogai, S., 1998, "Oxygen Sensor for CNG Application as ULEV or Tighter Emission Vehicle," SAE paper 980264.

Nicol, D. G., Steele, R. C., and Marinov, N. M., 1995, "Importance of the Nitrous Oxide Pathway to NO_x in Lean-Premixed Combustion," Journal of Engineering for Gas Turbines and Power, Transactions of the ASME, 117(1) pp. 100-111.

Peyton Jones, J.C., and Jackson, R.A., 2003, "Potential and Pitfalls in the Use of Dual Exhaust Gas Oxygen Sensors for Three-Way Catalyst Monitoring and Control," IMechE Proceedings, Part D: Journal of Automobile Engineering, 217, p 475-487.

Phillip, S., online lectures, http://www.crsim.utah.edu/Classes/6603/index.html.

Pipeline Research Council International, Inc. (2005). Pipeline engine emissions control roadmap: Technology pathways to cost-effective year 2010 reciprocating engine emissions compliance.

Potamianou, S.F., and Th. Thoma, K.A., 1994, "A Study of Ion Transport in Zirconia through Computer Modeling," Solid State Ionics, 70/71, 533-536.

Ramamoorthy, R., Dutta, P.K., and Akbar, S.A., 2003, "Oxygen Sensor: Materials, Methods, Designs and Applications," Journal of Material Science 38, p4271-4282.

Reid, R.C., Prausnitz, J.M., and Poling, B.E, 1987,"The Properties of Gases and Liquids", 4th edition, McGraw-Hill, New York.

Renewable Energy Policy Project, Issue Brief no. 15, 2000, "A Guide to the Clean Air Act for the Renewable Energy Community", by David R. Wooley.

Riegel, J., Neumann, H., and Wiedenmann, H.-M., 2002,"Exhaust Gas Sensor for Automotive Emission Control," Solid State Ionics, 152-153, pp. 783-800.

Riegel,J., Neumann, H., and Wiedenmann, H.-M., 2002, "Exhaust Gas Sensors for Automotive Emission Control," Solid State Ionics.

Robertson, N.L., and Michaels, J.N., 1990, "Oxygen Exchange on Platinum Electrodes in Zirconia Cells: Location of Electrochemical Reaction Sites," J.Electrochem. Soc., Vol. 137, No. 1.

Satterfield, C.N., 1991, “Heterogeneous Catalysis in Industrial Practice”, McGraw-Hill’s, 2nd edition.

Taylor, R., and Krishna, R, 1993, “MULTICOMPONENT MASS TRANSFER”, Wily series in chemical engineering, New York, USA.

Toema, M., Nuss-Warren, S., and Chapman, 2009, “Long-Term Emission Performance of Stationary Engines Equipped with NSCR System,” Gas Machinery Conference, October 5-7, Atlanta, GA.

Toema, M., Nuss-Warren, S., Chapman, K.S., McCarthy, J., and McGrath, T., 2009, “Mapping Study To Characterize NSCR Performance on A Natural Gas-Fueled Engine,” Proceedings of the 2009 Spring Internal Combustion Engine Division Technical Conference, ICES2009-76120, May3-6, Milwaukee, WI.

Toof, J. L., 1985, "Model for the Prediction of Thermal, Prompt, and Fuel NO_x Emissions from Combustion Turbines," 30th International Gas Turbine Conference and Exhibit. Anonymous ASME, New York, NY, USA, Houston, TX, USA, pp. 8.

Tsagarakis, E., and Weppner, W., 2005, “Electrode Kinetics Phenomena of Solid State Ionic Devices,” Ionics II.

Turns, S.R., 2000, “An Introduction to Combustion: Concepts and Applications, ” WCB/McGraw-Hill, Boston, pp. ISBN: 0-07-235044-x.

Vosz, A., Midlam-Mohler, S., Guezennec, Y., and Yurkovich, S., 2006, “Experimental Investigation of Switching Oxygen Sensor Behavior Due To Exhaust Gas Effects,” Proceedings of IMECE2006, 2006 ASME International Mechanical Engineering Congress and Exposition, Nov. 5-10, 2006, Chicago, IL. ASME, IMECE Paper No. 2006-14915.

Wesselingh, J.A., and Krishna, R, 2006, “Mass Transfer in Multicomponent Mixtures”, VSSD, Delft, Netherlands.

Westbrook, C.K. and Dryer, F.L., 1984, “Chemical Kinetic Modeling of Hydrocarbon Combustion,” Progress in Energy and Combustion Science, Vol. 10, pp 1-57.

Zhuiykov, S., 2006, “Electron Model of Solid Oxygen-Ionic Electrolytes Used in Gas Sensors,” Int. J. Appl. Ceram. Tech., 3[5] 401-411.

Appendix A - Derivation of the Maxwell-Stefan Equation

This appendix presents a simple approach to drive the Maxwell-Stefan equation (Higgins, 2008). Consider a simple binary case, where species A diffuses into species B.

The molar diffusive flux of species A relative to the molar average velocity u^* is given by

$$J_A = C_A(u_A - u^*) = -C_t D_{AB} \nabla x_A \quad \textbf{(A-1)}$$

This equation can be rewritten as

$$D_{AB} \nabla x_A = -\frac{C_A}{C_t}(u_A - u^*) = -x_A(u_A - u^*) \quad \textbf{(A-2)}$$

There is an equivalent equation for species B

$$D_{BA} \nabla x_B = -x_B(u_B - u^*) \quad \textbf{(A-3)}$$

By knowing that $x_A + x_B = 1$ and $D_{AB} = D_{BA}$, the above equation can rearranged to get

$$D_{AB} \nabla x_A = x_B(u_B - u^*) \quad \textbf{(A-4)}$$

Solving for average molar velocity u^* gives

$$u^* = u_B - \frac{D_{AB}}{x_B} \nabla x_A \quad \textbf{(A-5)}$$

Subtitling into equation (A-2) gives

$$D_{AB} \nabla x_A = -x_A \left(u_A - u_B + \frac{D_{AB}}{x_B} \nabla x_A \right) \quad \textbf{(A-6)}$$

hence,

$$D_{AB} \nabla x_A = -x_A x_B (u_A - u_B) \quad \textbf{(A-7)}$$

The above equation can generally be applied to multi-component system as follows:

$$\nabla x_i = \sum_{j=1}^{n} \frac{x_i x_j (u_j - u_i)}{D_{ij}} \quad \textbf{(A-8)}$$

This is the form of the M-S equation expressed in species velocities. The M-S can be rewritten in terms of diffusive fluxes:

$$\nabla x_i = \sum_{j=1}^{n} \frac{x_i x_j}{D_{ij}} \left(\frac{J_j}{C_j} - \frac{J_i}{C_i} \right) \quad \textbf{(A-9)}$$

By knowing the definition of

$$x_i = \frac{C_i}{C_t} \quad \textbf{(A-10)}$$

$$\nabla x_i = \sum_{j=1}^{n} \frac{x_i J_j - x_j J_i}{C_t D_{ij}} \quad \textbf{(A-11)}$$

This equation is another form of M-S equation in terms of diffusion fluxes.

Manipulation of M-S equation

$$C_t \nabla x_i = \sum_{j=1}^{n} \frac{x_i J_j}{D_{ij}} - J_i \sum_{j=1}^{n} \frac{x_j}{D_{ij}} \quad \textbf{(A-12)}$$

Since,

$$\sum_{j=1}^{n} J_j = 0 \quad \textbf{(A-13)}$$

$$\therefore J_n = -\sum_{j=1}^{n-1} J_j \quad \textbf{(A-14)}$$

$$C_t \nabla x_i = \sum_{j=1}^{n-1} \frac{x_i J_j}{D_{ij}} + x_i \frac{J_n}{D_{ij}} - J_i \sum_{j=1}^{n} \frac{x_j}{D_{ij}} \quad \textbf{(A-15)}$$

Substituting for J_n

$$C_t \nabla x_i = \sum_{j=1}^{n-1} \frac{x_i J_j}{D_{ij}} - x_i \sum_{j=1}^{n-1} \frac{J_n}{D_{ij}} - J_i \sum_{j=1}^{n} \frac{x_j}{D_{ij}} \quad \textbf{(A-16)}$$

$$C_t \nabla x_i = \sum_{j=1}^{n-1} x_i \left(\frac{1}{D_{ij}} - \frac{1}{D_{in}} \right) J_j + \left(\frac{x_i J_i}{D_{ii}} - \frac{x_i J_i}{D_{in}} \right) - J_i \sum_{j=1}^{n} \frac{x_j}{D_{ij}} \quad \textbf{(A-17)}$$

In a similar way we can take out the i^{th} component from the last summation

$$J_i \sum_{j=1}^{n} \frac{x_j}{D_{ij}} = J_i \sum_{j=1, j \neq i}^{n} \frac{x_j}{D_{ij}} + \frac{x_i J_i}{D_{ii}} \quad \textbf{(A-18)}$$

Using this result we can regroup terms to get

$$C_t \nabla x_i = \sum_{j=1, j \neq i}^{n-1} x_i \left(\frac{1}{D_{ij}} - \frac{1}{D_{in}} \right) J_j - \frac{x_i J_i}{D_{in}} - J_i \sum_{j=1, j \neq i}^{n} \frac{x_j}{D_{ij}} \quad \textbf{(A-19)}$$

$$C_t \nabla x_i = \sum_{j=1, j \neq i}^{n-1} x_i \left(\frac{1}{D_{ij}} - \frac{1}{D_{in}} \right) J_j - J_i \left(\frac{x_i}{D_{in}} - \sum_{j=1, j \neq i}^{n} \frac{x_j}{D_{ij}} \right) \quad \textbf{(A-20)}$$

Define matrix B with components

$$B_{ij} = x_i \left(\frac{1}{D_{ij}} - \frac{1}{D_{in}} \right), i \neq j \quad \textbf{(A-21)}$$

$$B_{ii} = \frac{x_i}{D_{in}} - \sum_{k=1, k \neq i}^{n} \frac{x_k}{D_{ik}} \quad \textbf{(A-22)}$$

Finally,

$$C_t \nabla x_i = -B_{ii} J_i - \sum_{j=1, j \neq i}^{n-1} B_{ij} J_j \quad \textbf{(A-23)}$$

In matrix form

$$C_t [\nabla x] = -[B][J] \quad \textbf{(A-24)}$$

In terms of diffusion fluxes

$$[J] = -C_t [B]^{-1} [\nabla x] \quad \textbf{(A-25)}$$

Appendix B - Model Parameters and Constants

The parameters and constants used in the lambda sensor model are presented in this appendix. Table B-1 shows the baseline of pre-catalyst operating conditions in addition to the sensor adsorption capacity and porosity/tortuosity factor.

Table B-1 Model parameters

Parameter	Description	Unit	Value
T	Exhaust gas temperature	K	973
P	Exhaust gas pressure	kPa	100
L	Adsorption capacity	mol/m^2	1.5E-5
ε/q	Porosity/Tortuosity factor	-	0.01

Table B-2 presents the values of the species molecular weight and diffusion values. These parameters used to calculate the binary diffusion coefficient in equation (2-26).

Table B-2 Species molecular weight and diffusion volume

	N_2	CO_2	H_2O	O_2	CO	H_2	NO	CH_4
M (g/mol)	28.01	44.01	18.02	32	28.01	2.016	30	16.04
Σ_v (cm^3/mol)	17.9	26.9	12.7	16.6	18.9	7.07	11.17	24.42

The results from the binary diffusion coefficients calculation are depicted in Table B-3.

Table B-3 Binary diffusion coefficients ($cm^2/s \times 10^4$)

	N_2	CO_2	H_2O	O_2	CO	H_2	NO	CH_4
N_2		118	190	149	148	546	172	158
CO_2	118		152	116	116	459	133	129
H_2O	190	152		190	186	632	220	193
O_2	149	116	190		146	559	171	158
CO	148	116	186	146		534	169	156
H_2	546	459	632	559	534		649	495
NO	172	133	220	171	169	649		180
CH_4	158	129	193	158	156	495	180	

Table B-4 shows the constants used to calculate the rate of reaction of each elementary step reaction used in this model. All of these constants are taken from the literature.

Table B-4 Reaction rate constants

		Reaction	*s/k (1/s)*	*E*(kJ/mol)
Adsorption	1	$O_2 + 2* \rightarrow 2O_s$	0.003	
	2	$CO + * \rightarrow CO_s$	0.84	
	3	$H_2 + 2* \rightarrow 2H_s$	0.05	
	4	$NO + * \rightarrow NO_s$	0.5	
	5	$H_2O + * \rightarrow H_2O_s$	0.1	
	6	$CH_4 + 5* \rightarrow C_s + 4H_s$	5e4	43.1
Surface Reaction	7	$O_s + H_s \rightarrow OH_s + *$	1e12	10.5
	8	$OH_s + * \rightarrow H_s + O_s$	1e8	20.9
	9	$OH_s + H_s \rightarrow H_2O_s + *$	9e16	62.8
	10	$H_2O_s + * \rightarrow OH_s + H_s$	1.8e13	154.9
	11	$2OH_s \rightarrow H_2O_s + O_s$	1e15	51.5
	12	$C_s + O_s \rightarrow CO + *$	5e13	62.8
	13	$CO_s + * \rightarrow C_s + O_s$	1e11	184.1
	14	$CO_s + O_s \rightarrow CO_2 + 2*$	1e15	$100\text{-}50\theta_o$
	15	$NO_s + * \rightarrow N_s + O_s$	8.3e4	56.5
	16	$NO_s + N_s \rightarrow N_2 + O_s + *$	2e9	87.8
	17	$2N_s \rightarrow N_2 + 2*$	3e10	120
Desorption	18	$2O_s \rightarrow O_2 + 2*$	5e12	$215\text{-}60\theta_o$
	19	$CO_s \rightarrow CO + *$	1e13	125.6
	20	$2H_s \rightarrow H_2 + 2*$	5e15	75.4
	21	$NO_s \rightarrow NO + *$	2.6e8	34.3
	22	$H_2O_s \rightarrow H_2O + *$	1e13	45.2

Appendix C - Uncertainly Analysis of Lambda Calculation

The normalized air-to-fuel ratio (lambda) is calculated using the following equation (Mario Balenvic, 2002):

$$\lambda = \frac{2x_{CO_2} + x_{CO} + 2x_{O_2} + x_{NO} + x_{H_2O}}{2x_{CO_2} + 2x_{CO} + x_{H_2} + \left(2\alpha + \frac{\beta}{2}\right)x_{C_\alpha H_\beta} + x_{H_2O}} \quad \textbf{(C-1)}$$

Equation (C-1) was derived based on solving a set of non-linear equations representing species mass balance and chemical equilibrium equations. This equation facilitates the calculation of lambda based on the exhaust gases mole fractions. The uncertainty of lambda is determined using the following general uncertainty analysis equation (Holman, 2000):

$$u_z = \sqrt{\left(u_{y_1}\frac{\partial z}{\partial y_1}\right)^2 + \left(u_{y_2}\frac{\partial z}{\partial y_2}\right)^2 + \cdots + \left(u_{y_n}\frac{\partial z}{\partial y_n}\right)^2} \quad \textbf{(C-2)}$$

The above equation presents the uncertainly in the dependent variable *Z* as a function of *n* independent variables *y*. (i.e., $Z = f(y_1, y_2, \ldots, y_n)$). The uncertainty in *Z* is the root-sum-squares of the uncertainly of each variable y. applying equation (C-2) to lambda expression reveals that:

$$u_\lambda = \sqrt{\begin{array}{c}\left(u_{x_{CO_2}}\frac{\partial z}{\partial x_{CO_2}}\right)^2 + \left(u_{x_{CO}}\frac{\partial z}{\partial x_{CO}}\right)^2 + \left(u_{x_{O_2}}\frac{\partial z}{\partial x_{O_2}}\right)^2 + \left(u_{x_{NO}}\frac{\partial z}{\partial x_{NO}}\right)^2 \\ + \left(u_{x_{H_2O}}\frac{\partial z}{\partial x_{H_2O}}\right)^2 + \left(u_{x_{H_2}}\frac{\partial z}{\partial x_{H_2}}\right)^2 + \left(u_{x_{C_\alpha H_\beta}}\frac{\partial z}{\partial x_{C_\alpha H_\beta}}\right)^2\end{array}} \quad \textbf{(C-3)}$$

The uncertainty of each species mole fraction is calculated based on the standard deviation of the data collected during the test. The value of the derivatives in the above equation is calculated using the average of the 5 min. data set which has been measured during each run. The hydrocarbons involved in lambda calculation are methane (CH_4), ethane (C_2H_6), ethylene

(C_2H_4), and propane (C_3H_8). All of these species were measured using the FTIR analyzer during engine mapping. Table C-1 presents the results of lambda calculation and it's uncertainty of each test of the engine mapping study.

Table C-1 The calculated lambda of engine mapping tests

	Lambda (λ)	**Uncertainty (u_λ)**
Test 7	0.9947167	±0.001031
Test 14	1.0072295	±0.000745
Test 22	1.0023941	±0.000758
Test 25	0.9975438	±0.000466
Test 30	0.9981024	±0.000827
Test 32	0.9956547	±0.000409

Appendix D - Field Testing Engine Specifications

This appendix shows the specification of the three engines used in the NSCR field testing. Table D-1 presents the rated power and site location of each engine used in the "Four Corners" study. This table also shows the description on the catalyst and controllers of each engine. In addition, the description of the monitoring technique was also mentioned. This appendix also presents some photos of these engines. These pictures show some details of the engine such as the instrumentation box that contains the portable emission analyzer, the controller and cellular modem. Figure D.2 shows a picture of the trailer used during engine mapping. This trailer used during this week of study as an in-kind donation from El Paso Pipeline Company.

Table D-1 "Four-Corners" study engine specifications

Engine #	Location	HP	Monitoring Description	NSCR System Specifications
1	Farmington, NM	57	• Continuous • Mapping • NH_3 bi-monthly	Emit Edge and Emit catalyst
2	Farmington, NM	23	• Continuous • NH_3 bi-monthly	Emit Edge and Emit catalyst
3	Durango, CO	1467	• Continuous • NH_3 bi-monthly	Altronic EPC 110 with QUICK-LID Model DC74-12 catalyst

Figure D.1 Engine 1 picture showing the instrumentation box

Figure D.2 Engine 1 during mapping

Figure D.3 FTIR analyzer used in Engine 1 mapping

Figure D.4 Engine 2 in Farmington, NM

Figure D.5 Engine 3 in Durango, CO

Figure D.6 Inside the Instrumentation box showing the portable analyzer